

EFFECT OF ELECTRON AND PHONON EXCITATION ON THE OPTICAL
PROPERTIES OF INDIRECT GAP SEMICONDUCTORS

By

Justin Mark Gregory

Dissertation

Submitted to the Faculty of the
Graduate School of Vanderbilt University
in partial fulfillment of the requirements
for the degree of

DOCTOR OF PHILOSOPHY

in

Interdisciplinary Materials Science

May, 2013

Nashville, TN

Approved:

Professor Norman H. Tolk

Professor Jim L. Davidson

Professor Leonard C. Feldman

Professor Timothy P. Hanusa

Professor Sokrates T. Pantelides

Professor Ronald D. Schrimpf

ACKNOWLEDGEMENTS

This work would not have been possible without funding from the Interdisciplinary Graduate Education Research Traineeship (IGERT) fellowship and from grant CHE-0707044, both provided by the National Science Foundation; from the U.S. Army Research Office under agreement number W911NF-10-1-0363; and from the Department of Energy under grant number FGO2-99ER45781. Portions of this work were performed at the Vanderbilt Institute of Nanoscale Science and Engineering, using facilities renovated under NSF ARI-R2 DMR-0963361. Transmission electron microscopy research supported by Oak Ridge National Laboratory's Shared Research Equipment (ShaRE) User Program, which is sponsored by the Office of Basic Energy Sciences, the U.S. Department of Energy.

I am indebted to Professor Norman Tolk for his guidance as my dissertation advisor, and to each member of my committee: Dr. Jim Davidson for his expertise on all people and things diamond-related, Dr. Len Feldman for many timely and insightful discussions, and to Drs. Sokrates Pantelides, Ron Schrimpf, and Tim Hanusa for their valuable input. I owe many thanks to Dr. Anthony Hmelo for his unwavering dedication in maintaining the Van der Graaff accelerator laboratory, his expertise concerning the ion implantations, and for helpful discussions. I am also grateful to the current and former members of the Tolk lab for their help and advice, including Dr. Halina Krzyzanowska, Dr. Heungman Park, Stephanie Gilbert Corder, Dr. Ying Xu, Dr. Jingbo Qi, Jennifer Jones, Zeynab Jarrahi, Joy Garnett, and particularly Dr. Andrew Steigerwald, Dr. Dongmin Seo, and Dr. Travis Wade. The valuable transmission electron microscopy studies included in this work would not have been possible without the kind support of Joyce Miller, Dr. Nathaniel Smith, Dr. Jim Wittig, Dr. Lawrence Allard, Dr. Kinga Unocic, and Dorothy Coffey. For helpful collaboration,

discussion, and advice on the germanium multiphoton absorption project, I am indebted to Dr. Phil Cohen, Dr. John Kozub, Dr. Hernando Garcia, Dr. Shekhar Guha, Dr. Leo Gonzales, Joel Murray, and Dr. Torrey Wagner. There are several others to whom I owe thanks, in some cases more than a simple acknowledgement permits, and these include Sarah Satterwhite, René Colehour, Sandy Childress, Eric Dye, Jane Fall.

I am forever grateful to my parents and grandparents for setting me on a lifelong path of knowledge, and to many teachers and mentors over the years for helping to continue in it. I thank both my parents and parents-in-law for encouraging me to continue my graduate school effort. Also, much support and encouragement were received from my brother Jacob and from several dear friends.

Finally, to my wife Stella and my daughters Eliza and Esther: You are the lights of my life, and the reason I get up every morning. For your unflagging patience, support, and love over the last several years, thank you.

In all things, *Deo gratias*.

TABLE OF CONTENTS

	Page
ACKNOWLEDGEMENTS	ii
LIST OF TABLES	vii
LIST OF FIGURES	xi
FOREWORD	xii
PART ONE: MULTIPHOTON ABSORPTION IN GERMANIUM	1
Chapter	
I. INTRODUCTION	2
I.1 Research Problem	2
I.1.1 Linear Absorption	2
I.1.2 Nonlinear Absorption	3
I.1.3 Germanium	6
I.2 Statement of Work	8
I.3 Scope and Limitations	9
II. LITERATURE REVIEW	10
II.1 Nonlinear Absorption in Semiconductors	10
II.1.1 Theory	10
II.1.2 Experiments	13
II.2 Nonlinear Absorption in Germanium	17
II.2.1 Theory	17
II.2.2 Experiments	19
II.3 Carrier Dynamics in Germanium	24
III. EXPERIMENT AND SIMULATION	29
III.1 Methodology	29
III.1.1 Vanderbilt Free Electron Laser	29
III.1.2 Transmission Measurement	30
III.1.3 Beam Diameter	31
III.1.4 Free Carrier Absorption Coefficients	31

III.2	Results.....	33
III.2.1	FEL Transmittance in Germanium.....	33
III.2.2	Simulation.....	35
III.2.3	Beam Propagation and Carrier Concentrations.....	37
III.2.4	Fitted Absorption Coefficients.....	38
III.3	Analysis.....	40
III.3.1	Comparison to Literature.....	40
III.3.2	Limitations in the Derived Coefficients.....	41
III.3.3	Ratios of Absorption Coefficients.....	42
III.4	Potential Expansion Studies.....	43
 PART TWO: COHERENT ACOUSTIC PHONON INTERFEROMETRY OF ION IMPLANTATION DEFECTS IN DIAMOND CRYSTALS		 45
IV.	INTRODUCTION.....	46
IV.1	Research Problem.....	46
IV.2	Statement of Work.....	50
IV.3	Scope and Limitations.....	51
V.	LITERATURE REVIEW.....	52
V.1	Ion Implantation in Diamond.....	52
V.1.1	Optical Properties of Ion-implanted Diamond.....	53
V.2	Coherent Acoustic Phonon Interferometry.....	60
V.2.1	The CAP Technique.....	60
V.2.2	CAP in Ion-implanted Materials.....	67
V.2.3	CAP in Diamond.....	69
V.2.4	Summary.....	70
VI.	EXPERIMENT.....	71
VI.1	Methodology.....	71
VI.1.1	Implantation.....	71
VI.1.2	Coherent Acoustic Phonon Interferometry.....	72
VI.2	Results.....	72
VI.2.1	Coherent Acoustic Phonon Interferometry.....	72
VI.2.2	Transmission Electron Microscopy.....	76
VI.3	Discussion.....	79
VI.3.1	Phase Reversal.....	79
VI.3.2	Cumulative Phase Shift.....	81
VI.3.3	Persistent Amplitude Loss.....	85

VII. PHENOMENOLOGICAL MODEL	88
VII.1 Objective and Limitations	88
VII.2 Analytical Approach	89
VII.2.1 Introduction	89
VII.2.2 Relationship to Experimental Observables	90
VII.2.3 Phenomenological Model	91
VII.2.4 Calculation and Results	92
VII.3 Numerical Simulation	95
VII.3.1 Theory	95
VII.3.2 Calculation	96
VII.3.3 Results and Discussion	98
VII.4 Potential Expansion Studies	103
CONCLUSIONS	105
REFERENCES	107

LIST OF TABLES

Table		Page
1	Reported experimental values for the germanium two-photon absorption coefficient β	24
2	Absorption cross-sections in Ge for electrons (σ_n) and holes (σ_p) as measured by low-intensity FTIR.	33
3	Fitted two-photon absorption coefficients.	39
4	Fitted three-photon absorption coefficients.	39
5	Selected literature values for β in Ge near 2.8 μm	40
6	Summary of the explanation for the phase reversal behavior in the CAP oscillations at $C_V = 3.9 \times 10^{20} \text{ cm}^{-3}$	82
7	Experimental parameters and results from available works studying the variation in real refractive index of ion irradiated diamond crystals.	86
8	Constant and best fit parameters for the exponential model given in Equations 36 and 37 using the analytical approach.	93
9	Experimental and simulation parameters used in the numerical calculation of the CAP reflectivity oscillations.	98
10	Specimen-specific properties used in the full numerical simulation.	99
11	Best fit parameters for the exponential model given in Equations 36, 37, and 41 using the full numerical simulation.	99

LIST OF FIGURES

Figure		Page
1	Various types of optical absorption.....	3
2	Theoretical transmission curves as a function of intensity for multiple values of β	5
3	Electronic band structure of germanium.	7
4	Allowed wavelength regimes for various absorption mechanisms in germanium.	7
5	Comparison of the photon energy-dependence of the theoretical two-photon absorption coefficient β between the Brandt and Wherrett scaling rules.	13
6	A simple photoconductivity experiment for determining absorption coefficients.	15
7	Nonlinear absorption measurement by direct transmission	15
8	Z-scan transmittance data in ZnSe.	16
9	Pump-probe transmittance in InAs.	17
10	Transmittance and photoconductivity results in Ge from Gibson et al.	20
11	Indirect 2PA photoconductivity vs. photon energy in Ge.	21
12	Nonlinear pump-probe spectroscopy of Ge.	22
13	Reported experimental values for the germanium two-photon absorption coefficient β , by year.	23
14	Time-resolved pump-probe transmission of 1.06 μm photons in germanium.	25
15	Temperature-dependent pump-probe transmittance in Ge.	28
16	Time-resolved probe transmission in germanium.	28

17	Vanderbilt FEL temporal pulse structure	30
18	Experimental setup for measuring multiphoton absorption in germanium.	30
19	Z-scan measurements at multiple FEL wavelengths.	32
20	Optical microscopy images of FEL-ablated germanium.	32
21	Transmittance vs. FEL peak intensity at all wavelengths studied.	34
22	Transmittance vs. FEL wavelength at two intensities.	35
23	Fitting agreement between simulation code and experimental results.	37
24	Fitted absorption coefficients for the transmittance data shown in Figure 21.	39
25	Theoretical wavelength dependence for direct and indirect 2PA in germanium.	41
26	Scanning confocal fluorescence micrographs of single fluorescent NV ⁻ centers in type Ib diamond.	47
27	Implantation and lift-out technique for photonic device fabrication in diamond crystals.	48
28	Single-crystal diamond nanostructures generated using the ion implantation and lift-out technique.	49
29	Refractive index and optical absorption of C ⁺ -implanted diamond as measured by Bhatia et al.	54
30	Real and imaginary refractive indices of graphitized implanted diamond layers as measured by Khomich et al.	55
31	Variation in the real and imaginary parts of the refractive index of Ga ⁺ -implanted diamond, as measured by Draganski et al.	56
32	Optical path difference data at 632.8 nm for proton-implanted diamonds as measured by Olivero et al.	58

33	Derived refractive index information for proton-irradiated diamonds, as measured by Battiato et al.	59
34	Optical measurements of proton-implanted diamond specimens by Lagomarsino et al.	60
35	Schematic views of strain wave generation and reflection interference in a typical CAP experiment.	62
36	Coherent acoustic phonon strain pulse shape.	63
37	CAP-induced interference oscillations in the pump-probe reflectivity signal of a GaAs specimen.	64
39	CAP reflectivity of a Ga _{0.95} Mn _{0.05} As/LT-GaAs/GaAs heterostructure.	66
40	CAP response of a He ⁺ -implanted GaAs specimen.	68
41	Comparison between experimentally-derived vacancy concentration profile from CAP reflectivity data and TRIM code simulation.	68
42	Experimental setup for CAP measurement of ion implanted diamonds.	73
43	Typical pump-probe reflectivity responses for implanted and unim- planted diamond crystals.	73
44	CAP oscillations in ion-implanted diamonds at multiple fluences.	75
45	Comparison of CAP oscillations and cross-sectional TEM at ion flu- ence 10 ¹⁵ cm ⁻²	77
46	Comparison of CAP oscillations and cross-sectional TEM at ion flu- ence 3 × 10 ¹⁶ cm ⁻²	78
47	Variations in CAP oscillation features with He ⁺ implantation fluence.	80
48	Comparison between CAP oscillations and simple optical transmit- tance for the implanted specimens.	87
49	Variation in the real and imaginary components of $\tilde{n}(C_V)$ over a range of vacancy concentrations, using the parameters given in Table 8.	93

50	Comparison of the exponential model given in Equations 36 and 37 using an analytical approach with the parameters from Table 8, along with experimental data from Chapter VI.	94
51	Variation in the real and imaginary components of $\tilde{n}(C_V)$ and $p_{12}(C_V)$ over a range of vacancy concentrations, using the parameters given in Table 11.	100
52	Comparison of the best fit of the exponential model given in Equations 36, 37, and 41 to the experimental data from Chapter VI.	101

FOREWORD

The interaction of electrons and phonons with the properties of semiconducting crystals continues to be a fascinating and highly fruitful field of study. This dissertation addresses two research problems under the general heading of electron and phonon effects on the optical properties of indirect gap semiconductors. The first problem addresses nonlinear (multi-photon) absorption in germanium crystals, a topic of interest for the telecommunications industry as well as to the basic scientist. As will be shown, a straightforward analysis of transmission measurements is rapidly complicated by the effects of photo-excited electrons, requiring numerical approaches. The second problem concerns the optical characteristics of ion-bombarded diamond crystals, which is a swiftly developing field due to diamond's current status as the material of choice for hosting photonic and quantum information devices. This study employs phonon effects, specifically an ultrafast optical technique called coherent acoustic phonon interferometry, to measure the implantation-induced optical modifications. A quantitative model for those modifications is then developed using numerical simulations.

Summary of Contents

Part one of this work, *Multiphoton Absorption in Germanium*, consists of the following: Chapter I (Introduction) introduces nonlinear absorption phenomena and describes their importance, Chapter II (Literature Review) gives an overview of experimental and theoretical approaches to measuring and predicting nonlinear absorption, Chapter III (Experiment and Simulation) presents the results of experimental studies of germanium multiphoton absorption, and the numerical simulations used to interpret them.

The contents of the second part of this dissertation, *Coherent Acoustic Phonon Interferometry of Ion Implantation Defects in Diamond Crystals*, are as follows: Chapter IV (Introduction) motivates the study of the optical properties of diamond, and describes the research problem. Chapter V (Literature Review) provides an overview of the current state of knowledge with respect to the optical properties of diamond, ion implantation in diamond, and the CAP technique. Chapter VI (Experiment) will detail the experimental methods used in these studies and discuss the results of the CAP experiments, along with a comparison to TEM. The numerical simulations and the quantitative model will be discussed in Chapter VII (Phenomenological Model).

Finally, a brief Conclusions chapter summarizes the scientific results from both parts of this dissertation.

PART ONE:

MULTIPHOTON ABSORPTION IN GERMANIUM

CHAPTER I

INTRODUCTION

This introductory chapter provides a brief overview of nonlinear absorption phenomena and introduces some of the factors which can complicate an otherwise straightforward analysis of multiphoton absorption in germanium, particularly the role of photo-excited electrons. Following that is a statement of work describing the research project, and a discussion of the scope and limitations of the project.

I.1 Research Problem

I.1.1 Linear Absorption

Ordinary linear absorption in semiconductors may be described as a one-step process whereby an electron is photo-excited from the valence band to the conduction band, absorbing one photon of energy $\hbar\omega$. (See Figure 1a.) From the macroscopic standpoint of an optical pulse propagating through a linearly absorbing region, the absorption is described by an absorption coefficient α , such that

$$\frac{\partial I}{\partial z} = -\alpha I, \quad (1)$$

where I is the optical intensity (power per unit area) of the pulse and z is sample depth. This equation leads directly to the Beer-Lambert law for a pulse of initial intensity I_0 traveling a distance z through a linearly absorbing region:

$$I(z) = I_0 e^{-\alpha z}. \quad (2)$$

The optical transmittance T (or often, ‘transmission’) of an absorbing region of thickness L is defined as the ratio of incoming and outgoing intensities, $T = I/I_0$. Thus,

$$T = e^{-\alpha L}. \quad (3)$$

Linear transmittance therefore depends on the thickness of the region under study, but has no dependence on the initial intensity of the incident light.

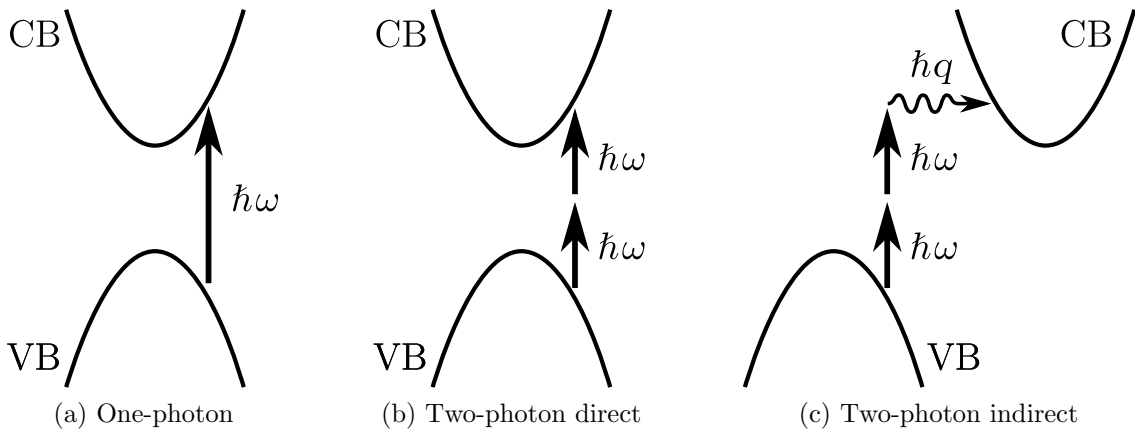


Figure 1: Various types of optical absorption, each resulting in the creation of a single electron-hole pair. Two-photon indirect absorption (1c) in the bulk is assisted by the creation or annihilation of a phonon with momentum $\hbar q$.

1.1.2 Nonlinear Absorption

The widespread availability of lasers in the last several decades has allowed the observation of nonlinear absorption and refraction effects. Such processes have been used to demonstrate the generation of low, evenly-distributed carrier densities, [1] optical limiting, [2,3] optical switching, [4] holography, [5] and laser frequency tuning by optical parametric oscillation. [6]

In semiconductor multiphoton absorption processes, a valence band electron attains to the conduction band by simultaneously absorbing two or more photons. Any

or all of these photons may have sub-band-gap energies (see Figure 1b). Such cases are usually understood using the concept of virtual states, [7] with uncertainty relationships restricting virtual state lifetimes to the order of 10^{-15} s. Such short lifetimes impose an upper limit on the time in which the absorption of multiple photons must occur, therefore very high photon densities (*i.e.*, $I > 10^6$ W/cm², as may be produced using lasers) are required. The necessary intensity to observe an n -photon absorption process increases roughly as I^n .

The more general form of Equation 1, including multiphoton transitions, is

$$\frac{\partial I}{\partial z} = -\alpha I - \beta I^2 - \gamma I^3 \dots, \quad (4)$$

where the coefficient β (usually in cm/GW) describes two-photon absorption, γ (cm³/GW²) describes three-photon absorption, and so on for higher-order processes. All of these coefficients are functions of the energies of the absorbed photons. Thus, in the general case, $\beta = \beta(\omega_1, \omega_2)$, $\gamma = \gamma(\omega_1, \omega_2, \omega_3)$, etc. If all of the absorbed photons have the same frequency ($\omega_1 = \omega_2 = \dots = \omega$), the process is referred to as degenerate.

Typically, absorption phenomena are dominated by the lowest-order allowed process. For instance, in the case where $\hbar\omega < E_g < 2\hbar\omega$, one-photon absorption is forbidden (*i.e.*, $\alpha(\omega) \rightarrow 0$), and three-photon absorption is usually relatively weak ($\gamma I \ll \beta$). Thus, the two-photon transition dominates. In any case where two or more orders of transition are allowed, one may define a critical intensity $I_c = k^{(n)}/k^{(n+1)}$, where $k^{(n)}$ is the absorption coefficient of an n -th order transition. For incoming intensities $I \sim I_c$, the higher-order transition must be considered. If $I \gg I_c$, the higher-order transition will dominate.

In the intensity and wavelength regime where two-photon absorption is the only significant transition process,

$$\frac{\partial I}{\partial z} = -\beta I^2. \quad (5)$$

Solving this equation analogously to the Beer-Lambert Law and deriving the transmittance yields, for a two-photon absorbing region of thickness L ,

$$T = \frac{1}{\beta L I_0 + 1}. \quad (6)$$

Note that transmittance is now a nonlinear function of incident intensity, as shown in Figure 2. Generally in multiphoton absorption, the greater the incoming intensity, the smaller the transmittance.

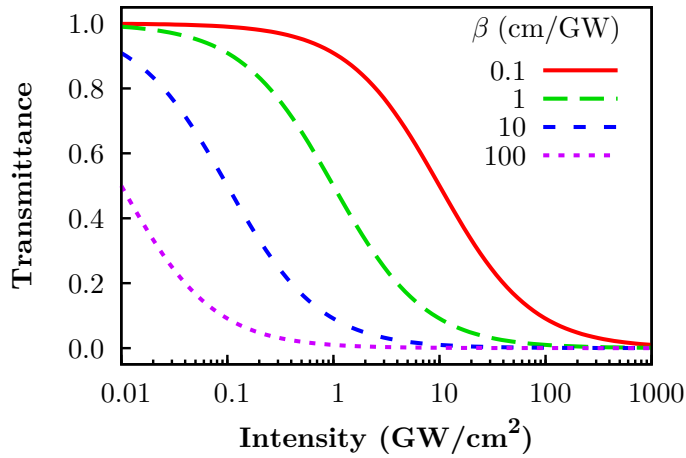


Figure 2: Theoretical transmission curves as a function of incoming intensity for a 1 cm-thick sample with various values of β , based on Equation 6. Reflection at surfaces is ignored.

Experimental techniques for determining nonlinear absorption coefficients are described in detail in Section II.1.2. Typically, the transmittance of a beam is measured as a function of incident intensity and fitted to an equation such as Equation. 6, but

these measurements are usually complicated by the presence of photo-excited carriers, as described further below.

I.1.3 Germanium

The electronic and optical properties of germanium make it a very interesting material for the study of multiphoton absorption. Germanium has an indirect band gap of 0.66 eV at the Γ point, and a direct gap only slightly higher at 0.8 eV. Figure 3 shows the detailed band structure of germanium. This band configuration provides a relatively even distribution of absorption onset wavelengths, as shown in Figure 4. In general, indirect multiphoton absorption (see Figure 1c) is expected to be much weaker than the direct case, due to the required participation of an added phonon. Therefore, if one has a range of available experimental wavelengths similar to that shown in Figure 4, by scanning up in photon energy it should be possible to observe the onset of each new type of absorption.

Despite these unique properties, multiphoton absorption in germanium has been studied relatively little in comparison with other semiconductors. In addition, there is no strong agreement in the literature on the actual absorption coefficients (see Section II.2.2), and reported values can vary by several orders of magnitude. At least one cause for these discrepancies appears to be the effect of photogenerated carriers. Once an electron-hole pair has been created by multiphoton absorption, either of the two carriers may be subsequently excited to higher energy bands in a single-photon absorption process. Thus, Equation 5 becomes

$$\frac{\partial I}{\partial z} = -\beta I^2 - \sigma_e N_e I - \sigma_h N_h I, \quad (7)$$

where N_e and N_h are the electron and hole densities, and σ_e and σ_h are the respective absorption cross sections. These cross sections are likely to be dependent on the

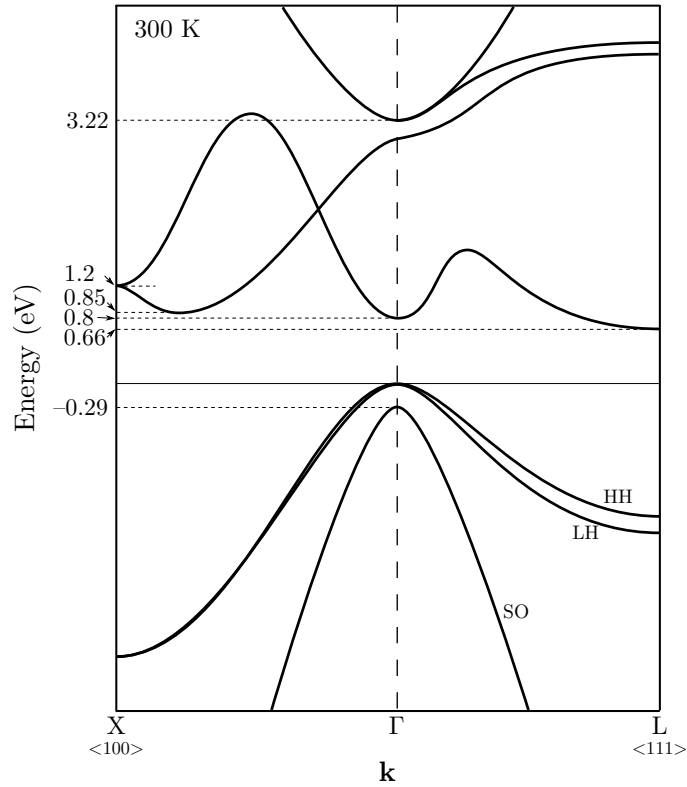


Figure 3: Electronic band structure of germanium, from [8] and [9]. Indicated energy values are to scale; others are approximations.

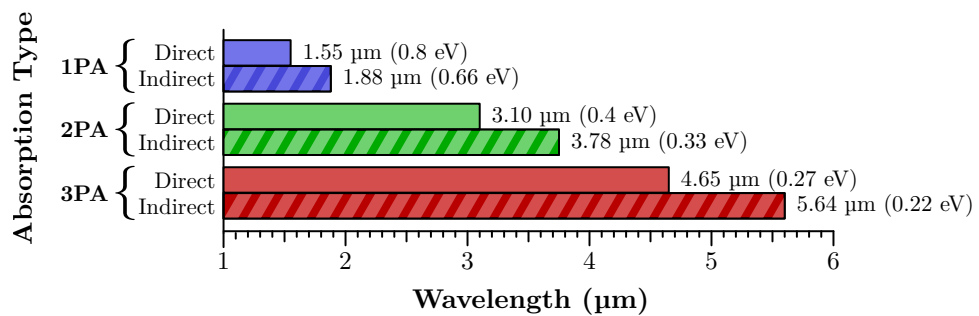


Figure 4: Allowed wavelength regimes for various absorption mechanisms in germanium. The cutoff wavelengths and corresponding photon energies are listed for each process to the right of the corresponding bar.

energy states of these particles, which may not reach equilibrium on the ultrafast time scales of current laser pulses. Generated carriers can modulate the optical properties of the sample, causing enhanced reflection, absorption saturation, and beam deflection due to changes in refractive index. In addition, the carrier densities will vary with time and space in the sample so that diffusion, recombination, self-thermalization, intervalley scattering, stimulated emission, and lattice thermalization may all become important. In these cases, analytical solutions to the underlying differential equations are generally unavailable, and numerical methods must be used. Though some efforts have been made to address these issues (see Section II.2.1), much more work is needed to develop a clear understanding of the complex interactions involved, and to develop the tools for accurate analysis of experimental data.

I.2 Statement of Work

In this study, the question of multiphoton absorption in germanium is addressed using a two-pronged approach consisting of experiment and numerical calculations. The experimental work makes use of the Vanderbilt Free Electron Laser, a source uniquely suited for these studies, and the numerical calculations allow for the consideration of excited carrier effects. Using this combination of experimental and simulation techniques, multiphoton absorption coefficients are derived in the 2.8 μm –5.2 μm wavelength range, which accesses direct and indirect absorption regimes for both two- and three-photon absorption. The experimental and numerical techniques are described in detail in the chapters that follow, as well the limitations of those techniques, and how those limitations may influence the derived quantities.

I.3 Scope and Limitations

A clear understanding of carrier dynamics in germanium is required in the development of accurate computer simulations of multiphoton absorption phenomena. Likewise, nonlinear refraction must be considered to some extent as a possible beam modulation mechanism, and is developing into a significant field of study. [3, 10–13] However, the primary focus of this work is intended to be multiphoton absorption, and these areas will only be addressed to the extent necessary to correctly describe the observed absorption-related phenomena.

CHAPTER II

LITERATURE REVIEW

In this chapter the theoretical and experimental techniques for the study of multiphoton absorption in semiconductors are generally described, followed by the results of particular applications of both theory and experiment to germanium. After that is a brief description of experiments studying free carrier dynamics in germanium.

II.1 Nonlinear Absorption in Semiconductors

Two thorough reviews of nonlinear optical phenomena in semiconductors have been written by Nathan [1] and Garmin. [5] The material presented here includes many works cited in these articles, as well as some more recent reports.

II.1.1 Theory

Multiphoton absorption processes were first explored theoretically by Maria Göppert-Mayer in 1931. [14] She predicted both multiphoton absorption and multiphoton emission. However, such effects were not observed experimentally until after the advent of the laser, [15, 16] and theoretical models had no basis of comparison until that time. [17] Since then, two distinct branches of theory on multiphoton absorption have developed, one based on higher-order perturbation theory, and the other using a model introduced by Keldysh.

Higher-order Perturbation Theory

The first branch is based on time-dependent perturbation theory, as initially stated by Göppert-Mayer and developed by many authors since. In this method, the probability for an n -photon direct electron transition from an initial valence band v to a final

conduction band c is, according to Fermi's golden rule: [1]

$$\begin{aligned}
W_n = \frac{2\pi}{\hbar} \int & \left| \sum_m \sum_l \cdots \sum_j \sum_i \frac{\langle \Psi_c | H | \Psi_m \rangle \langle \Psi_m | H | \Psi_l \rangle}{[E_m - E_l - (n-1)\hbar\omega]} \right. \\
& \cdots \frac{\langle \Psi_j | H | \Psi_i \rangle}{(E_j - E_i - 2\hbar\omega)} \frac{\langle \Psi_i | H | \Psi_v \rangle}{(E_i - E_v - \hbar\omega)} \left. \right|^2 \\
& \times \delta [E_c(\mathbf{k}) - E_v(\mathbf{k}) - n\hbar\omega] \frac{d^3\mathbf{k}}{(2\pi)^3} \quad (8)
\end{aligned}$$

where $j \dots m$ are intermediate states with energies $E_j \dots E_m$ and the integration is over all of \mathbf{k} -space. At this point various simplifications are applied, depending on the properties of the system being studied. Recent work has been able to use sophisticated band models, yielding good agreement with experimental results. [18, 19]

For two-photon absorption ($n = 2$), Equation. 8 is simplified to:

$$W_2 = \frac{2\pi}{\hbar} \int \left| \frac{\sum_i \langle \Psi_c | H | \Psi_i \rangle \langle \Psi_i | H | \Psi_v \rangle}{(E_i - E_v - \hbar\omega)} \right|^2 \times \delta [E_c(\mathbf{k}) - E_v(\mathbf{k}) - 2\hbar\omega] \frac{d^3\mathbf{k}}{(2\pi)^3} \quad (9)$$

The two-photon absorption coefficient β is related to W_2 by:

$$\beta = \frac{2W_2(2\hbar\omega)}{I^2}. \quad (10)$$

In 1984, Wherrett [20] used perturbation theory to derive a formula for direct-gap multiphoton absorption coefficients based on a simplified band model. The strength of the Wherrett equation is not in the prediction of absolute values for the coefficients, but in providing a universal gap dependence, which enables one to estimate absorption coefficients for a given material based on the known coefficients of another material. Wherrett's scaling rule for two-photon absorption may be expressed as:

$$\beta \propto \frac{1}{E_g^3} \frac{(2\hbar\omega/E_g - 1)^{3/2}}{(2\hbar\omega/E_g)^5} \quad (11)$$

This rule was later verified experimentally by Van Stryland, et al. [21]

Keldysh Model

The second branch of theory is based on a method initially proposed by Keldysh in 1965. [22] The Keldysh model treats multiphoton absorption as one aspect of a wider range of phenomena concerning electrons in oscillating electric fields. Keldysh used a parameter

$$\gamma = \frac{\omega}{eE_0} \sqrt{2m_e E_g} \quad (12)$$

to determine which of two processes would be the dominant observed effect. (Here E_0 is the magnitude of the peak electric field of the incident radiation oscillating at frequency ω). If $\gamma \gg 1$, multiphoton absorption dominates. If $\gamma \ll 1$, strong band-bending may allow electrons to tunnel directly across the forbidden gap.

In the multiphoton absorption limit, the Keldysh method allows for analytical solutions using first-order perturbation theory. As later developed by Brandi, [23] the two-photon absorption coefficient is given as:

$$\beta = \frac{2^{11/2} \pi e^4}{3c^2} \left(\frac{p_{vc}^2 (m^*)^{5/2}}{m^2 m_1^2 n^2} \frac{1}{E_g^{7/2}} \right) f_2 \left(\frac{\hbar\omega}{E_g} \right), \quad f_2(\zeta) \equiv \left(\frac{2\zeta - 1}{\zeta^5} \right)^{3/2} \quad (13)$$

where p_{vc} is the momentum matrix element, m^* is the reduced effective mass, and m_1 is the effective mass in the conduction band.

Both the Keldysh and higher-order perturbation methods have found good agreement with experimental results. [21, 23] The photon-energy dependence of the Brandi and Wherrett scaling rules are plotted in Figure 5 for comparison. The Keldysh method has been favored for its relative ease of calculation, but becomes very complex for higher-order transitions. The perturbation method can also become quite complex when the full band structure and further possibilities for transition routes

are included in the calculation, but as computers have made such work less expensive in the last few decades, the perturbative approach seems to hold more favor. [18]

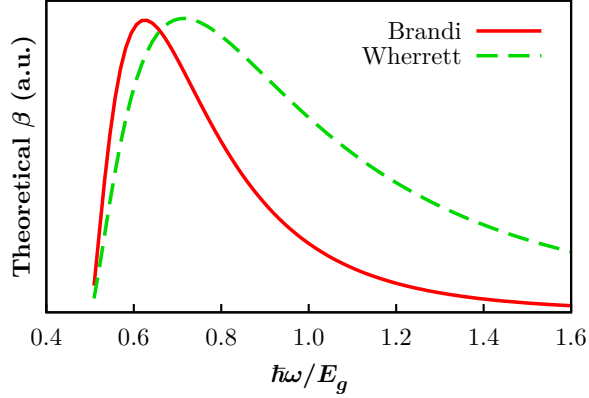


Figure 5: Comparison of the photon energy-dependence of the theoretical two-photon absorption coefficient β between the Brandi [23] and Wherrett [20] scaling rules. The two curves have been normalized for comparison.

II.1.2 Experiments

Two-photon absorption in solids was first observed in Europium-doped CaF_2 crystals in 1961 by Kaiser and Garrett. [15] Since that time, multiphoton absorption has been reported in a wide variety of semiconducting materials, [11, 24–33] with the most recent interest (both theoretical and experimental) in quantum-confined structures. [34–38]

Derived absorption coefficients for a given semiconductor can vary dramatically from study to study, as Van Stryland et al. have shown. [21] The general trend by year appears to be downward; *i.e.*, later papers generally report smaller values of β . This trend appears to be due to increasing awareness of the various factors, such as free carrier absorption and beam instability, which can introduce large errors into derived values if not properly considered.

Photoconductivity

The earliest multiphoton absorption experiments made use of photoconductivity. In nonlinear photoconductivity experiments [1, 39–42] (see Figure 6), a specimen is irradiated with sub-bandgap photons, which generate free carriers via a multiphoton absorption process. A voltage bias is applied across the illumination region and the specimen conductivity is monitored. The generated carriers modulate the specimen conductance Y , and the fractional change in conductance in the illumination region is given by: [40]

$$\frac{\Delta Y}{Y} = \frac{1 + b}{(P + bN)Z} \int_0^Z N_G dz, \quad b = \frac{\mu_e}{\mu_h} \quad (14)$$

where μ_e and μ_h are the electron and hole mobilities, N and P are the electron and hole concentrations, Z is the thickness of the specimen, and N_G is the density of multiphoton absorption-generated carriers, given by

$$N_G = \frac{\beta}{2h\nu} \int_0^\tau I(t)^2 dt. \quad (15)$$

Here a thin sample approximation is used, and the integration is over the time duration τ of the pulse traveling through the specimen. The determination of β is therefore indirect.

One advantage of the photoconductivity technique is that it remains sensitive at low incident intensities, where photodetectors may not be able to distinguish pulse energies. However, the analysis requires precise knowledge of the doping and carrier mobilities in the specimen under study. In addition, it is highly sensitive to impurities.

Direct Transmission

Direct transmission experiments [40, 43, 44] eliminate some of the uncertainty that is present in the photoconductivity method. Figure 7 shows a diagram of a typical

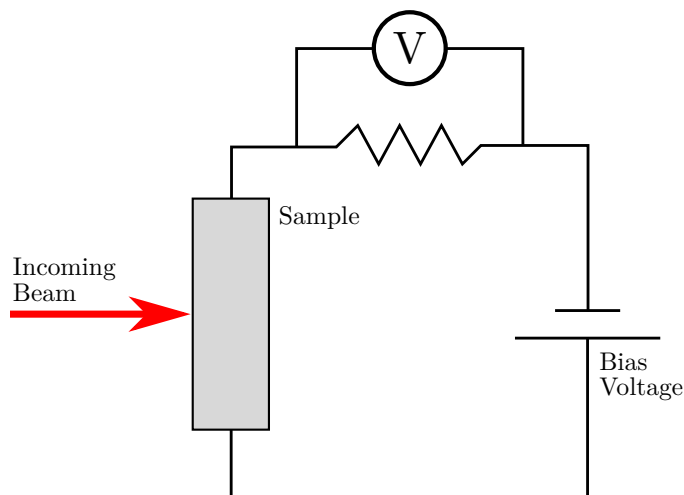


Figure 6: A simple photoconductivity experiment for determining absorption coefficients. The conductivity of the DC-biased, illuminated specimen is monitored by observing the voltage across a resistor in series with the specimen.

setup. In the simplest case, the incoming laser beam is sent through a variable attenuator, then focused on the specimen. The transmitted energy is collected in a photodetector. The transmittance may be obtained by performing the experiment both with and without the specimen in place, in order to obtain I and I_0 , respectively.

Variations in pulse-to-pulse energy are a significant source of error, and may be accounted for by inserting a beam splitter in front of the specimen and sending this line to a second detector, as shown in the figure. The transmittance may then be obtained by means of a calibrated ratio of the two simultaneous detector signals.

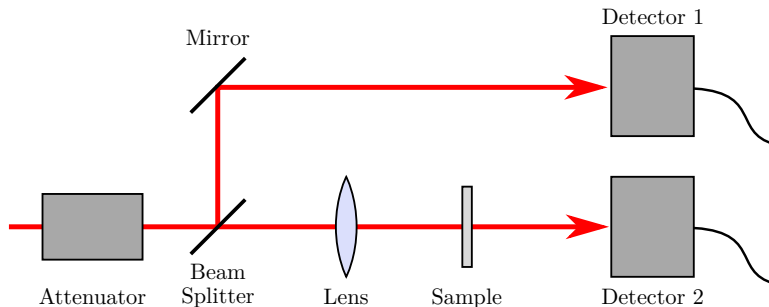


Figure 7: Nonlinear absorption measurement by direct transmission

An alternative to the use of a polarizing attenuator is the z -scan technique, wherein a specimen is shifted along the beam axis. The variation in beam diameter due to the focusing effect of the lens will provide a range of incident intensities as a function of specimen position. Due to the nonlinear nature of the observed absorption, the focal point of the lens may be found at the specimen position of minimum transmittance. (See Figure 8).

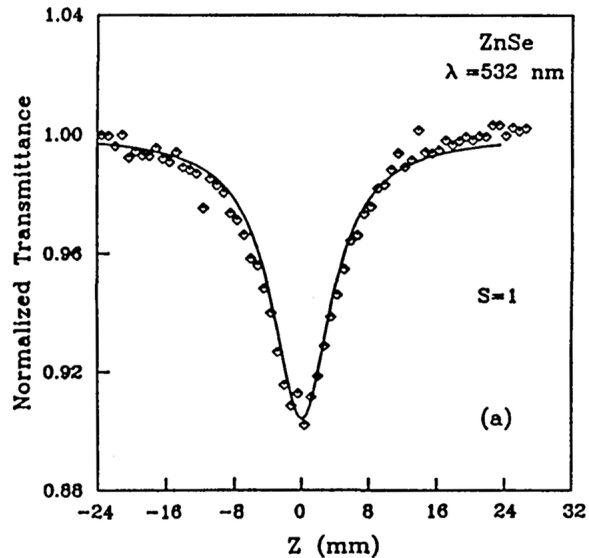


Figure 8: Z-scan transmittance data in ZnSe, from [30]. The focal point of the beam ($Z = 0$ in this plot) is determined from the minimum of the curve.

Pump-probe

The development of time-resolved pump-probe techniques has enabled many new experiments related to multiphoton absorption, and particularly the dynamics of multiphoton-generated carriers. [26, 27, 45, 46] In these experiments, a strong pump pulse perturbs the system under study by some absorption mechanism, and a subsequent weak probe pulse measures the effect of the pump. By adjusting the time delay between the pump and probe pulses, time-dependent data may be obtained, with

resolution down to the order of femtoseconds. For instance, Krishnamurthy et al. [26] used a pump-probe technique to observe the decay of 2PA-generated carriers in InAs on a nanosecond timescale, as shown in Figure 9.

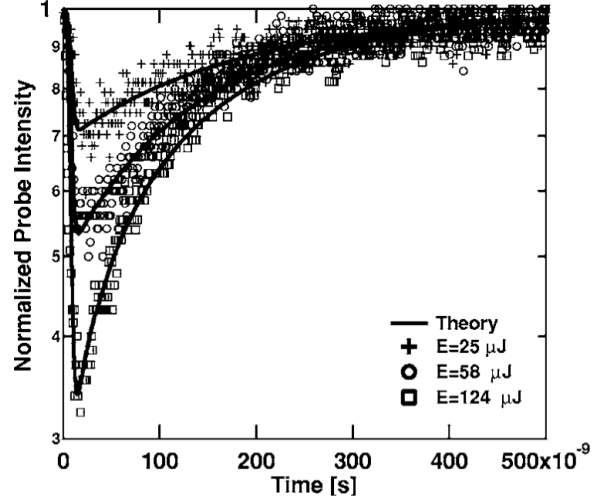


Figure 9: Pump-probe transmittance in InAs, from [26]. Specimens were pumped at $4.8\ \mu\text{m}$ to generate free carriers by two-photon absorption, then probed at $5.3\ \mu\text{m}$ to observe the decay of the generated carriers.

II.2 Nonlinear Absorption in Germanium

II.2.1 Theory

The study of two-photon absorption in indirect semiconductors such as silicon and germanium is complicated by the fact that at some wavelengths the direct and indirect two-photon transitions may be competing. In 1972, Bassani and Hassan [47] reported an analysis of indirect two-photon absorption in semiconductors using third-order time-dependent perturbation theory. They did not derive a two-photon absorption coefficient for germanium, but they did employ a detailed analysis of selection rules to conclude that, for an indirect two-photon transition, the only phonon type that may

participate is longitudinal optical. This result was later confirmed experimentally by Tuncel et al. [48] (see description on page 19, below).

In a 1982 report, G. W. Bryant et al. [49] performed detailed computer simulations of the interaction of 2.7- μm photons with electrons and holes in germanium. The primary objective of these simulations was to investigate the remarkable result of Danileiko et al. [50] that Ge could not be damaged by intense infrared laser pulses. They found that the damage process required very high optical intensities to generate the necessary carriers via two-photon absorption, and therefore that the damage threshold did not depend solely on total pulse energy.

The model used by Bryant et al. was based on that of Elci et al., [51] but modified for two-photon absorption. The model accounted for intraband free-carrier absorption and inter-valence band one-photon absorption, and also considered the carrier and lattice temperatures, tracking the energy distribution of carriers in several relevant valleys. The thermalization of the carrier plasma and subsequent phonon-assisted thermalization with the lattice were also modeled. One aspect that was not considered was the modulation of the pulse profile as it propagates through the specimen; they used a thin-sample approximation. In addition, they did not consider the self-focusing of the beam brought on by the free carrier generation. Although they mentioned plans to include such effects in future work, it seems that this work was never carried out.

In a recent theoretical report, [52] Garcia and Avanki have studied the wavelength dependence of direct and indirect two-photon absorption in germanium. However, since that report directly utilizes results from the present work, it will be discussed after the experimental outcomes are presented in Section III.3.1.

II.2.2 Experiments

Two-photon absorption in germanium was first reported experimentally in 1969 by Zubov, et al. [53]. Using a wavelength of $2.36\ \mu\text{m}$ in a direct transmission experiment on a 1-cm specimen, they derived a two-photon absorption coefficient of $\beta = 1000\ \text{cm/GW}$. However, their analysis ignored free carrier absorption effects and multiple internal reflections of the pulse.

Wenzel et al. [54] reported a similar experiment in 1973. They used a spectral laser source to produce ~ 90 -ns pulses containing a range of wavelengths from 2.6 – $3.1\ \mu\text{m}$, and reported a β of $2500\ \text{cm/GW}$. Although they considered multiple internal reflections in their analysis, they also ignored free carrier effects. At the conclusion of their paper, they suggest the usefulness of photoconductivity experiments.

Gibson et al. performed both photoconductivity and direct transmission experiments on germanium specimens, as reported in their paper from 1976. [40] They took into account the free carrier contribution to the absorption, and noted the resulting change in pulse shape. Their laser was similar to that of Wenzel et al., covering a range of wavelengths from 2.6 – $3.0\ \mu\text{m}$, but with a pulse duration of $480\ \text{ns}$. Figure 10(a) shows their intensity-dependent direct transmission results at several different specimen thicknesses. From these data they derived a wavelength-averaged β of $160\ \text{cm/GW}$. Figure 10(b) shows the values of β they derived using photoconductivity. These range from ~ 100 – $700\ \text{cm/GW}$, depending on wavelength. As expected, their value for β appears to approach zero as the wavelength approaches $3.07\ \mu\text{m}$, corresponding to one half the direct gap in germanium.

In conference proceedings from 1978, Danileiko et al., [50] who were primarily interested in laser-induced damage thresholds, reported in passing a two-photon absorption coefficient of $75\ \text{cm/GW}$ in Ge at $2.76\ \mu\text{m}$. They used 90 -ns pulses from a pulsed $\text{CaF}_2:\text{Er}^{3+}$ laser in a photoconductivity experiment, but did not report any further details.

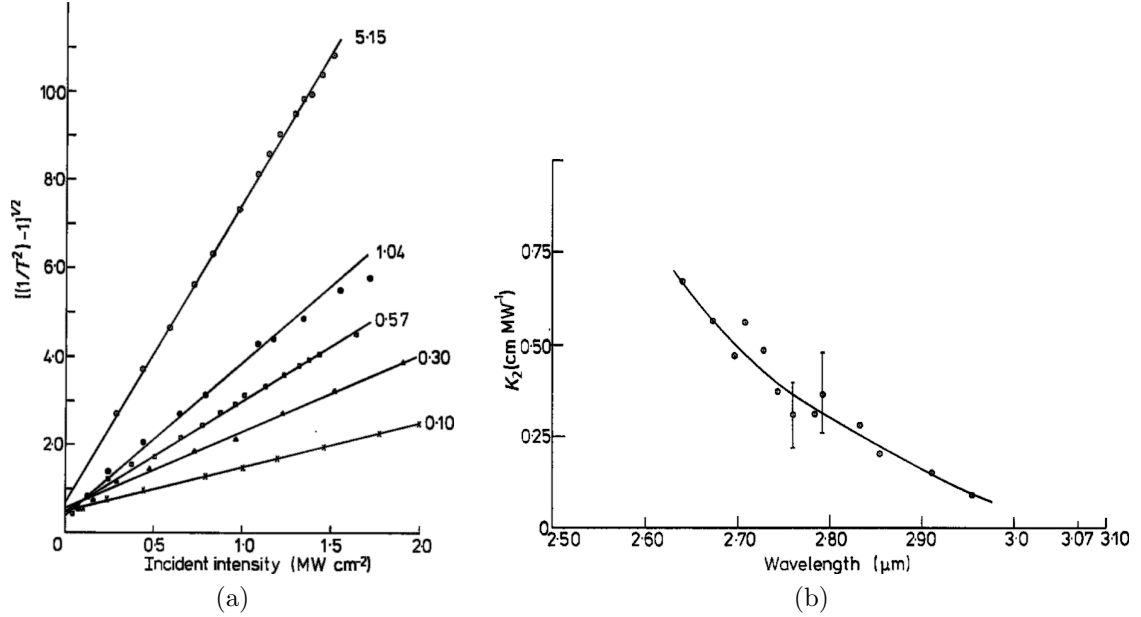


Figure 10: Transmittance and photoconductivity results in Ge from Gibson et al. [40] (a) Adjusted inverse transmission vs. incident intensity from the direct transmission experiment. The numbers at the end of each line denote specimen thickness, in cm. (b) Experimental values of β (K_2) vs. wavelength, derived from photoconductivity data.

In 1993 Tuncel et al. [48] used the Vanderbilt Free Electron Laser to study the wavelength dependence of germanium two-photon absorption in photoconductivity experiments. Due to the complex nature of the FEL pulse structure (Section III.1.1), they did not derive explicit values of β . However, they did observe indirect-gap two-photon absorption, and estimated the ratio β_d/β_i to be ~ 2000 . In addition, they confirmed the theoretical result of Bassani and Hassan, [47] which stated that this transition may only be assisted by longitudinal optical phonons (see Figure 11 on page 21).

Rauscher and Laenen [46] used picosecond pump-probe spectroscopy to study two-photon absorption in germanium in 1996. They used a tunable mode-locked laser to produce $2.9 \mu\text{m}$ pulses of length 1–2 ps. Using just the pump pulse in a direct transmission experiment, they estimated β for germanium to be $80 \pm 10 \text{ cm/GW}$. They included free carrier absorption in their analysis, which they attributed primarily to

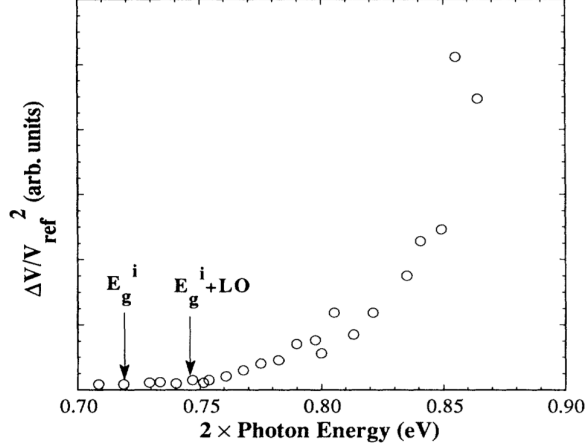


Figure 11: Indirect 2PA photoconductivity vs. photon energy in Ge, from [48]. The onset of absorption occurs at the energy of the indirect gap plus 30.4 meV, which is the energy of the LO phonon predicted to enable this transition. [47]

the transition of a heavy hole to the split-off band, after Bryant, et al. Following that, they used the same pump beam and a weaker probe beam tuned to 3.0 μm to determine the non-degenerate $\beta(2.9 \mu\text{m}, 3.0 \mu\text{m})$ to be $35 \pm 10 \text{ cm/GW}$. The results of this experiment are shown in Figure 12 on page 22. The fast peak is interpreted to be the non-degenerate absorption, as evidenced by its intensity-dependence, shown in the inset.

T. J. Wagner et al. [55] have recently studied nonlinear absorption in Ge and GaSb at 2.05 and 2.5 μm using both nanosecond and picosecond sources with an irradiance-scan approach. They carefully considered several effects that may influence the measurement, and accounted for free-carrier absorption by simultaneously fitting the two-photon and free-carrier absorption coefficients to their experimental data. They derived a value of 68 cm/GW for the two-photon coefficient, β at 2.5 μm .

Summary

Figure 13 shows the experimentally-derived values of the two-photon absorption coefficient of germanium, by year. Table 1 on page 24 contains the same information, with

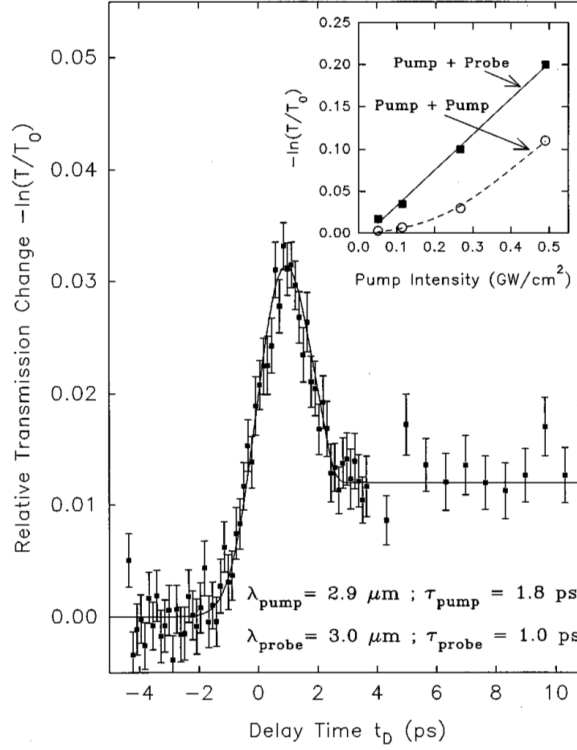


Figure 12: Nonlinear pump-probe spectroscopy of Ge from [46]. Here, the probe transmission is plotted vs. time delay with respect to the pump. (An increase on the y axis indicates decreasing probe transmission.) The fast peak at zero time delay is attributed to the simultaneous absorption of one pump and one probe photon. The inset shows the linear pump intensity-dependence of the magnitude of the fast peak (black squares), suggesting that only one pump photon contributes to the process. The hollow circles in the inset show the quadratic intensity dependence of the pump-only absorption, for comparison. The probe intensity is too weak in this experiment for significant probe-probe absorption.

the addition of the wavelengths used and notes on each experiment. The reported value for the current work at will be discussed in Chapter III.

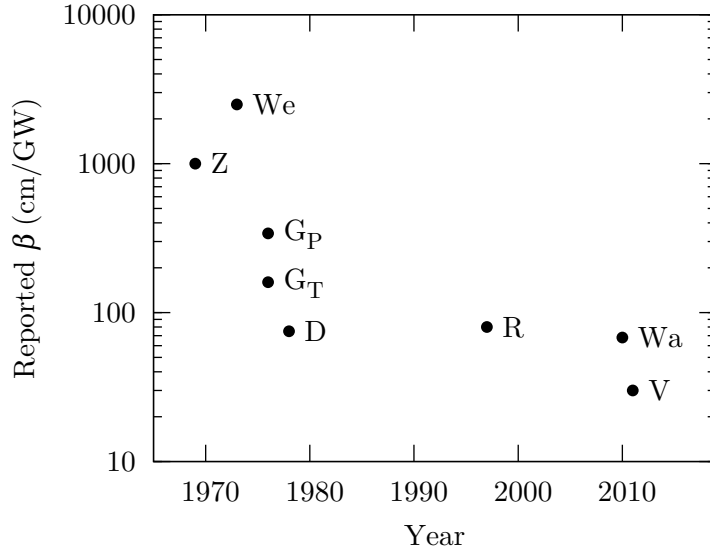


Figure 13: Reported experimental values for the germanium two-photon absorption coefficient β near $2.8 \mu\text{m}$, by year. The points are keyed as follows: Z = Zubov et al. [53], We = Wenzel et al. [54], G_P = Gibson et al. (photoconductivity) [40], G_T = Gibson et al. (direct transmission), D = Danileiko et al. [50], R = Rauscher and Laenen [46], Wa = Wagner et al. [55], V = Current work at Vanderbilt [56].

The reported values of β generally trend downward with time. This may be due to multiple factors:

- (i) The inclusion of free carrier effects significantly lowers the value of β derived from experimental data.
- (ii) The shorter pulses available in more recent laser systems decrease free carrier effects.
- (iii) More recent experiments are able to use higher-power lasers, and this may reduce the measurement of β . (Compare Gibson’s high-intensity transmission data to the lower-intensity photoconductivity data.)

Table 1: Reported experimental values for the germanium two-photon absorption coefficient β .

Reference	Year	Wavelength (μm)	β (cm/GW)	Notes
Zubov [53]	1969	2.36	1000	Ignored multiple reflections and free carrier absorption.
Wenzel [54]	1973	2.6—3.1	2500	Ignored free carrier absorption.
Gibson [40]	1976	2.6—3.0	340	Photoconductivity.
			160	Direct transmission. Both experiments by Gibson included free carrier absorption in the analysis.
Danileiko [50]	1978	2.76	75	Little detail available.
Rauscher [46]	1997	2.9	80	Included free carrier absorption.
Wagner [55]	2010	2.5	68	Simultaneous fit of two-photon and free-carrier absorption coefficients.

(iv) Higher-purity specimens of germanium are more readily available as time progresses.

II.3 Carrier Dynamics in Germanium

Research on two-photon absorption in germanium and other materials has demonstrated that knowledge of the dynamics of the photogenerated carriers is crucial for the accurate evaluation of absorption phenomena. [24, 40] In fact, the dynamics of hot carriers in germanium has been a topic of interest in its own right for the last several decades.

In 1972, Müller et al. [57] reported a fast modulation in CO_2 laser absorption by germanium, which they attributed to absorption by hot carriers, with an estimated cooling time of 1 ps.

Kennedy et al. in 1974 [58] reported the use of $1.06\ \mu\text{m}$ pulses of duration $< 5\ \text{ps}$ in a pump-probe experiment to measure the relaxation time of hot carriers. They saw a fast peak in transmittance at zero time delay, which they attributed to saturation of excited carrier states, and thus determined that the hot carrier relaxation time was faster than their pulse width, *i.e.* $< 5\ \text{ps}$.

However, the following year Shank and Auston [59] reinterpreted the zero-time-delay spike in transmittance as an autocorrelation of the pump and probe beams due to a transient grating phenomena generated by the interaction of the electric fields of the two pulses. In addition, in their own pump-probe experiment, which was very similar to that of Kennedy et al., they observed a slow decay in transmittance (Figure 14 on page 25), which was attributed to carrier diffusion out of the probe beam area.

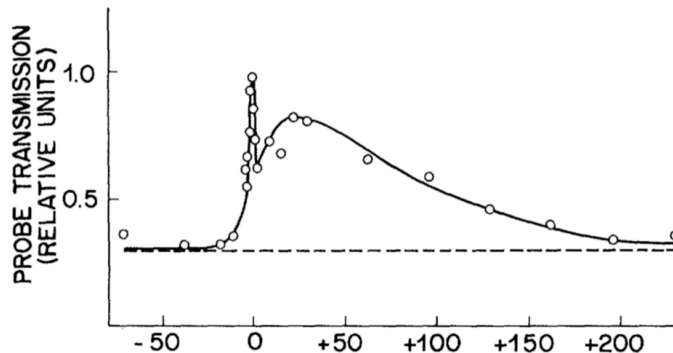


Figure 14: Time-resolved pump-probe transmission of $1.06\ \mu\text{m}$ photons in germanium, from Shank and Auston. [59] The horizontal axis is pump-probe time delay, in ps.

In Reference [60] from the next year, the authors of the original 1974 paper by Kennedy et al. [58] responded in agreement with the interpretation of Shank and Auston, and presented new temperature-dependent pump-probe results, which showed a greater rise in probe transmission saturation for low temperatures, as depicted in Figure 15(a). Following the initial rise in probe transmittance, there is a slow decay,

shown in Figure 15(b). The authors suggest the following interpretation: the pump pulse excites photogenerated carriers into high energy states. These carriers subsequently cool toward the band edge via phonon emission. The 1.06 μm probe photons in this experiment effect a transition above the germanium band edge, but below the energy of the hot carriers. As the pump-excited carriers cool to the probe excitation point, they fill available probe excitation states, and the probe transmission increases. At later time delays, after the pump-generated carriers have decayed down to the conduction band minimum, the probe transmission decreases again.

In 1989, A. Othonos et al. [61] reported results of picosecond Raman scattering and transient absorption experiments on germanium specimens using 4-ps pulses at 575 nm. From the Raman scattering experiment, they demonstrated the existence of a non-equilibrium population of optical phonons, which are generated as hot carriers in the L valley thermalize with the lattice. The lifetime of these phonons suggests that the plasma-lattice thermalization occurs on the order of tens of ps. They theoretically predicted the optical phonon occupation number as a function of time within a factor of two of the experimental data. They also found from the reflectivity experiment that the hot carriers diffuse quickly into the specimen at an enhanced temperature-dependent ambipolar diffusion coefficient, and that this effect must be considered to accurately model the experimental data.

Zhou et al. [62] in 1994 reported femtosecond pump-probe transmission and photoluminescence measurements demonstrating that photo-excited electrons in the Γ valley scatter to the L valley with a time constant of 230 ± 25 fs at room temperature. (See Figure 16). They estimated a similar time-scale for scattering to the X valley. In fact, their data suggests that carrier thermalization, intervalley scattering, and cooling all occur on a sub-picosecond timescale. With regard to the previous experiments in this area, the authors suggest that the faster timescales reported in the work are due to the femtosecond laser source they used. In a follow-up experiment from

1995, Mak and Rüle [63] found that the thermalization time for excited carriers in germanium scales with the excited carrier density N as $N^{-0.55}$.

Summary

To summarize the recent results of carrier dynamics in Ge, it is believed that photo-generated electrons in the Γ valley undergo the following processes:

- (i) Equilibration in momentum space without energy loss, on the order of 10 fs. (Although this is not explicitly mentioned in the literature reported here, it is generally understood.)
- (ii) Carrier-carrier thermalization due to Coulomb interactions within the plasma, of order 100 fs.
- (iii) Electron-phonon scattering from the Γ valley to the X and L valleys, of order 100 fs.
- (iv) Phonon-assisted relaxation down to the band edge, on a timescale of hundreds of fs. According to Mak and Rüle, [63] this transition is forbidden near the bottom of the Γ valley.
- (v) Recombination with holes. The lifetime for generated carriers is on the order of hundreds of μ s, depending on doping. [64]

An accurate evaluation of the importance of these effects will be critical in the experimental analysis and simulation of multiphoton absorption.

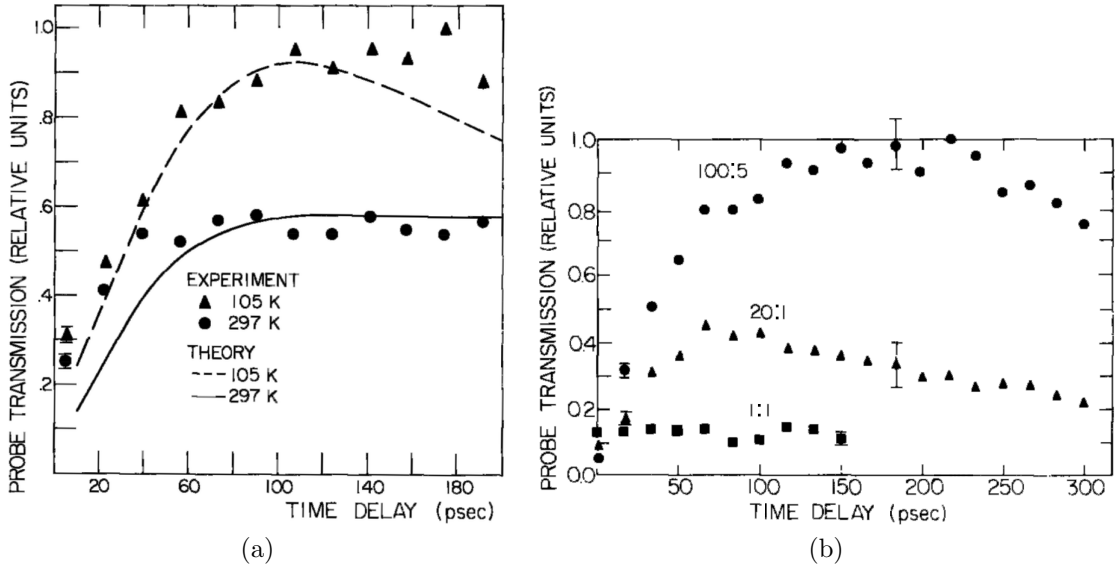


Figure 15: Temperature-dependent pump-probe transmittance in Ge, from [60]. (a) Temperature dependence of the initial rise in transmittance, along with theoretical curves calculated by the authors. (b) Low-temperature rise and decay of probe transmittance at different ratios of pump and probe intensity. The displayed error bars are typical of all data points.

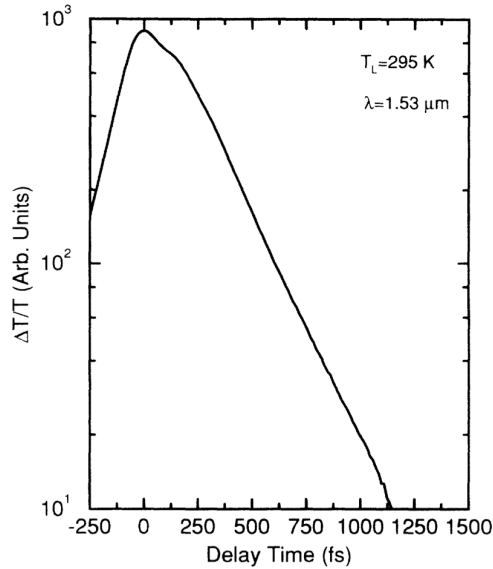


Figure 16: Time-resolved probe transmission in germanium, from [62]. Carriers are pumped near the band edge, thus the decay in transmission is attributed to the scattering of pumped carriers from the Γ valley to the L valley, with a time constant of 230 ± 25 fs.

CHAPTER III

EXPERIMENT AND SIMULATION

This chapter begins by describing in detail the experimental techniques used in these studies, including the determination of the critical quantities of the beam diameter and free carrier absorption coefficients. Then the results of the transmission experiments are presented, along with the simulation code that was used to extract the multiphoton absorption coefficients. Finally, the significance of the coefficients and their ratios are discussed, and comparison is made to other experimental and theoretical works.

III.1 Methodology

III.1.1 Vanderbilt Free Electron Laser

The Vanderbilt University Free Electron Laser (FEL) provides a high-power beam in the mid-IR with wavelength selectivity from 2 to 9 μm . [65] The beam consists of a 30-Hz train of 5 μs macropulses, each containing approximately 14,000 one-ps micropulses with 350 ps separation. These pulse structures are shown schematically in Figure 17. The macropulse-to-macropulse energy fluctuations are a source of random error, typically $\pm 5\%$, and the error becomes smaller as higher macropulse energies are used. For example, 1 ± 0.05 mJ and 10 ± 0.2 mJ have been observed. Micropulse-to-micropulse fluctuations are less than 10%. [66] The micropulses are nearly transform-limited as measured by autocorrelation, and are assumed to have a Gaussian temporal profile. Although individual micropulse chirping is minimal, the wavelength of the micropulses could vary over the course of the macropulse by as much as 50 nm for the shorter wavelengths studied and as much as 100 nm for the longer wavelengths. Spatially, the FEL beam profile is very near to Gaussian.

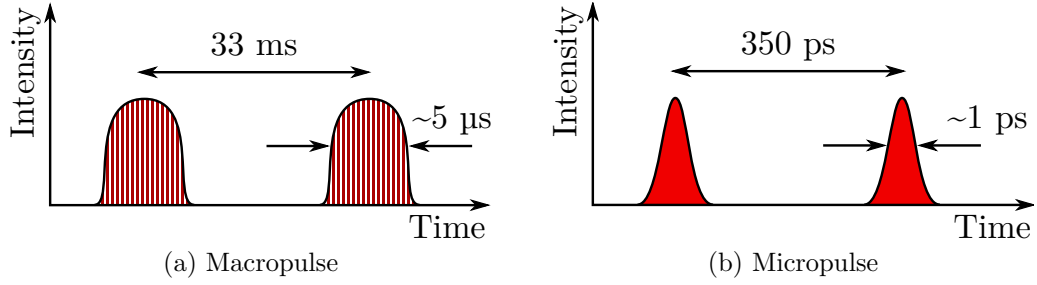


Figure 17: Vanderbilt FEL temporal pulse structure.

III.1.2 Transmission Measurement

Double-side polished, 0.5 mm-thick near-intrinsic n-type Ge(100) specimens were used in these studies. The specimens had a resistivity of $\sim 50 \Omega\cdot\text{cm}$, corresponding to a free carrier concentration in the range of 10^{13} – 10^{14} cm^{-3} . All experiments were performed in air at room temperature.

The linearly polarized FEL output energy was adjusted using a rotating Brewster’s angle Ge attenuator, and the radiation was focused onto the Ge specimen using a ZnSe lens with 250 mm focal length. (In polarization experiments with this apparatus, the absorption showed no measurable dependence on incident polarization). Incident and transmitted laser energies were measured using a power meter, as depicted in Figure 18.

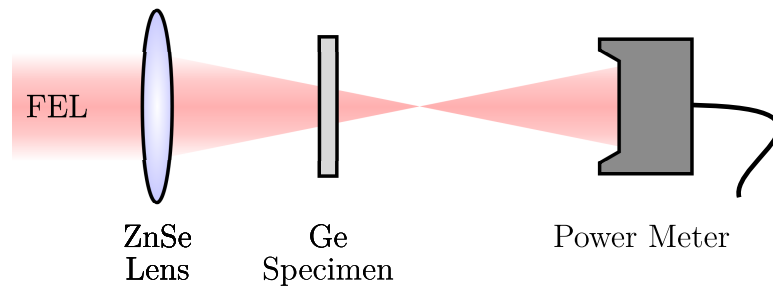


Figure 18: Experimental setup for measuring multiphoton absorption in germanium.

For all wavelengths studied, strong nonlinear absorption and material removal (ablation) were observed whenever the specimen was placed at the focal point, even at low macropulse energies ($E_M < 3$ mJ). [67] Therefore, for all wavelengths the transmittance was measured with the specimen at a fixed distance from the lens of 24 cm, not at the focal point, permitting the use of higher macropulse energies (up to 30 mJ) and increasing the range of incident intensities in the experiment.

III.1.3 Beam Diameter

The beam diameter at the specimen and the free carrier absorption coefficients are critical values for the characterization of nonlinear interactions between the specimens and the FEL beam. To calibrate the beam diameter, a z -scan technique was used to determine the focal point of the lens at different wavelengths, as shown in Figure 19. The focal length was found to increase linearly with increasing wavelength. Since the FEL beam diameter does not vary significantly with wavelength, a linear relationship between the beam wavelength and the beam diameter at the fixed specimen position was assumed. FWHM beam diameters at the specimen position for 2.8 μm and 5.2 μm were determined by setting the incident beam fluence to twice the damage threshold for those wavelengths and measuring the diameters of the resultant damage spots (see Figure 20). The beam diameters for the intermediate wavelengths were then interpolated linearly. This ‘damage spot’ method was found to be in agreement with the knife-edge method in a comparison of the two at the focal point.

III.1.4 Free Carrier Absorption Coefficients

To determine the wavelength-dependent free carrier absorption coefficients σ_n (electrons) and σ_p (holes), the FTIR spectra of heavily doped n-type ($N_n \sim 7 \times 10^{17} \text{ cm}^{-3}$) and p-type ($N_p \sim 2.5 \times 10^{16} \text{ cm}^{-3}$) Ge specimens were measured and compared to the spectrum for the near-intrinsic specimen. The results are summarized in Table 2.

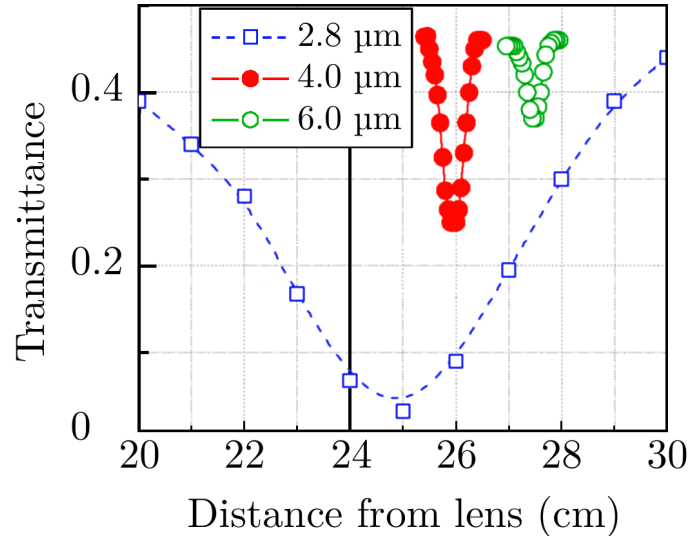


Figure 19: Z-scan measurements for 2.8 μm , 4.0 μm , and 6.0 μm , revealing a linear relationship between FEL wavelength and focal point location. Actual transmission measurements for all wavelengths were performed at the fixed specimen position of 24 cm from the lens, as indicated by the solid vertical line.

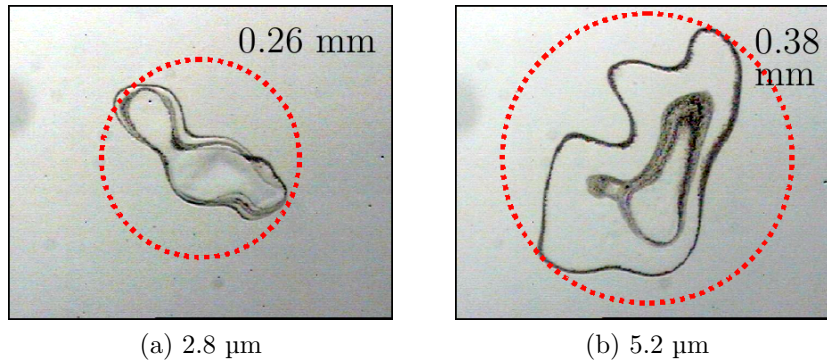


Figure 20: Optical microscopy images of FEL-ablated germanium, for determination of the FEL beam diameter. Measured beam diameters are marked by the dotted circles. Irregularities in the spots may be attributed to damage nucleation mechanisms in addition to irregularities in the FEL beam.

The values at 2.8 μm are comparable to previously reported measurements. [68] Since the majority of free carriers encountered by the photons in the FEL beam will already have relaxed to the band edge, [62] this method is believed to provide realistic absorption coefficients for this experiment.

Table 2: Absorption cross-sections in Ge for electrons (σ_n) and holes (σ_p) as measured by low-intensity FTIR.

λ (μm)	σ_n (10^{-17} cm^2)	σ_p (10^{-16} cm^2)
2.8	0.72	1.4
3.2	0.78	1.5
3.6	0.87	1.3
4.0	0.95	0.95
4.4	1.06	0.8
4.8	1.17	1.0
5.2	1.32	0.7

During the 350 ps between FEL micropulses, it is expected that photo-generated carriers will have sufficient time to relax to the lowest level excited states, including the relaxation of Γ valley electrons to the L valley, but not enough time to undergo any substantial recombination, even at the very high concentrations generated. The 33 ms between macropulses is sufficient for the entire electronic system to recover to the ground state via recombination, [69] with essentially no excited carriers remaining.

III.2 Results

III.2.1 FEL Transmittance in Germanium

Figure 21 shows transmittance as a function of incident micropulse peak intensity for wavelengths ranging from 2.8 μm to 5.2 μm , at 0.4 μm intervals. The measured incident macropulse energy E_M was converted into the micropulse peak intensity I_μ

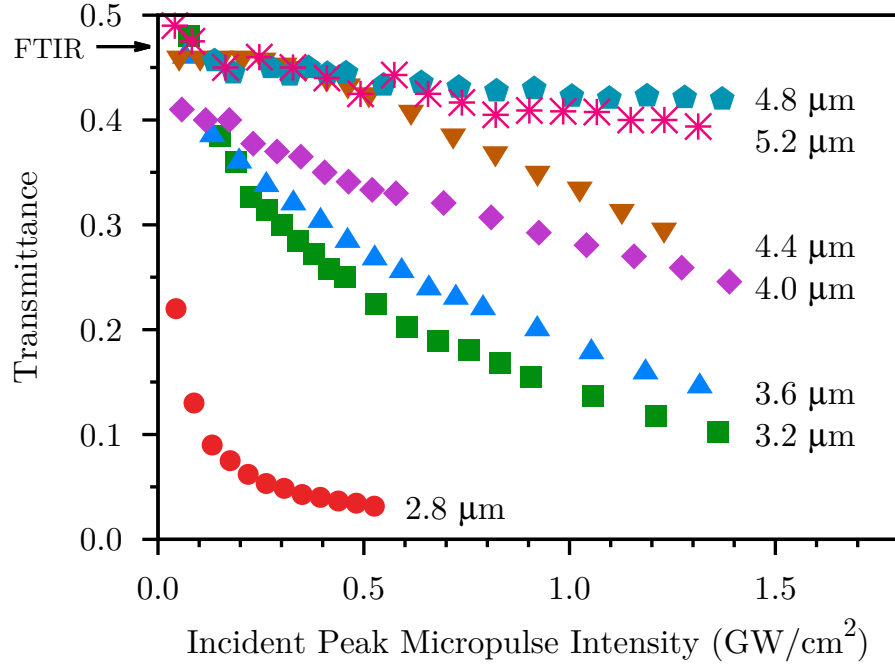


Figure 21: Transmittance as a function of incident micropulse peak intensity for the seven wavelengths studied. FTIR on the Ge sample shows a transmittance of 0.47 at low power (black arrow, upper left).

according to the following equation:

$$I_{\mu} = \frac{E_M/14000}{\pi^{3/2}r_0^2t_0} \quad (16)$$

where r_0 is the HWe^{-1}M beam radius and t_0 is the HWe^{-1}M micropulse length ($\text{HWe}^{-1}\text{M} = \text{FWHM} / 1.66511$). Fourier transform infrared (FTIR) measurements were also performed to establish the low-power transmittance of the specimens at the wavelengths studied. At $4.0 \mu\text{m}$, the low-intensity limit did not approach the FTIR transmittance as expected, rendering suspect the result at that wavelength. This anomaly is believed to be due to instability in the FEL beam during measurement.

The data separate into four groups at high intensity, with a general trend of decreased absorption for higher-order processes. The fast transmittance decrease at $2.8 \mu\text{m}$ (0.44 eV) as a function of incident intensity is attributed to two-photon

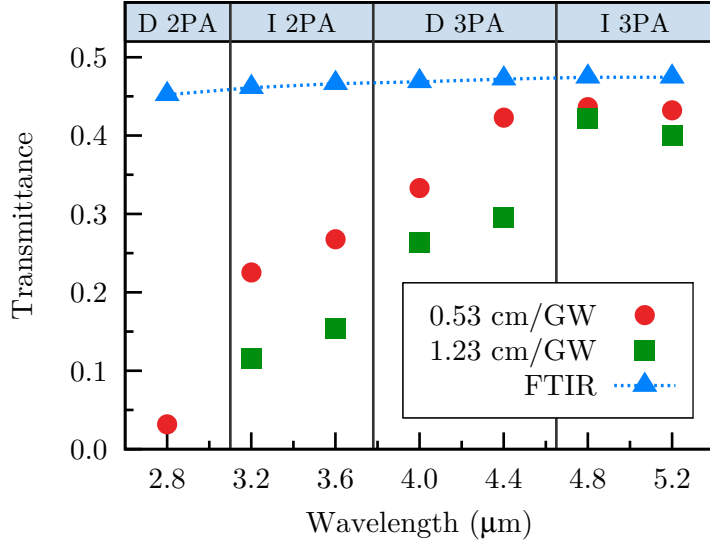


Figure 22: Transmittance cross-sections at two incident peak intensities, showing wavelength dependence, along with the low-intensity FTIR transmittance. The attributed absorption regimes (direct 2PA, etc.) are noted at the top of the plot.

absorption across the direct band gap (~ 0.8 eV). The intermediate decrease at $3.2 \mu\text{m}$ (0.39 eV) and $3.6 \mu\text{m}$ (0.34 eV) is attributed to 2PA across the indirect band gap (0.66 eV). We attribute the relatively slow transmittance decrease at $4.0 \mu\text{m}$ (0.31 eV) and $4.4 \mu\text{m}$ (0.28 eV) to direct three-photon absorption (3PA), and the small decrease in transmittance observed at $4.8 \mu\text{m}$ (0.26 eV) and $5.2 \mu\text{m}$ (0.24 eV) to indirect 3PA.

Figure 22 shows the same data as a function of wavelength at two different intensities, highlighting the dramatic change in transmittance between the various absorption regimes. These differences are especially clear in the high-intensity (1.23 cm/GW) curve. The low-intensity FTIR transmittance is also shown, for comparison.

III.2.2 Simulation

The transmission curves shown above were analyzed using the following theoretical model. The nonlinear absorption of optical pulses at sub-band-gap wavelengths may

be described by the equation:

$$\frac{\partial I}{\partial z} = -\beta I^2 - \gamma I^3 - (\sigma_n + \sigma_p)NI, \quad (17)$$

where I is the intensity of the pulse as a function of space and time, β is the two-photon absorption coefficient (units cm/GW), γ is the 3PA coefficient (cm³/GW²), and the last term describes free carrier absorption. The time evolution of the local free carrier concentration N is described as:

$$\frac{\partial N}{\partial t} = \frac{\beta I^2}{2\hbar\omega} + \frac{\gamma I^2}{3\hbar\omega} + D \frac{\partial^2 N}{\partial z^2} - \frac{N}{\tau} - AN^3. \quad (18)$$

Here the first and second terms refer to two- and three-photon absorption, respectively, with $\hbar\omega$ as the energy of the absorbed photons. The third term refers to free carrier diffusion with ambipolar diffusion coefficient $D = 67$ cm²/s, [70] the fourth term to radiative recombination with lifetime $\tau = 100$ μ s, [69] and the final term to Auger recombination with Auger coefficient $A = 2 \times 10^{31}$ cm⁶/s. [71, 72]

This pair of coupled differential equations was solved numerically using a time- and space-discret pulse propagation simulation, with consideration given to the spatial and temporal profiles of the micropulses (assumed to be Gaussian in both cases), multiple reflections inside the sample using the usual Fresnel coefficients, and to the accumulation of carriers between micropulses. The simulation code was verified for accuracy by comparison with simpler analytical models. The possible effects of surface recombination, temperature rise due to carrier relaxation, and bleaching due to relaxed state filling were all considered and found to be negligible.

Using the two- and three-photon absorption coefficients as parameters, the output of the simulation code was fit to the experimental results from Figure 21. Excellent agreement was found between fit parameters and the experimental data in all cases except the 4.0 μ m case, where, as noted before, the low-intensity transmittance does

not approach the FTIR result. Figure 23 shows the typical agreement using the representative cases of 2.8 μm and 4.4 μm .

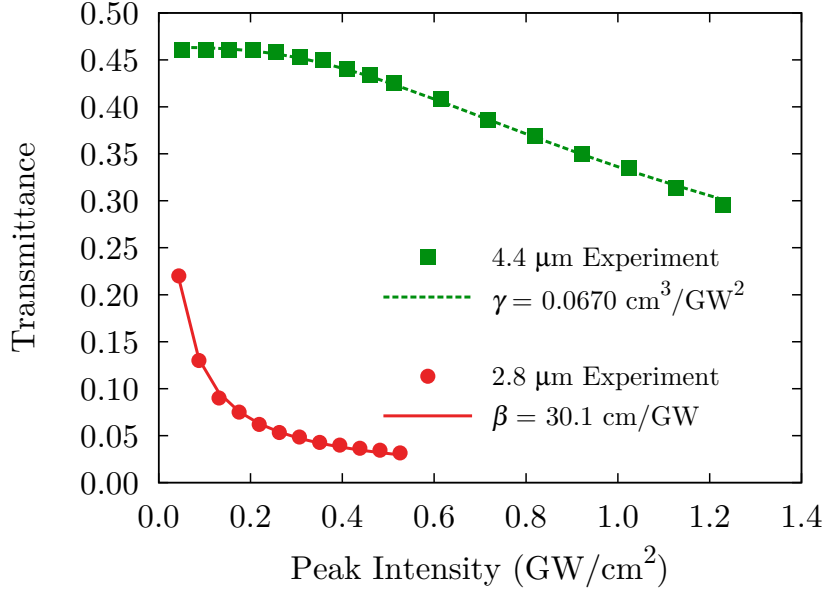


Figure 23: Fitting agreement between the simulation code and the experimental results for the representative cases of 2.8 μm and 4.4 μm .

III.2.3 Beam Propagation and Carrier Concentrations

The simulations provide information about pulse intensity and carrier concentration throughout the sample depth. For instance, when the absorption was low, which occurred at low incident intensities for the shorter wavelengths and at all intensities for the longer wavelengths, a relatively even carrier distribution was produced. In these cases, the micropulses tended to lose their energy gradually as they traversed the sample. At the weakest intensity for 2.8 μm , for example, after the complete macropulse had traversed the sample, the carrier concentration near the front surface was $1.1 \times 10^{18} \text{ cm}^{-3}$ and decayed exponentially toward the back surface, where it was $2 \times 10^{17} \text{ cm}^{-3}$.

When the absorption was high, as in the high-intensity, shorter-wavelength case, the micropulses tended to lose most of their energy quickly upon entering the sample, resulting in greater carrier concentrations near the front surface. For example, after the highest-intensity 2.8 μm macropulse had traversed the sample, the front surface carrier concentration was $6 \times 10^{18} \text{ cm}^{-3}$, and decayed exponentially to a back surface carrier concentration of $2 \times 10^{17} \text{ cm}^{-3}$, as in the low-absorption case.

In either case, for a given FEL macropulse, the carrier concentrations increased steadily with each micropulse until competition with recombination processes caused the system to approach a quasi-steady state. In the high-absorption regime, this state was reached after a few hundred micropulses. In the low-absorption regime, several thousand were required to reach it, or it was not reached at all. For instance, at the highest intensity studied for 4.8 μm , the carrier concentration never reached steady state, and was $\sim 2 \times 10^{16} \text{ cm}^{-3}$ throughout the entire sample depth at the end of the macropulse.

III.2.4 Fitted Absorption Coefficients

Tables 3 and 4 list the fitted absorption coefficients β and γ for the wavelengths studied. The same coefficients are plotted in Figure 24. In the 2PA data, there is a distinct change in the absorption coefficients between the direct and indirect regimes. In the 3PA data, this difference is not so pronounced. The decreased absorption in the indirect regimes is reasonable considering the need for phonon assistance in exciting carriers to the indirect valley. In addition, the less pronounced difference in the 3PA data may be attributed to the greater number of absorption pathways generally available in 3PA, as recently shown by Cirloganu et al. [18]

Table 3: Fitted two-photon absorption coefficients for the transmission data shown in Figure 21. Here, $x = 2\hbar\omega/E_g$, where E_g may refer to either the direct (0.8 eV) or indirect (0.67 eV) gap.

λ (μm)	Absorption Type	x	Fitted β (cm/GW)
2.8	Direct	1.11	30.
3.2	Indirect	1.17	0.16
3.6	Indirect	1.04	0.090

Table 4: Fitted three-photon absorption coefficients for the transmission data shown in Figure 21. Here, $x = 3\hbar\omega/E_g$, where E_g may refer to either the direct (0.8 eV) or indirect (0.67 eV) gap.

λ (μm)	Absorption Type	x	Fitted γ (cm^3/GW^2)
4.0	Direct	1.16	0.27
4.4	Direct	1.06	0.067
4.8	Indirect	1.16	0.0050
5.2	Indirect	1.07	0.013

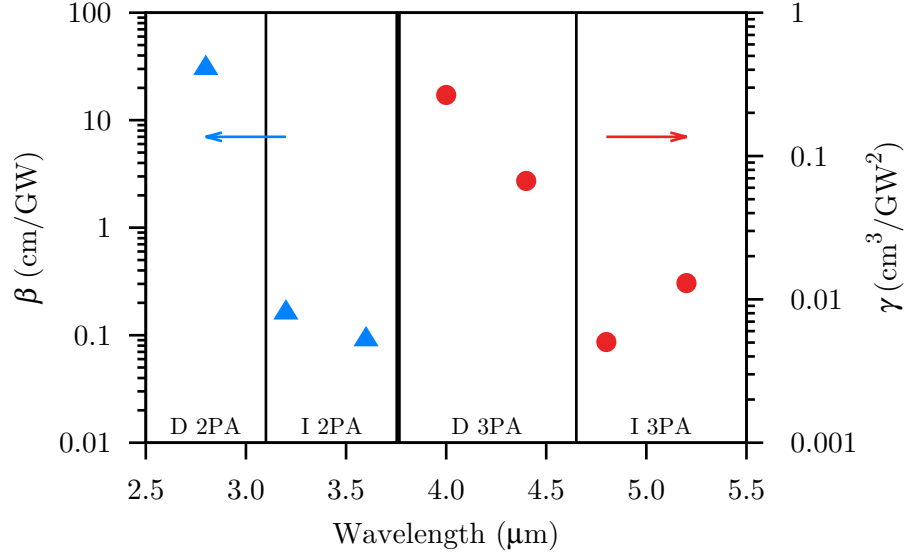


Figure 24: Fitted absorption coefficients for the transmission data shown in Figure 21. The triangles are 2PA coefficients (left vertical axis) and the circles are 3PA coefficients (right vertical axis).

III.3 Analysis

III.3.1 Comparison to Literature

Previous works have reported the 2PA coefficient in Ge near 2.8 μm . These are listed in Table 5. The derived value of β at 2.8 μm in the present work (30 cm/GW) is a factor of five less than the earliest observations at similar wavelengths, [40] and is a factor of two less than the more recent measurements. [46, 55] The current result has also been compared to predictions based on Wherrett’s scaling rule, [20] which has been remarkably successful in predicting the nonlinear behavior of a variety of direct-gap materials. [21] At 2.8 μm , Wherrett scaling predicts $\beta = 40.9$ cm/GW, which is consistent with current result, and is evidence that multiphoton absorption theory for direct-gap materials is applicable to direct transitions in indirect-gap materials. For the direct 3PA wavelengths, the Wherrett scaling overestimates the coefficients by factors of 40 for 4.0 μm and 225 for 4.4 μm . However, theoretical studies [73] have shown that more complex models are necessary to accurately describe 3PA behavior.

Table 5: Selected literature values for β in Ge near 2.8 μm , along with the result of the current work.

Work	Year	λ (μm)	β (cm/GW)
Gibson [40]	1976	2.6—3.0	160
Rauscher [46]	1997	2.9	80
Wagner [55]	2010	2.4—2.51	68
This Work	2011	2.8	30

In a recent theoretical work, Garcia and Avanki [52] have applied direct and indirect gap two-photon absorption calculations to Ge using the experimental results from the current work. [56] Their approach employs a single fitting parameter, $f(\theta, \phi)$. When their model is applied to the current experimental result, they find $f(\theta, \phi) =$

0.124 for the direct case and $f(\theta, \phi) = 0.11$ for the indirect case. The fact that these two independent fitting parameters are in such good agreement is seen as a validation of the current result. Figure 25 shows the theoretical wavelength-dependence of β in Ge for both the direct and indirect cases, with $f(\theta, \phi) = 0.117$, the mean value of the direct and indirect results.

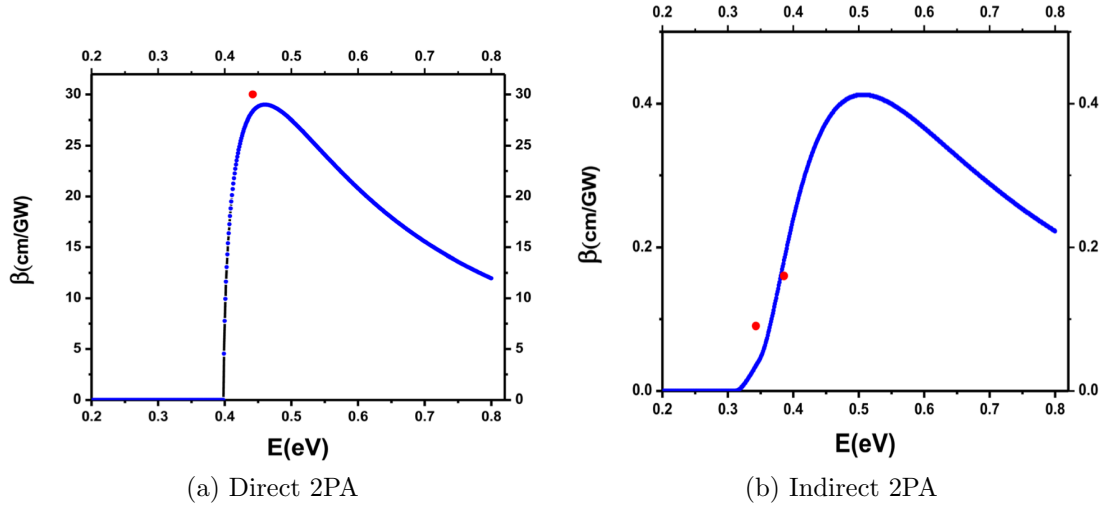


Figure 25: Theoretical wavelength dependence for direct and indirect 2PA in germanium, from [52]. The blue curves show the theoretical value for β , with the single fitting parameter $f(\theta, \phi) = 0.117$, and the red dots are the experimental results from this work.

III.3.2 Limitations in the Derived Coefficients

The coefficients listed in Tables 3 and 4 are subject to a few caveats. One is due to the uncertainty in the beam area at the sample. Interpolated values for the beam diameter were used in this work, as described in Section III.1. Errors in beam diameter measurement affect the incident pulse intensity by Equation 16, with the result that the data in Figure 21 may be scaled horizontally along the intensity axis. In addition, the fitting simulations used a Gaussian spatial profile, but the FEL beam has some

spatial irregularities. It is found that a 10% variation in the beam diameter can result in a 50% variation in the derived coefficients.

The second major caveat is due to uncertainty in the free carrier absorption cross-sections. Free carriers generated by multiphoton absorption can be excited further by single-photon absorption, either due to subsequent photons in the same micropulse or in latter micropulses. Ignoring free carrier absorption effects can cause derived multiphoton absorption coefficients to be off by orders of magnitude. [40, 54] While in other works the 2PA/3PA coefficients and free carrier cross-sections are fitted simultaneously, [24] in this work an approach employing FTIR of doped samples was used to measure these values directly, as described in Section III.1. Still, these cross-sections may be influenced by a variety of factors, particularly the energy state of the photo-excited carrier undergoing absorption, though as discussed earlier the unique pulse structure of the FEL should allow sufficient time for carrier relaxation, more than other laser sources. Nevertheless, it is noted that a 10% variation in the free carrier absorption cross-sections σ_n and σ_p can result in a 15% variation in the derived multiphoton absorption coefficients.

III.3.3 Ratios of Absorption Coefficients

Although the caveats listed above, which are common to nonlinear absorption experiments, cast some uncertainty on the reported absolute absorption coefficients, the ratios of these coefficients across the direct-to-indirect transitions for 2PA and 3PA are found to be invariant to systematic changes of at least 20% in both beam diameter and free carrier absorption coefficients. Essentially all theoretical treatments of nonlinear absorption consider a multiplicative factor $f(x) \geq 0$ that reflects the multiple ways that two or three photons can add to give multiphoton absorption. For 2PA, $x = 2\hbar\omega/E_g$, and for 3PA, $x = 3\hbar\omega/E_g$. (Here, E_g may refer to the direct (0.8 eV) or indirect (0.67 eV) gap, depending on the absorption regime.) Ideally, comparisons

of ratios across the direct/indirect transitions should be made using the same value of x . Here, for the 2PA ratio, 2.8 μm ($x = 1.11$) and 3.2 μm ($x = 1.17$) are used, and for 3PA, 4.4 μm ($x = 1.06$) and 5.2 μm ($x = 1.07$) are used. For the transition from 2.8 μm to 3.2 μm , the ratio in β is 175. In a previous work this ratio was estimated as 2,000. [48] For the transition from 4.4 μm to 5.2 μm , the ratio in γ is 5. These ratios should prove valuable in the continued development of the theoretical models for indirect 2PA and 3PA. A comparison of two separate experiments in silicon [74,75] shows a ratio of 17 across the 2PA direct/indirect transition. The advantage in this work lies in the use of a single laser source and experimental setup for all wavelengths.

The quantity $\beta/(\gamma I)$ provides a measure of the relative importance of 2PA to 3PA at a given intensity I . Assuming that the direct 3PA remains on the order of $0.05 \text{ cm}^3/\text{GW}^2$ in the wavelength regimes where 2PA is allowed, at 2.8 μm 3PA will dominate at intensities greater than $300 \text{ GW}/\text{cm}^2$. For 3.2 μm and 3.6 μm , 3PA will dominate above $2.5 \text{ GW}/\text{cm}^2$.

The theoretical work of Garcia and Kalyanaraman on indirect 2PA in silicon [76] predicts the relative indirect absorption coefficients at different wavelengths. Although their work dealt with silicon, the general shape of the curve as a function of x should hold for other materials. At 3.2 μm and 3.6 μm , the Garcia theory predicts that the allowed-allowed transition dominates and calculates a ratio of 10 between the coefficients at these wavelengths. In this work, ratio is found to be 2.

III.4 Potential Expansion Studies

There are multiple ways in which the study reported in this chapter could be extended. For instance, more detailed knowledge about the energy states occupied by the photoexcited electrons and holes would enable a more sophisticated modeling approach, which could account for carrier dynamic effects that have not been considered here. A two-color pump-probe transmission study, which would be able to determine

free-carrier absorption cross-sections directly, and to distinguish electron cross sections between the L and Γ valleys, would be particularly useful in this regard. Such a study could also measure the predicted onset of hole absorption due to electron excitation from the split-off band to the valence band. [49]

In addition, a new method for measuring multiphoton absorption coefficients is suggested by the technique known as coherent acoustic phonon interferometry, which has already been used to measure linear absorption coefficients. Such a technique would be particularly well suited to measure the nonlinear absorption properties of multilayered heterostructures, for which transmission measurements would only provide averaged information on the full specimen. The CAP technique is described in detail in Section V.2.1.

PART TWO:

**COHERENT ACOUSTIC PHONON INTERFEROMETRY OF ION
IMPLANTATION DEFECTS IN DIAMOND CRYSTALS**

CHAPTER IV

INTRODUCTION

This chapter introduces and motivates the study of ion-bombarded diamond using coherent phonon effects. Following that is a statement of work describing the planned experiments, and a discussion of the scope and limitations of this project.

IV.1 Research Problem

Diamond is an indirect wide band-gap semiconductor that has long been known for its superlative mechanical, electronic, thermal, and tribological properties. [77] Most recently, diamond's optical properties, specifically its many optically active defect complexes, have generated considerable interest for photonic and quantum computing applications. Of these complexes, the NV^- color center is by far the most studied, [78–80] (see Figure 26) but there are several complexes of interest. [81] Centers such as the NV^- provide bright, stable, room-temperature sources for single photons, [82] exhibit spin coherence lifetimes on the order of a millisecond, [83] and have electronic spin states that can be controlled and read optically. [84] These qualities make optical centers in diamond ideal candidates for quantum computing devices, and diamond-based qubits and coupled multi-qubits have been demonstrated. [85,86]

NV^- centers occur in natural diamonds, and they can be introduced into device-quality crystals in a controlled way by means of ion implantation followed by annealing above 700 °C. [88] Targeted implantation of single NV^- defects by means of a focused nitrogen beam has also been demonstrated. [89] NV^- centers can also be incorporated during chemical vapor deposition (CVD) crystal growth by incorporating appropriate nitrogen precursors into the growth chamber. This method exhibits decreased spatial control, but allows for preferential orientation of the NV^- axis. [90]

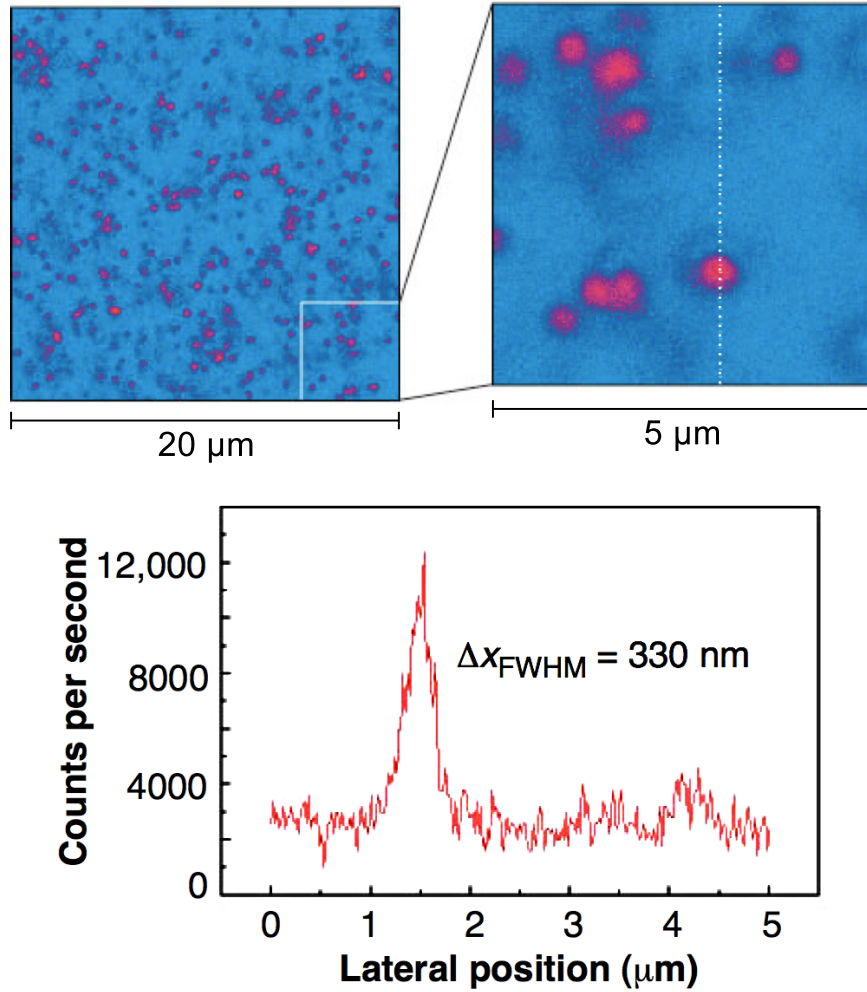


Figure 26: Scanning confocal fluorescence micrographs of single fluorescent NV^- centers in type Ib diamond, from [87]. The cross-sectional scan indicated by the dotted line in the 5 μm image is shown at the bottom.

Recently, an ion implantation and lift-out technique in diamond has been reported for the fabrication of single-crystal nanoscale photonic devices. [91] In this technique, light ions such as helium are implanted at energies from 0.5 to 2.0 eV into diamond single crystals to create a sacrificial buried layer of implantation damage (see Figure 27). High-temperature annealing repairs the implantation damage up to a certain threshold, thereby sharpening the interface between the damaged and undamaged layers of the specimen. At this point, focused ion beam milling may be used to pattern the desired features. Finally, the damaged layer is removed using a chemical etch, leaving a free-standing structure. Thin monolithic diamond structures, such as those shown in Figure 28, can be used to collect and guide the light to and from qubits in quantum information devices, or as interconnects in photonic computers.

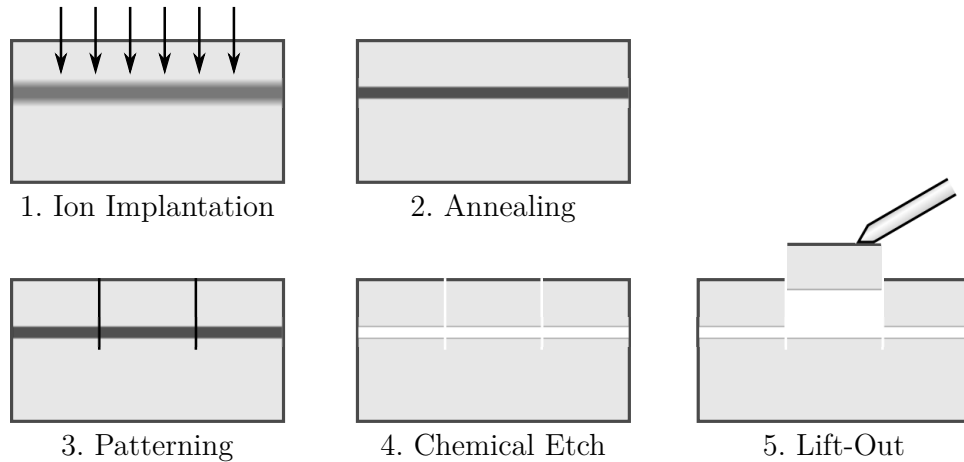


Figure 27: Implantation and lift-out technique for photonic device fabrication in diamond crystals.

To summarize, in the burgeoning fields of quantum information processing and photonics, diamond is a prime candidate for a host material. In addition, these fields are likely to employ ion implantation as a principal technique for scalable device fabrication. However, ion implantation introduces defects into the lattice that modify

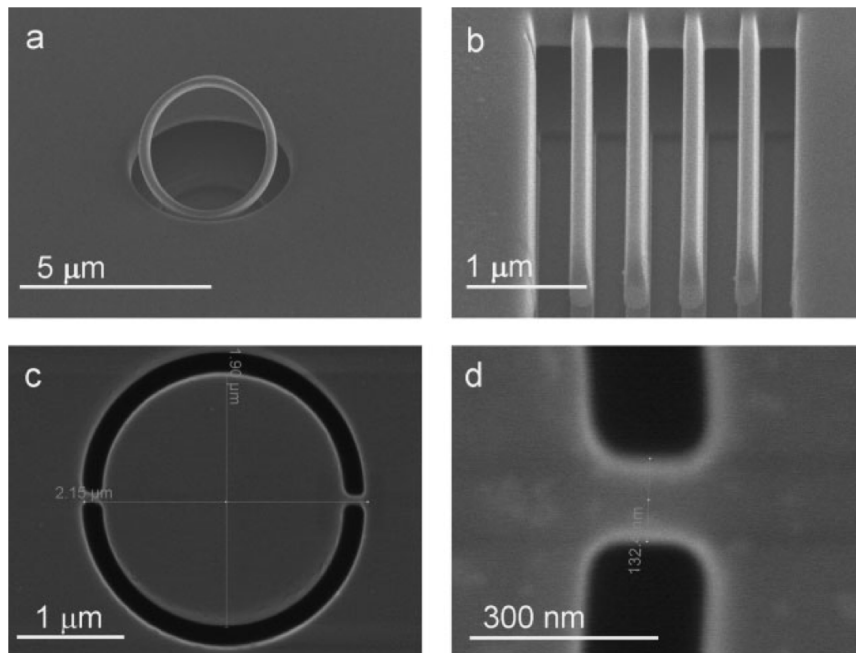


Figure 28: Single-crystal diamond nanostructures generated using the ion implantation and lift-out technique, taken from [91]. a) Micrometer-scale ring, a prototype for a whispering gallery mode resonator, fabricated in a 330 nm layer of single-crystal diamond. b) Nano-cantilevers 110 nm wide, $\sim 3 \mu\text{m}$ long, in a 330 nm layer. c) Concept cavity with 1.9 μm inner diameter and 2.2 μm outer diameter. d) High-magnification view of the diamond bridge from c), 130 nm wide.

local electronic wave functions, and thereby modulate the opto-electronic properties of the material. In addition, ion implantation in diamond can transform the bonding characteristics of the lattice atoms, introducing significant strain in implanted crystals and causing surface swelling or even the total amorphization of the lattice. [92–94]

Clearly, reliable fabrication of single-photon emitting centers and photonic devices in diamond using ion implantation techniques will require a detailed understanding of the associated defects created within the lattice during the implantation process, and how those defects modify the optical properties of diamond. Despite decades of work [95,96] on ion implantation in diamond and the optical properties of diamond defects, many questions remain concerning the specific relationships between the structural modifications of the diamond lattice and the resulting modulation of local optical properties.

IV.2 Statement of Work

In this study, coherent acoustic phonon (CAP) interferometry is applied to ion-implanted diamond crystals to determine the nature of the implantation-induced modulation of diamond’s optical characteristics. CAP interferometry is a depth-resolved, non-destructive ultrafast optical pump-probe technique employing the reflectivity of phonon waves, and is sensitive to local modulations in the optical properties of materials with a spatial resolution of ~ 10 nm. Recent experiments on implanted GaAs crystals (see Section V.2.2) using CAP interferometry have shown that the CAP technique is sensitive to damage-induced modulations of optical structure over several orders of magnitude in fluence, and in particular at very low fluences. This work will show that CAP interferometry is also sensitive to implantation damage in diamond crystals, and that ion implantation can significantly modify the optical properties of diamond, specifically the complex refractive index and its first derivative with strain. The CAP results are compared to cross-sectional transmission electron

microscopy (TEM), and numerical simulations of the CAP experiments are applied to derive quantitative relationships between implantation-induced lattice damage and the resulting optical modification.

IV.3 Scope and Limitations

There are a number of interesting questions and experiments suggested by this research topic. For instance, what sorts of defect species are created in diamond by ion bombardment? Can certain modulations in the optical characteristics of the diamond lattice be associated with specific defect types? Can tuning the wavelength of the optical probe in a CAP experiment isolate the NV^- center or other defect species? Ion-bombarded diamond lattices are well-known to heal under annealing conditions, so long as the damage is below a particular threshold. [97–99] Could the CAP technique measure this self-healing process, and the accompanying sharpening of the interface between specimen regions above and below the critical damage threshold?

While these questions are clearly significant and may be explored in future experiments, the present study will be limited to the overall effect of implantation damage on the optical characteristics of diamond lattices in the mid-gap energy regime. As such, this study will assist in tailoring implantation conditions toward the fabrication of diamond-based photonic devices with desirable properties for a given application.

CHAPTER V

LITERATURE REVIEW

This chapter first summarizes the current state of research in the area of ion implantation in diamond and its effect on diamond's optical characteristics. Following that is an introduction to coherent acoustic phonon interferometry as an optical characterization technique, and a summary of its prior applications to ion-implanted crystals and to diamond crystals.

V.1 Ion Implantation in Diamond

The first investigation of the effect of ion irradiation on the properties of diamond was performed in 1909 by Sir William Crookes, [100] who observed discoloration in natural diamonds after exposing them to radium. The effects he observed were later attributed to α particle bombardment. [101] Since then, ion bombardment of diamond crystals has been a subject of continual interest. Early works (up through the 1960's) focused on the generation of diamonds with specific spectral characteristics, or on the use of diamonds as scintillation detectors. Strictly speaking, these works employed neutron and electron sources, rather than energetic ions. However, these investigations laid the groundwork for understanding the role of natural and artificial structural defects as well as annealing on diamond's optical properties. Billington and Crawford [102] provide an excellent review of this era, as does Champion. [103]

Systematic studies of ion implantation in diamond began in the 1960's, [104–106] and were primarily concerned with the electrical conductivity of the irradiated specimens. One notable exception is the work by R. L. Hines, [106] who measured the optical reflectivity and transmission of implanted diamonds, and discovered that

both the real and imaginary indices increase with implantation fluence and that they could be restored upon annealing.

Interest intensified from the 1970's through the 1990's, and primary areas of focus included determining the exact nature of the induced electrical conductivity in implanted layers, [107–112] using ion bombardment to artificially produce semiconducting diamonds, [113–118] determining the critical implantation fluence above which damaged layers could no longer be restored to pristine diamond by annealing, [99, 119–123] and identifying specific point defect species resulting from implantation and their behavior under annealing conditions. [124–135] The study of the critical damage level for total amorphization of the diamond lattice continues to this day, [94, 97, 136, 137] as does the pursuit of semiconducting diamond devices, though in the latter case, the approach has shifted to dopant incorporation during diamond film growth. [138]

There are several reviews of the above efforts in the literature, [139–143], the most recent being a book chapter written in 1998 by Kalish and Praver. [143] A full book by Dresselhaus and Kalish [139] and a review article by Praver and Kalish [142] are also excellent starting points. The scientific findings relevant to this work may be summarized as follows: room-temperature implantation in diamond results in the formation of defect clusters, which below a critical vacancy concentration of about 10^{22} cm^{-3} may be removed by annealing. Above a critical damage level, the material retains its sp^3 bonding character but the lattice collapses into amorphous carbon, and annealing or further implantation results in graphitization, that is, the conversion of sp^3 bonds to sp^2 .

V.1.1 Optical Properties of Ion-implanted Diamond

Beginning near the turn of the century, with the rapid growth of quantum information science [144] and the identification of the NV^- center in diamond as a possible stable

photon source [82,87] (see Section IV.1), attention was shifted to the optical properties of ion implanted diamonds. [137,145–153]

In 1997, Bhatia et al. measured the Raman, FTIR, and visual-ultraviolet spectra of a diamond specimen irradiated with progressively larger fluences of C^+ ions. [145] In the visual spectrum, they were able to extract information on the real refractive index and the optical absorption. Their results are shown in Figure 29. Although they did not observe any clear correlation between the real refractive index and the ion fluence, there was a clear correlation between ion fluence F and optical absorption α , with a phenomenological fit at 918 nm of

$$\alpha = (1.3 \times 10^{-4})F^{1/2}. \quad (19)$$

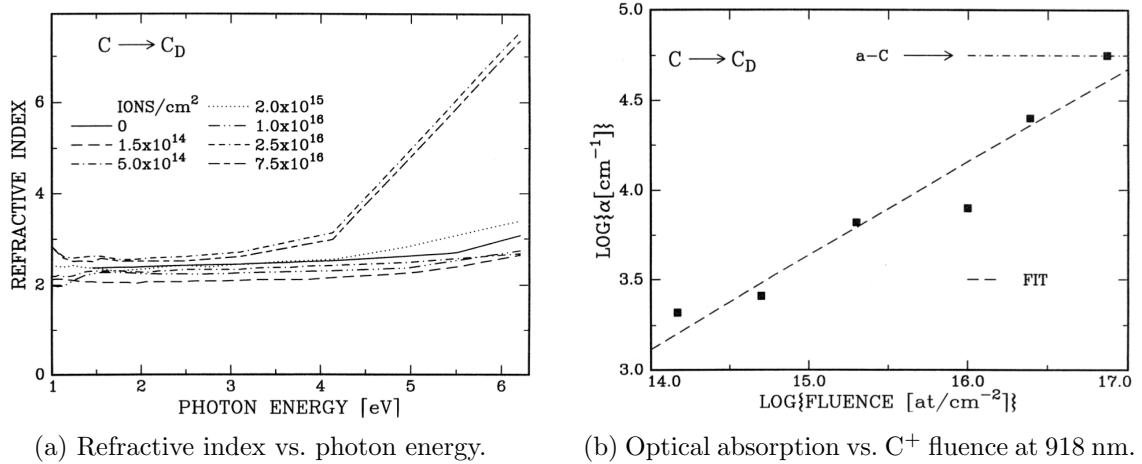


Figure 29: Optical properties of C^+ -implanted diamond as measured by Bhatia et al. [145].

Gippius, Khomich, et al. have studied the optical characteristics of heavily-damaged layers in He^+ -implanted diamonds that have been annealed to induce graphitization. Their first report [137] in 2003 relied primarily on visual inspection, but in a second

report [146] they employed spectroscopic ellipsometry to extract the real and imaginary indices of the graphitized layers, as depicted in Figure 30. These results provide valuable information for optical device fabrication using high-dose implantation and annealing to produce graphitic layers, but they leave open the question of the optical characteristics of partially damaged and fully-amorphized diamond lattices prior to annealing.

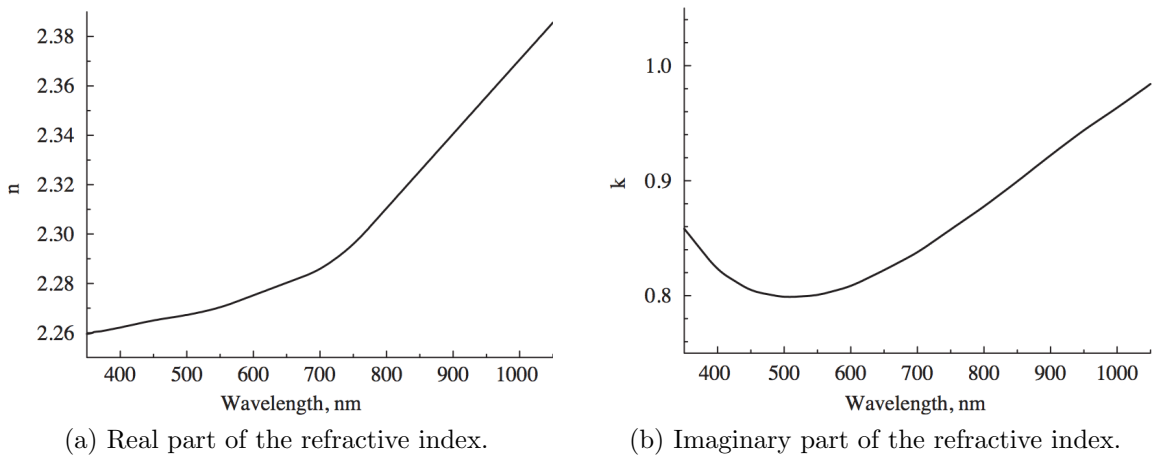


Figure 30: Real and imaginary refractive indices vs. wavelength for graphitized implanted diamond layers as measured by Khomich et al. [146]

To date two groups have addressed the problem of implantation-induced optical modification prior to annealing. The first group, Draganski et al. (P.I. Steven Prawer), presented preliminary results using spectroscopic ellipsometry in 2008, [154] and a more full treatment in 2012. [152] They implanted 30 keV Ga^+ ions at a range of fluences, and their primary results after ellipsometric analysis are shown in Figure 31. For the real part of the refractive index, they observed a decrease at low fluences and an increase at higher fluences. They suggest that this behavior is unique to heavy-ion implantations, as previous studies (see the work of the Olivero group, below) using light ions found only monotonic increases in the refractive index with implantation

fluence. For the imaginary index, they observe an increase at all fluences, but again the behavior is non-monotonic, as confirmed by conductivity measurements.

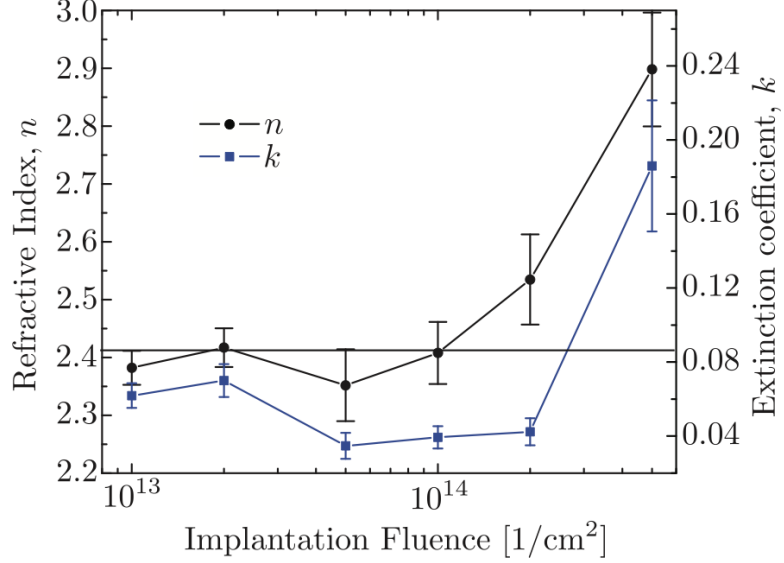


Figure 31: Variation in the real and imaginary parts of the refractive index of Ga⁺-implanted diamond at multiple implantation fluences, from [152]

The Olivero group is the second to address this problem, beginning with a report in 2010 [148] wherein they use an interference microscopy technique to measure the refractive index variation at 632.8 nm (near the wavelength of NV⁻ center emission) for 2 and 3 MeV proton-implanted diamonds over a range of fluences. This technique yields an areal map of the optical path difference for full-thickness traversal of different regions of the specimen, as depicted in Figure 32(a). Figures 32(b)–(c) show the measured optical path difference as a function of ion fluence, after subtraction of the specimen swelling contribution. From this data, they extract the following phenomenological relation for the real refractive index variation as a function of vacancy concentration C_V :

$$n = n_0 + [(4.3 \pm 0.3) \times 10^{-23}] \times C_V. \quad (20)$$

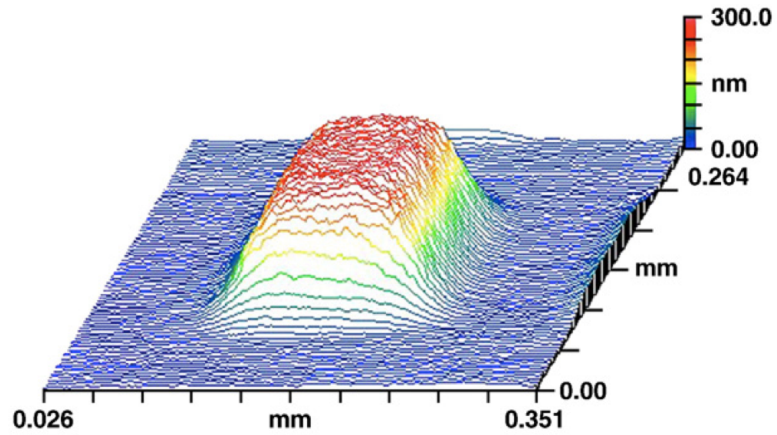
This linear behavior is relevant to specimens irradiated at lower fluences, where the lattice has not amorphized and there is no saturation behavior.

In 2011, the same group reported attempts to expand the spectral range of the above measurement using transmission spectroscopy, [149] but were unable to derive a single conclusive spectrum. However, as reported in 2012 (Battiato et al. [151]), using a combination of spectroscopic ellipsometry and transmittance measurements they were able to extract successfully the spectral behavior of the complex refractive index (Figures 33(a)–(b)) for diamonds that had been irradiated with 180 keV B⁺ ions, and to determine phenomenologically that, for the real refractive index,

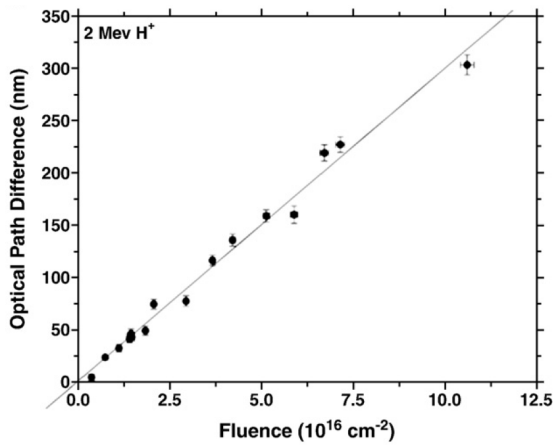
$$n = n_0 + c[1 - \exp(-C_V/b)], \quad (21)$$

with b and c as fitting parameters (at 638 nm, $b = 1.5 \times 10^{21} \text{ cm}^{-3}$ and $c = 0.1$, as depicted in Figure 33(c)). The exponential behavior of this curve accounts for the saturation effect in the real index change at high doses. For the imaginary component of the refractive index, the investigators did not derive an expression as a function of vacancy concentration, but instead derived an expression for the absorption of the entire specimen thickness as a function of ion fluence.

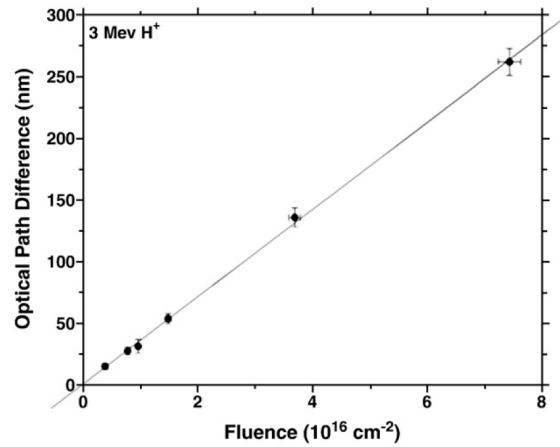
The full evaluation of the complex refractive index of proton-irradiated diamond as a function of vacancy concentration came later in 2012 (Lagomarsino et al. [153]). In this work, the group expanded on their results from [148] by measuring differences in absorption length between irradiated and unirradiated diamond regions, and by applying a multi-layer propagation model which accounted for refraction and absorption using the full complex index. Their results are shown in Figure 34. Since all of the implantation fluences are below the amorphization limit, they again find good agreement with the experimental data using a linear model for the dependence of the



(a) Optical path difference map showing a $125 \times 125 \mu\text{m}^2$ region implanted with 2 MeV protons at a fluence of $7.63 \times 10^{16} \text{ cm}^{-2}$.

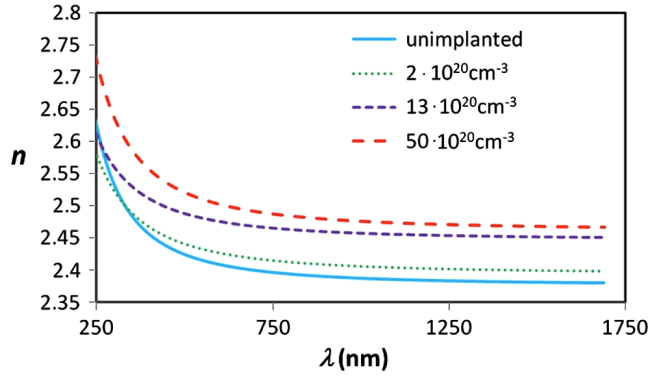


(b) Optical path difference vs. fluence for 2 MeV proton implantations.

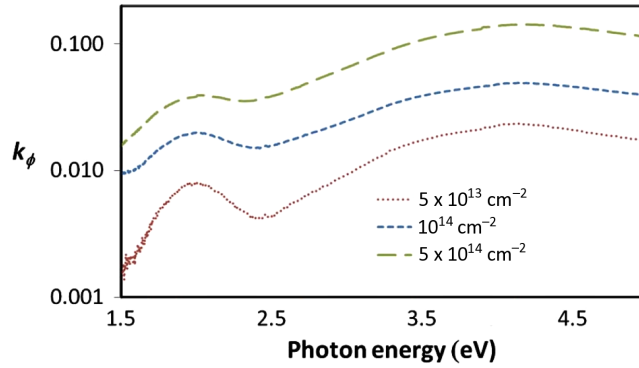


(c) Optical path difference vs. fluence for 3 MeV proton implantations.

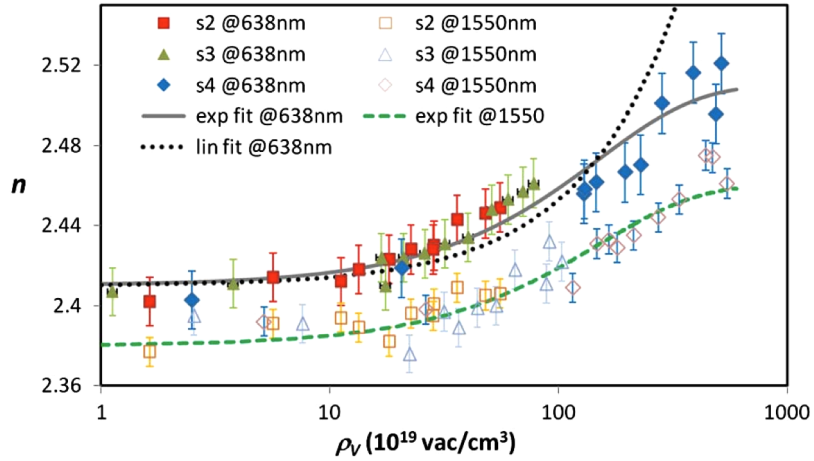
Figure 32: Optical path difference data for proton-implanted diamonds as measured by Olivero et al., from [148].



(a) Real refractive index vs. wavelength at various vacancy concentrations.

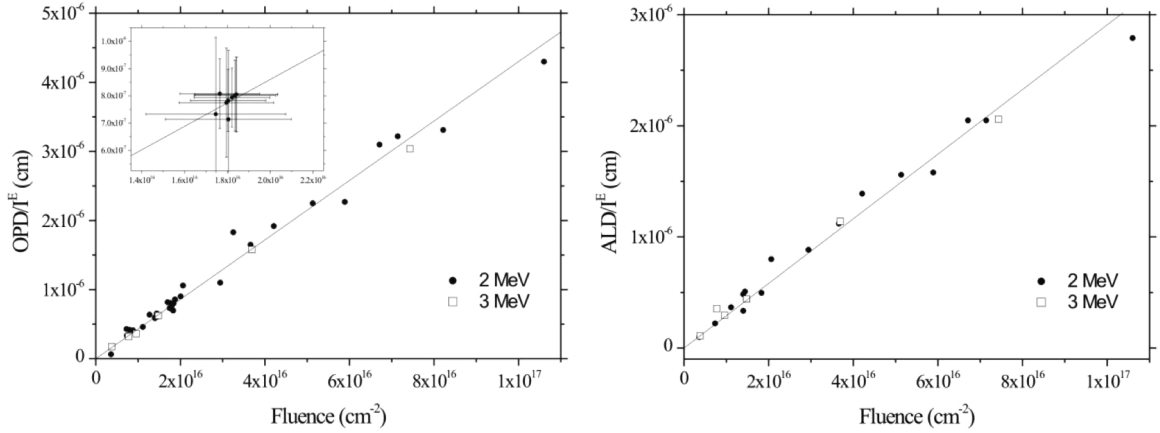


(b) Average imaginary refractive index vs. photon energy at various implantation fluences.



(c) Real refractive index vs. vacancy concentration at 638 and 1550 nm, along with linear and exponential fits.

Figure 33: Derived refractive index information for proton-irradiated diamonds as measured by Battiato et al., from [151].



(a) Optical path difference between irradiated and unirradiated regions vs. implantation fluence, used to determine the behavior of the real refractive index.

(b) Absorption length difference between irradiated and unirradiated regions vs. implantation fluence, used to determine the behavior of the imaginary refractive index.

Figure 34: Optical measurements of proton-implanted diamond specimens by Lagomarsino et al. [153] The lines show fits based on the linear model from Equation 22.

complex index \tilde{n} at 632.8 nm on local vacancy concentration C_V :

$$\tilde{n} = 2.41 + [(4.34 + 2.86i) \times 10^{-23}] \times C_V. \quad (22)$$

The above findings will be compared directly with those of the current work in Chapters VI and VII.

V.2 Coherent Acoustic Phonon Interferometry

V.2.1 The CAP Technique

Coherent acoustic phonon (CAP) interferometry, also known as picosecond ultra-sonics, is a well-developed all-optical technique for non-destructive and non-invasive depth-resolved materials characterization. The CAP method is a subset of the more general category of ultrafast optical pump-and-probe experiments, wherein a strong electromagnetic pump pulse perturbs a system in some way that can be measured by a weak probe pulse a brief time later. This approach to materials characterization has

blossomed in the last few decades due to significant advances in laser technology that have made available coherent optical sources with ultrafast (~ 100 fs) pulse lengths, high powers, and high repetition rates.

Strain Wave Generation

The defining characteristic of CAP pump-probe experiments is the presence of a thin transducing layer, either at the specimen surface or embedded within it. This layer usually consists of metal, but could be any material which strongly absorbs at the pump frequency. The incidence of the optical pump pulse on this layer results in the generation of a coherent acoustic phonon pulse, which radiates out from the location of incidence and traverses the specimen at the longitudinal speed of sound. As described below, the subsequent optical probe will be partially reflected from this traveling acoustic pulse, yielding the depth sensitivity of the technique. Figure 35(a) depicts the pump-induced strain wave generation process.

The generation and detection of laser-induced picosecond acoustic pulses was first reported in 1984 [155] and elaborated on in 1986 [156] by a group of researchers at Brown University. They employed a model based on surface heating to describe the acoustic pulse generation. Briefly, the absorbed optical pump heats up the transducing layer, introducing thermal stress that is relaxed by means of surface swelling and the launching of the acoustic strain pulse. They go on to show that, to first order, the propagating strain pulse has the form of an exponentially decaying sign function, as depicted in Figure 36. This propagating strain pulse, also referred to as the CAP wave, has been observed to traverse millimeter-thick specimens with little-to-no decoherence. [157]

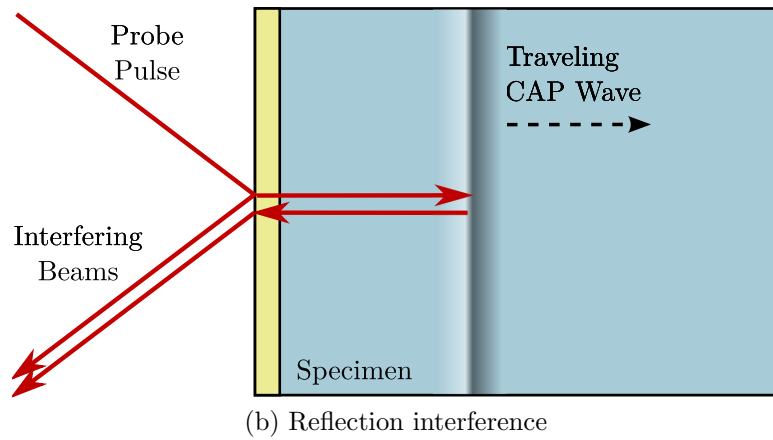
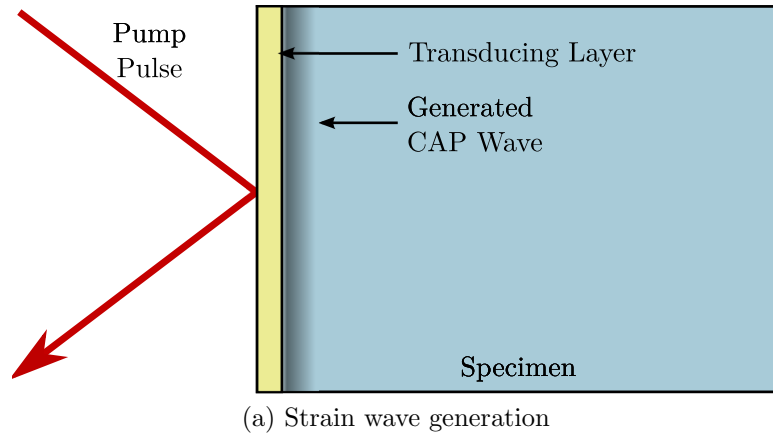


Figure 35: Schematic views of (a) the pump-induced strain wave generation and (b) the strain-induced interference effect in the reflected probe beam in a typical reflection geometry CAP experiment.

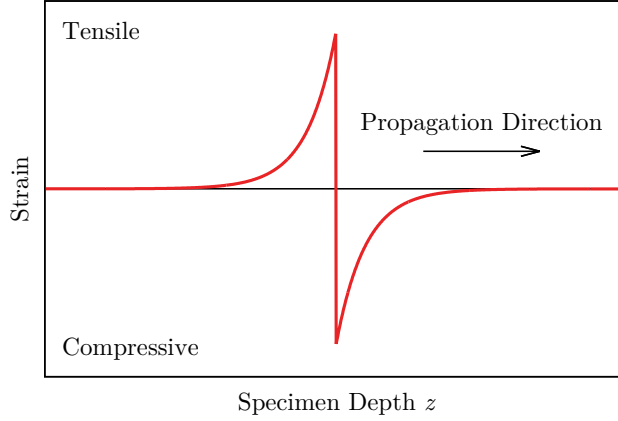


Figure 36: Coherent acoustic phonon strain pulse shape.

Reflection Interference

The propagating strain pulse represents a distortion of the ordinary lattice spacing of the host material, and modulates the local material properties. For CAP experiments, the property of interest is the complex index of refraction, $\tilde{n} = n + i\kappa$, which at a given point in time is modulated to first order according to:

$$\tilde{n}(z, t) = \tilde{n}_0 + \frac{d\tilde{n}}{d\eta} \eta(z, t), \quad (23)$$

where \tilde{n}_0 is the index of the unperturbed lattice, η is the strain from the propagating acoustic pulse, and $d\tilde{n}/d\eta$ is the photoelastic coefficient of the host material. The strain-induced modulation of the refractive index produces an optical interface in the host material that is particularly strong at the sharp transition from compressive to tensile strain (see Figure 36). In this way, the CAP wave acts as a “moving mirror” within the specimen.

Upon incidence with the specimen, the electromagnetic probe reflects from both the surface and from the propagating CAP wave, resulting in self-interference (Figure 35(b)). The interference can be either constructive or destructive, depending on the distance between the CAP wave and the specimen surface. This distance may be

selected by varying the time delay between the pump and probe pulses, thus allowing the CAP wave more or less time to propagate into the specimen before the incidence of the probe. A systematic variation of the pump-probe time delay results in an oscillation pattern in the reflectivity signal, as depicted in Figure 37.

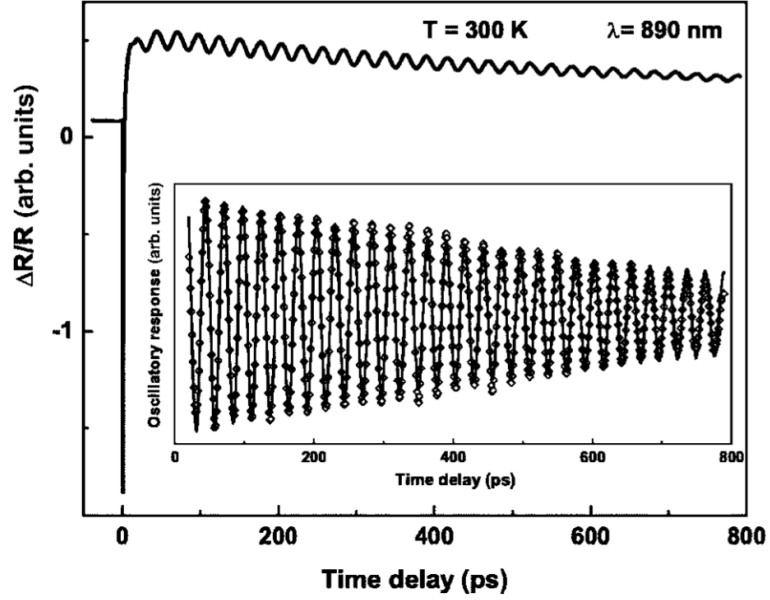


Figure 37: CAP-induced interference oscillations in the pump-probe reflectivity signal of a GaAs specimen with a 20 nm transducing layer of GaSb on the surface, from [158]. The inset shows the same data after subtraction of the thermal pump-probe response, isolating the phonon-induced oscillations.

Materials Characterization

Analyzing the behavior of the CAP oscillations reveals information about the material under study, as depicted in Figure 38. For instance, the period of the oscillations, T , is determined by the real refractive index and the speed of sound according to:

$$T = \frac{\lambda}{2nv_s}, \quad (24)$$

where λ is the wavelength of the optical probe. The decay of the oscillations is associated with the imaginary part of the refractive index, κ , according to:

$$\text{Decay} \propto \exp(-\alpha v_s t) = \exp \left[- \left(\frac{4\pi\kappa}{\lambda} \right) v_s t \right]. \quad (25)$$

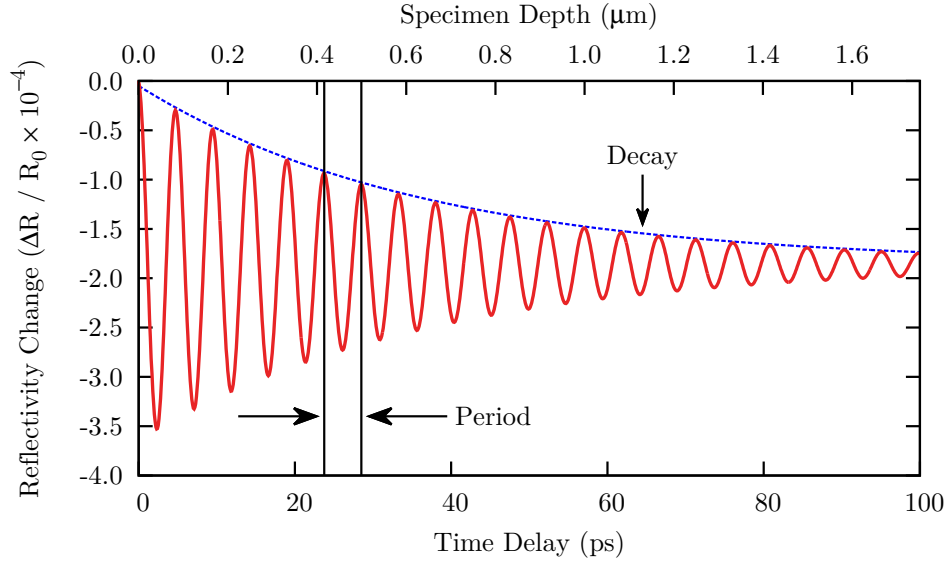


Figure 38: Simulated CAP oscillations for a material with index $\tilde{n} = 2.4 + 0.05i$ and speed of sound $v_s = 17.52$ nm/ps.

Since the CAP wave propagates at the longitudinal speed of sound v_s , the pump-probe time delay t may be correlated directly with specimen depth, z , according to:

$$z = v_s t. \quad (26)$$

This fact is the key to the depth sensitivity of the CAP technique. It should be noted that in these sorts of experiments, the depths of interest are usually much smaller than the diameter of the laser spot; thus, a near-field regime is assumed, and the CAP wave is treated as planar. In the more general far-field case, the CAP wave

radiates spherically from the point of incidence, and information about the depth-dependent nature of a specimen requires more careful evaluation. Figure 39 shows a near-field CAP reflectivity measurement on a multilayered system consisting of 1 μm of molecular-beam epitaxial $\text{Ga}_{0.95}\text{Mn}_{0.05}\text{As}$ above a 300 nm layer of low-temperature grown GaAs above a GaAs substrate. [159] The multi-layered structure of the material is apparent in the amplitude of the oscillations, as shown in the inset.

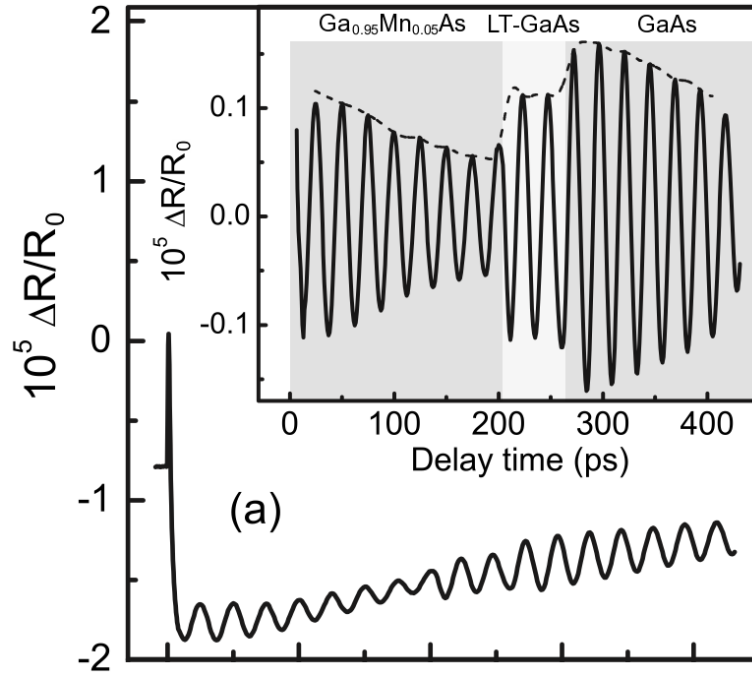


Figure 39: CAP reflectivity of a $\text{Ga}_{0.95}\text{Mn}_{0.05}\text{As}/\text{LT-GaAs}/\text{GaAs}$ heterostructure grown using molecular beam epitaxy, from [159]. The layered structure of the specimen is most clearly visible in the inset, which shows the isolated CAP oscillations.

Changes in the amplitude of CAP oscillations that do not follow exponential decay behavior can be attributed to variations in the photoelastic coefficient, $d\tilde{n}/d\eta$. In the case of Figure 39, $d\tilde{n}/d\eta$ varies with the different material layers. Generally, the greater the magnitude of $d\tilde{n}/d\eta$, the stronger the reflectivity of the CAP wave and the larger the CAP oscillations. Like the index \tilde{n} , $d\tilde{n}/d\eta$ is a function of wavelength,

and has been found in semiconductors to be particularly strong at photon energies near the band edge. [158] In addition, this quantity is associated with the p_{12} Pockels coefficient of the photoelastic tensor, [160] according to:

$$\frac{d\tilde{n}}{d\eta} = -\frac{\tilde{n}^3}{2}p_{12}. \quad (27)$$

V.2.2 CAP in Ion-implanted Materials

Only a few experimental studies of the CAP response of ion-implanted crystals have been reported. In 2009, Steigerwald et al [161] reported CAP experiments on GaAs crystals implanted with 325 keV He⁺ ions. As shown in Figure 40, they observed a decrease in the CAP oscillation amplitude at specimen depths corresponding to the peak implantation damage. The depth of the amplitude loss was in excellent agreement with Monte Carlo simulation codes (specifically, the TRIM code [162]), and by performing implantations at multiple He⁺ fluences, the investigators were able to correlate the oscillation amplitude loss directly with local vacancy concentrations, as depicted in Figure 41.

The oscillation amplitude loss depicted in Figure 40 was attributed to a band tailing effect brought on by the implantation damage, resulting in a decrease in the photoelastic coefficient $d\tilde{n}/d\eta$. In 2012, the same group of researchers reported further experimental work, this time implanting GaAs crystals with 400 keV Ne⁺⁺ ions. [163] They were able to determine the optical damage cross-section around the Ne⁺⁺ tracks, and found that the extent of the optical modification to the crystal was about five times that of the structural modification. In addition, they found that the CAP response was highly sensitive to the wavelength of the optical probe in the vicinity of the band edge, further validating the band tailing interpretation. They also verified the earlier quantitative measurement of vacancy concentration profiles using CAP methods by performing ion channeling experiments on the implanted specimens.

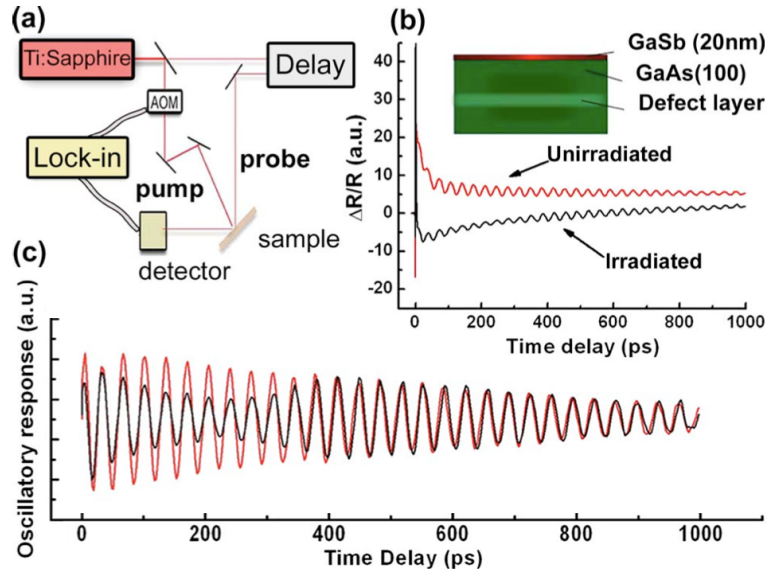


Figure 40: CAP response of a He^+ -implanted GaAs specimen, from [161]. The implantation fluence was $3.5 \times 10^{13} \text{ cm}^{-2}$. (a) Experimental setup for measuring CAP reflectivity. (b) Reflectivity response for implanted (black) and unimplanted (red) GaAs specimens. The inset shows the specimen geometry. (c) Isolated CAP oscillations from the reflectivity data. The loss of oscillation amplitude in the implanted specimen (black) is evident at 200 ps.

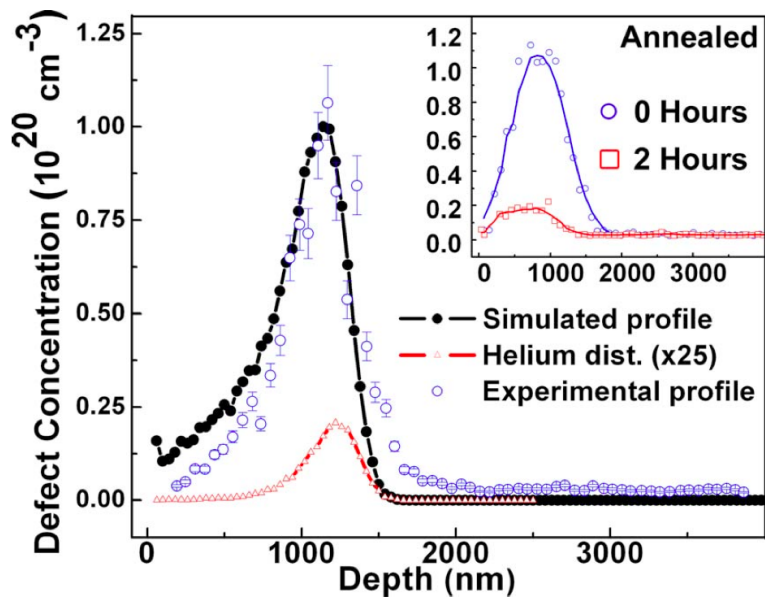


Figure 41: Comparison between experimentally-derived vacancy concentration profile from CAP reflectivity data (blue) and TRIM code simulation (black) for He-implanted GaAs specimens, from [161]. The inset shows the experimental profile before and after annealing, with evident healing of the implantation damage.

Finally, another group (Rossignol et al.) reported in 2012 on the behavior of ion-implanted TiO_2 thin films grown on SrTiO_3 substrates under CAP interferometry measurements. [164] They found that the implantation defects accumulated in the interfacial SrTiO_3 region, and that the speed of sound in that region was reduced three-fold at the highest implantation fluences.

V.2.3 CAP in Diamond

There are two previous reports of CAP measurements in diamond materials, one of which was applied to ion-implanted diamond. The first report was published in 2004 by Rossignol et al. [165] They studied polycrystalline diamond films grown on substrates of Ti alloy using chemical vapor deposition, and were able to evaluate the relative quality of different films by determining their elastic constants (C_{33}) from the CAP data. In this case, the Ti alloy substrate itself acted as the transducing layer, and the CAP wave traveled from the substrate towards the surface. Thus, they were also able to evaluate the surface roughness of the films by observing the strength of the reflection of the CAP wave at the surface of each specimen.

CAP in Ion-implanted Diamond

In the second work, [166] published in 2011, Klokov et al studied the CAP response of diamond specimens that had been implanted with 350 keV C^+ ions and annealed to sharpen the internal amorphous-crystalline interface. They used the internal damage layer for the transducing effect, and were able to extract the thermoelastic response of those layers. However, the reflectivity response data was extremely noisy, and the convergence between their experimental results and the calculations was poor.

V.2.4 Summary

All of the aforementioned results show that CAP interferometry is a valuable tool that has yet to be fully exploited for the study of ion implanted materials, and in particular for ion-implanted diamond. This study seeks to further the knowledge of implantation-induced optical modifications in diamond and to broaden the capabilities of the CAP technique.

CHAPTER VI

EXPERIMENT

This chapter describes in detail the experimental techniques employed in these studies. The results of the coherent acoustic phonon reflectivity measurements in implanted diamonds are presented, along with the comparison to TEM. Finally, the observed features in the reflectivity data are attributed to specific modulations in the optical characteristics of the diamond lattice. For details concerning the numerical simulations of the CAP experiments, see Chapter VII (Phenomenological Model).

VI.1 Methodology

VI.1.1 Implantation

Single-crystal type IIa CVD diamond specimens were purchased from the Element Six Corporation. Specimens had (100) crystal orientation on all faces, dimensions $3 \times 3 \times 0.3$ mm, and were polished on both sides. A High-Voltage Engineering AN-2000 electrostatic Van de Graaff accelerator was used to implant the specimens with 1 MeV He^+ ions at currents of approximately 200 nA, with fluences ranging from 10^{14} to 3×10^{17} cm^{-2} . In some cases more than one crystal was implanted at the same fluence. Implantations were performed in vacuum at temperatures below 0 °C. Specimen heating during implantation is assumed to be negligible due to the high thermal conductivity of diamond and good thermal coupling with the large aluminum block on which the crystals were mounted.

To model the lattice damage resulting from ion implantation, Monte Carlo simulations were performed using the Transport of Ions in Matter (TRIM) code. [162] Model parameters were $3.515 \text{ g}\cdot\text{cm}^{-3}$ for the density of diamond and 52 eV for the displacement energy. [167] The TRIM results were verified by cross-sectional TEM

using a Philips CM200 microscope at Oak Ridge National Laboratory. TEM sample preparation was performed using a TESCAN dual-beam FIB at the MTSU MIMIC facility.

VI.1.2 Coherent Acoustic Phonon Interferometry

To form the transducing layer, implanted crystals were coated with ~ 10 nm of aluminum using an Angstrom Åmod resistive evaporation chamber. Pump-probe reflectivity measurements were taken using a Coherent Mira 900 Ti:Sapphire laser producing 150 fs pulses at 76 MHz. The experimental setup is shown in Figure 42. The pump beam was tuned to 800 nm with an average power of 150 mW, and the probe beam was frequency-doubled to 400 nm (near the middle of the diamond band gap) with a typical average power of 2.1 mW. Both beams were focused onto the specimen at the same location with a spot diameter of 100 μm for the pump and 50 μm for the probe. To reduce interference in the reflectivity signal, the pump beam was modulated at 50 kHz using an acousto-optical modulator and the reflected probe beam was monitored using a lock-in amplifier.

Figure 43 shows the typical pump-probe reflectivity response of the implanted specimens. The oscillations from the CAP wave can be seen superimposed over the usual peak and decay of the thermal pump-probe response. It is standard in the analysis of CAP experiments for the thermal response to be subtracted out, leaving only the CAP oscillations.

VI.2 Results

VI.2.1 Coherent Acoustic Phonon Interferometry

The lower six panels of Figure 44 show CAP oscillation signals for diamond specimens implanted at fluences from $3 \times 10^{14} \text{ cm}^{-2}$ to $3 \times 10^{16} \text{ cm}^{-2}$. For clarity, noisy regions of the CAP response near zero time delay have been removed from the plots for the two

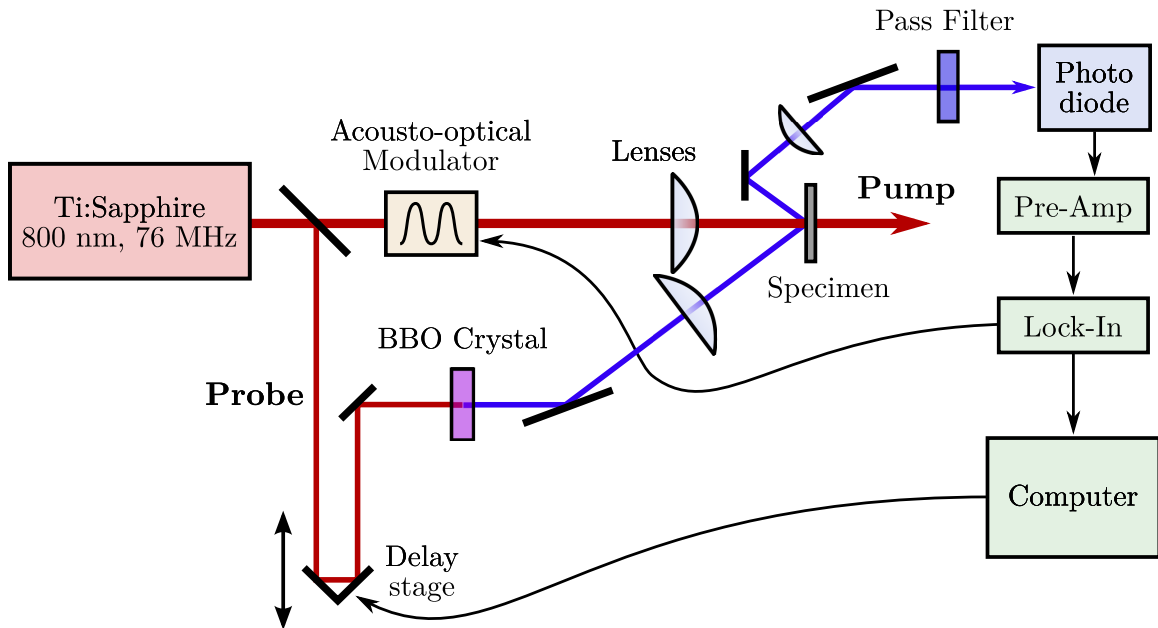


Figure 42: Experimental setup for CAP measurement of ion implanted diamonds.

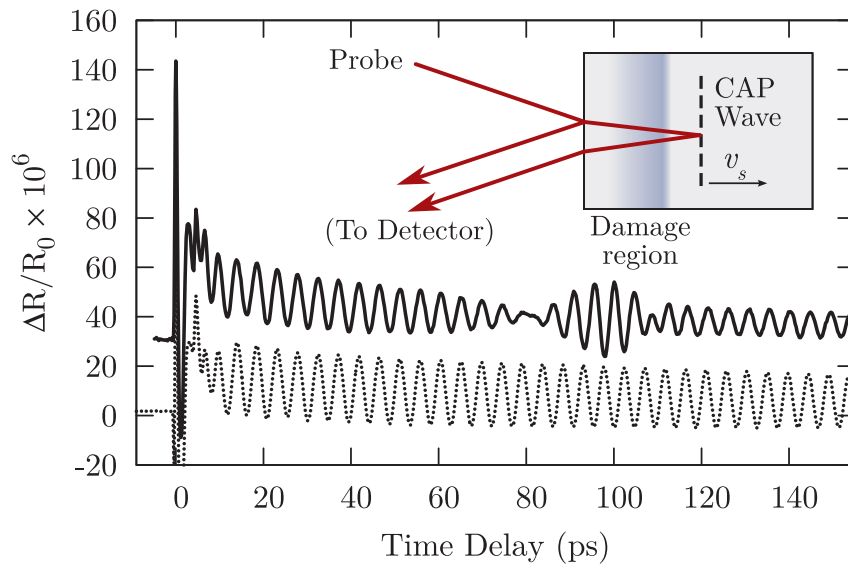


Figure 43: Typical pump-probe reflectivity responses for implanted (solid) and unimplanted (dotted) diamonds, vertically offset for clarity. Data are relevant to a sample implanted at a fluence of $3 \times 10^{15} \text{ cm}^{-2}$. Inset: CAP experiment configuration showing strain-wave induced self-interference in the probe reflectivity.

lowest fluences. At He^+ fluences below $3 \times 10^{14} \text{ cm}^{-2}$, no damage-induced modulation of the CAP signal is apparent, and at fluences above 10^{17} cm^{-2} , no CAP oscillations are observed due to the strong absorption of the probe pulse in the damaged region.

Three important features of the data are noted here, and will be explored in detail below. The most striking feature in the oscillations is the ‘pulse’ that increases in width and shifts toward smaller time delays as the implantation fluence is increased. Comparison of the implanted curves with the corresponding unimplanted behavior shows that the regions before and after this pulse feature are essentially in phase with the unimplanted oscillations, but that the pulse feature itself is 180° out of phase with the unimplanted oscillations. In all cases the direct out-of-phase behavior ceases beyond the damaged region.

In addition to the above, there is a small phase delay between the implanted and unimplanted oscillations in the out-of-phase region and the region after it, which increases with increasing fluence. For the higher fluences, this small phase change is noticeable well before the strain wave reaches the peak of the implantation damage.

Finally, the amplitude of the oscillations beyond the damaged region decreases with increasing implantation fluence, and disappears entirely at the highest fluence shown. The time-domain decay toward this decreased persistent amplitude begins in the out-of-phase region.

Some previous experimental studies of ion-implanted diamond [136, 168, 169] have observed surface swelling due to the volume expansion of the amorphized lattice. For instance, Bosia et al. [136] observed surface swelling of $\sim 100 \text{ nm}$ in a diamond specimen implanted with 1.8 MeV He^+ ions at a fluence of $4.18 \times 10^{16} \text{ cm}^{-2}$. Although such swelling could in principle influence the depth characteristics of the CAP experiment, the fluences used in this study are below that reported by Bosia et al., and even at the highest fluences, the oscillations are damped out before reaching the peak of the

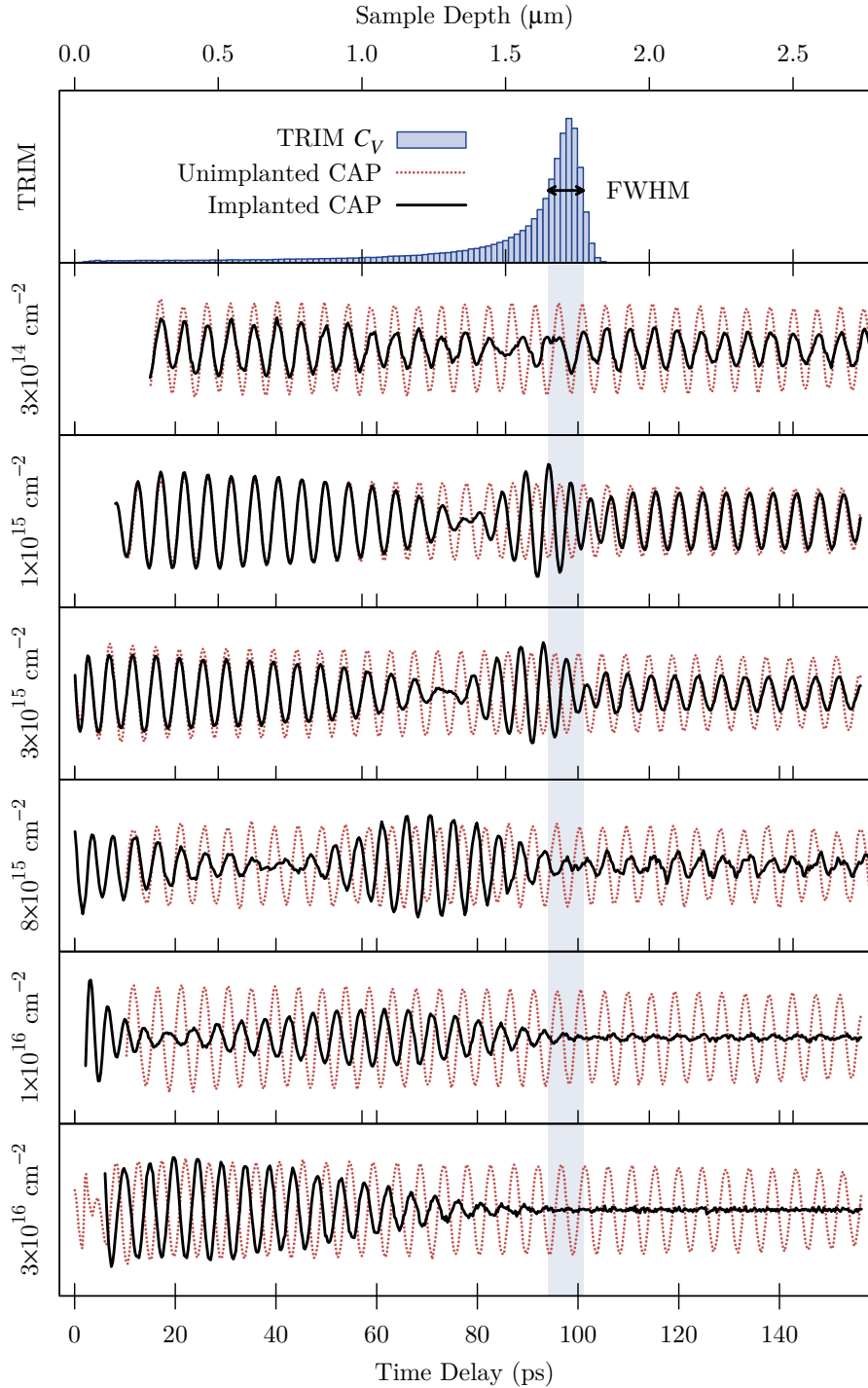


Figure 44: CAP oscillations in the pump-probe reflectivity signal of ion-implanted diamond specimens at multiple fluences (dark lines). The dotted line behind each curve is the corresponding response for an unimplanted specimen. Above the CAP responses is damage-induced vacancy distribution as calculated by the TRIM code. The vertical bar indicates the full width at half maximum of the TRIM vacancy profile.

implantation damage, where any swelling effects would be most noticeable. In addition, if there were an appreciable contribution to the CAP measurement from surface swelling, it would manifest as an increase in the apparent depth of the implanted layer, *i.e.*, the tail of the out-of-phase pulse feature would appear to shift to the right with increasing fluence. Since such behavior is not observed in the oscillations in Figure 44, and in light of the above considerations, the effect of surface swelling in these studies is taken to be negligible.

VI.2.2 Transmission Electron Microscopy

Since the concept of vacancy concentrations has proven to be such a useful tool for quantifying damage to implanted materials, the analysis that follows relies on the implantation-induced vacancy concentration profile as calculated by the TRIM code (Figure 44, top panel) to describe the damage to the diamond lattice. To verify the accuracy of the TRIM calculation, cross-sectional lamellae were cut out of the implanted specimens and studied under transmission electron microscopy, as shown in Figures 45 and 46. The TEM image in Figure 46 is for the $3 \times 10^{16} \text{ cm}^{-2}$ specimen, and shows a thick band of implantation damage at the location of the peak predicted by the TRIM profile. The damage peak in Figure 45, which depicts the 10^{15} cm^{-2} specimen, is more faint, but is also in excellent agreement with the TRIM prediction. The use of the TRIM code in the analysis of the CAP oscillations is justified based on these results. In addition, it is noted that the spatial extent of the implantation effects in the diamond specimens is much broader in the opto-electronic properties (as measured by CAP) than in the visible structural changes to the lattice shown by TEM.

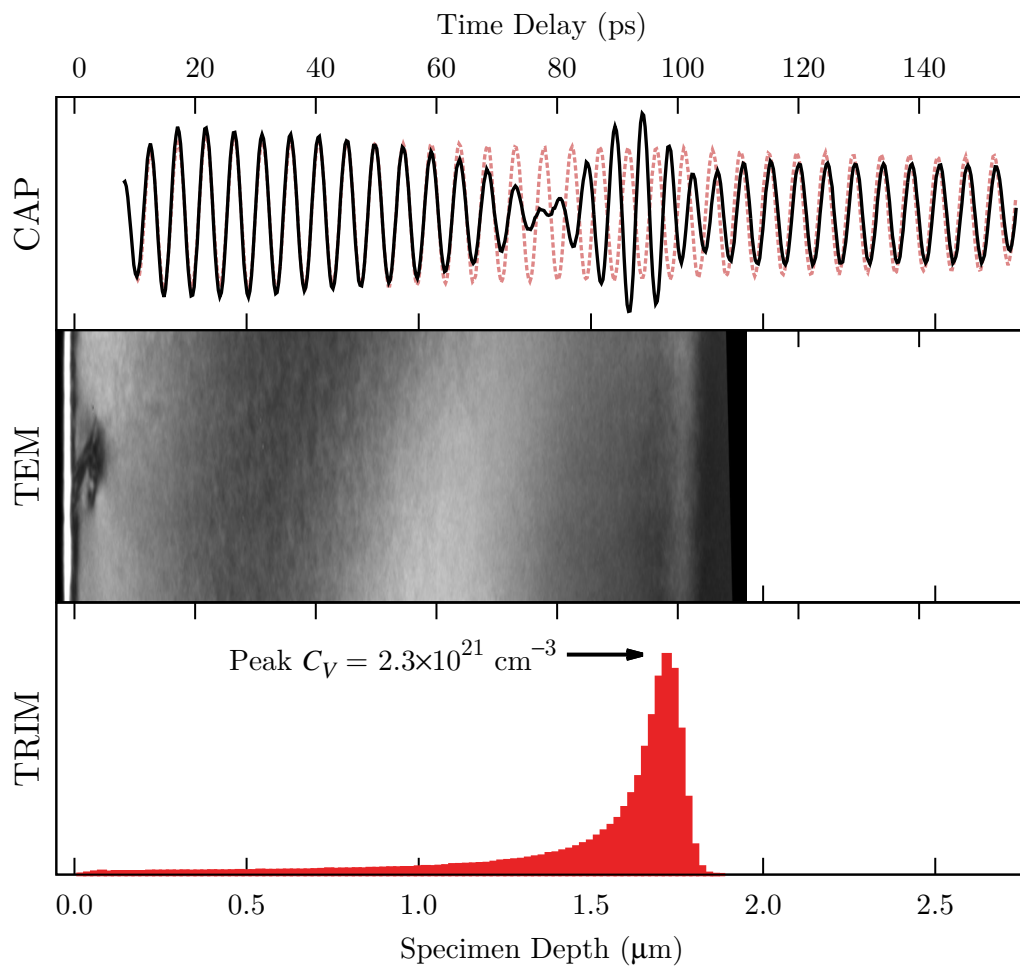


Figure 45: Comparison of CAP oscillations with cross-sectional TEM for the 10^{15} cm^{-2} implantation. TEM image is of bright field two-beam diffraction, with $\mathbf{g} = (220)$. The predicted TRIM vacancy concentration profile is shown at the bottom for reference.

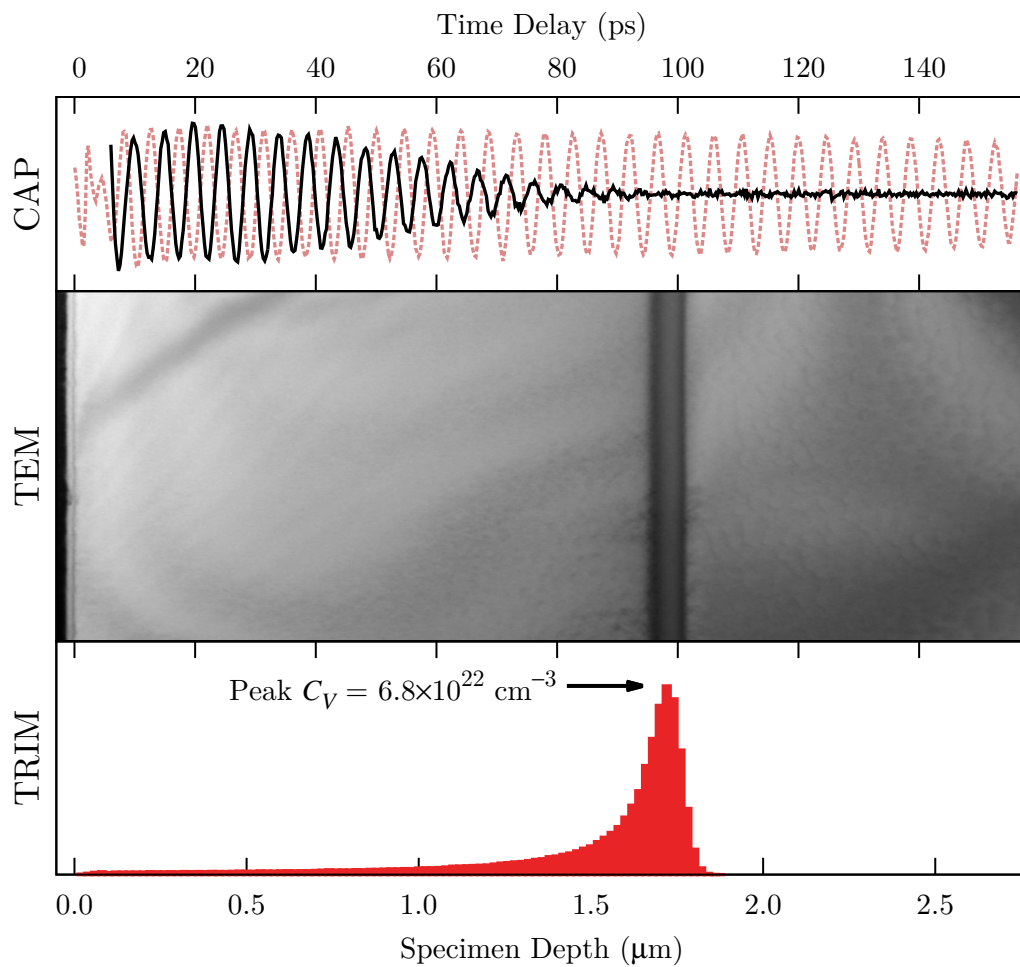


Figure 46: Comparison of CAP oscillations with cross-sectional TEM for the $3 \times 10^{16} \text{ cm}^{-2}$ implantation. TEM image is of bright field two-beam diffraction, with $\mathbf{g} = (220)$. The predicted TRIM vacancy concentration profile is shown at the bottom for reference.

VI.3 Discussion

The features noted in the reflectivity data are due to a variety of damage-induced modifications to the optical properties of the diamond lattice. In addition to the following discussion of these features, a full quantitative treatment is given in Chapter VII.

VI.3.1 Phase Reversal

The time delay of the pump-probe reflectivity signal may be correlated with crystal depth by simple multiplication with the longitudinal speed of sound, which in diamond is $17.52 \text{ nm}\cdot\text{ps}^{-1}$, as reported in the top axis of Figure 44. This enables the features in the reflectivity signal to be mapped directly against the damage-induced vacancy concentration profile as calculated by TRIM. Figure 47(a) shows for each fluence the TRIM vacancy concentration at the ‘node depth,’ where the onset of the out-of-phase behavior appears, and at the peak amplitude of the out-of-phase region. The vacancy concentrations for the node depths in particular are in good agreement across the range of fluences, with an average concentration of $C_{V\text{-node}} = (3.9 \pm 0.9) \times 10^{20} \text{ cm}^{-3}$.

The 180° out-of-phase behavior in the CAP oscillations and the physical significance of the critical vacancy concentration $C_{V\text{-node}}$ can be explained within a model incorporating an empirical dependency of photoelasticity on defect concentration. The amplitude of the CAP oscillations is proportional to the reflectivity of the CAP strain wave, which comes from the strain-induced modulation of the real refractive index of the local lattice. Thus,

$$R_{CAP} \propto \frac{dn}{d\eta}(C_V(z)) \times \eta(z, t), \quad (28)$$

where R_{CAP} is the strain wave reflectivity, η is the local strain due to the traveling CAP wave, and $dn/d\eta$ is related to the p_{12} component of the photoelastic tensor, [160]

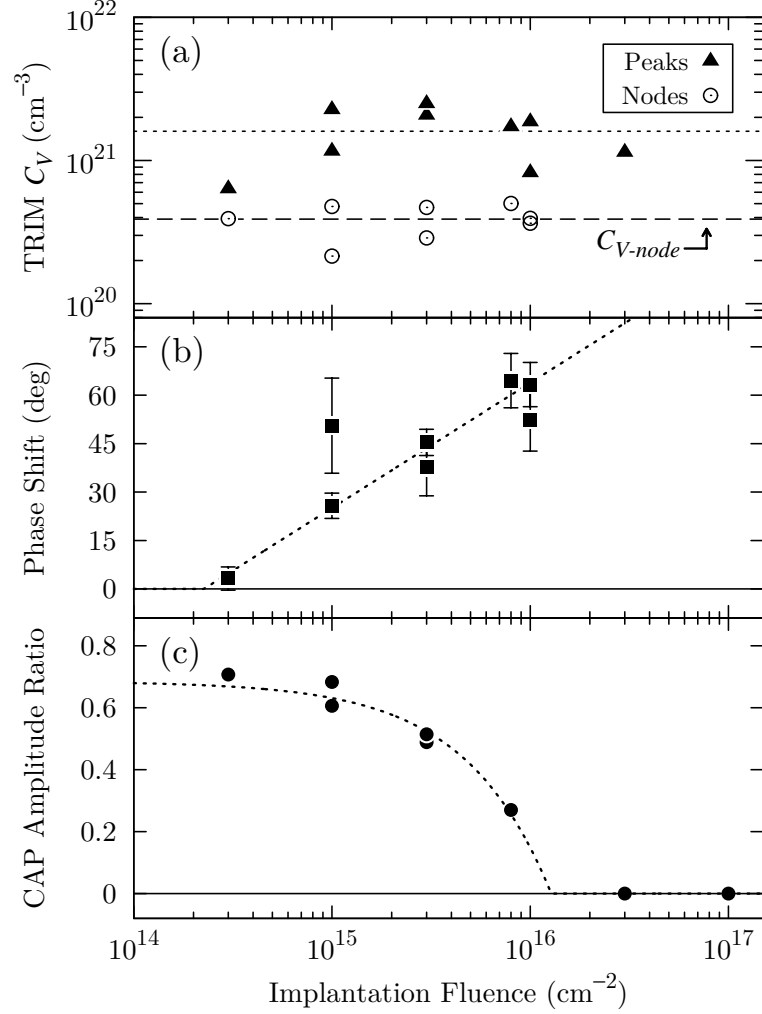


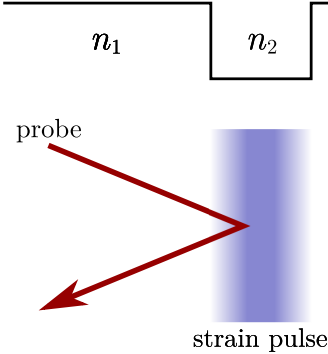
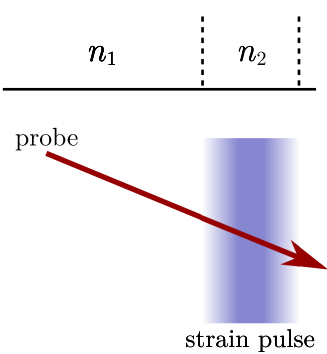
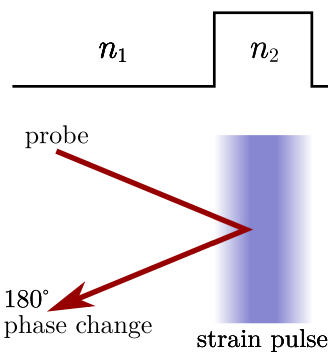
Figure 47: Variations in CAP oscillation features with He^+ implantation fluence. (a) TRIM vacancy concentrations for the initial node and peak of the out-of-phase ‘pulse’ feature. The lines at $1.6 \times 10^{21} \text{ cm}^{-3}$ (dotted) and $C_{V-node} = 3.9 \times 10^{20} \text{ cm}^{-3}$ (dashed) are the respective average vacancy concentrations for the peaks and nodes. (b) Cumulative phase shift resulting from the damage-induced increase in the real index, n . The line is a guide to the eye. (c) Amplitude of the oscillations beyond the damage layer as a fraction of the oscillation amplitude before the out-of-phase behavior. The line is a linear fit to the data.

which in these specimens varies with the implantation-induced vacancy concentration, $C_V(z)$. The $dn/d\eta$ term in diamond is ordinarily negative at 400 nm, [170] thus if we imagine for the sake of argument that the strain wave is a simple positive square pulse, it generates a traveling optical interface with a high-to-low transition in the real refractive index. (The argument given here is valid regardless of the shape of the CAP pulse, which in reality is more complex. [156]) As the vacancy concentration increases toward C_{V-node} , $dn/d\eta$ increases toward zero and the CAP amplitude diminishes. At $C_V = C_{V-node}$, $dn/d\eta = 0$, and the strain induces no change in the refractive index of the lattice, thus the CAP oscillations disappear. As C_V continues to increase beyond C_{V-node} , $dn/d\eta$ becomes positive. Now the CAP wave generates an optical interface with a low-to-high index transition, and the reflected probe light undergoes a phase shift of 180° . This reverses the constructive and destructive interference of the recombined probe beam at the surface, resulting in the direct out-of-phase behavior observed in the reflectivity data. This explanation is summarized in Table 6. Since the amplitude of the CAP oscillations in the phase-inverted region often exceeds that of the oscillations near the surface, the absolute magnitude of the photoelastic coefficient in these regions is believed to exceed that for an undisturbed diamond lattice.

VI.3.2 Cumulative Phase Shift

Figure 47(b) shows, at each fluence for which data was available, the phase shift between the implanted and unimplanted specimens in the oscillations beyond the damaged region, determined from the data by cross-correlation. The data show a monotonic increase with He^+ implantation fluence. This phase shift is due to a decrease in the real refractive index of the damaged diamond lattice, which results in a decreased optical path length for the probe pulse as it traverses the specimen to the strain wave and back again. Because of this, the phase shift is manifested cumulatively with time delay as the strain wave traverses more of the specimen's

Table 6: Summary of the explanation for the phase reversal behavior in the CAP oscillations at $C_V = 3.9 \times 10^{20} \text{ cm}^{-3}$.

$C_V < 3.9 \times 10^{20} \text{ cm}^{-3}$	$C_V = 3.9 \times 10^{20} \text{ cm}^{-3}$	$C_V > 3.9 \times 10^{20} \text{ cm}^{-3}$
$dn/d\eta < 0$ $n_1 > n_2$	$dn/d\eta = 0$ $n_1 = n_2$	$dn/d\eta > 0$ $n_1 < n_2$
		

modified optical path length, and appears most strongly in the region beyond the implantation damage.

Comparison to Literature

There is currently disagreement in the literature about the effect of ion implantation on diamond's refractive index. This study, along with the reports by Khomich et al. [146] and to a degree Draganski et al. [152], finds a decreasing index after ion bombardment, in apparent contradiction to other reports [106, 148, 151–153] that find an index increase.

The increased index result that some groups have reported is intriguing. In most crystals, ion implantation damage decreases the atomic density of the lattice by introducing vacancies, thereby decreasing the refractive index. However, there are other

potential influences, as shown in the Wei modification to the Lorentz-Lorenz equation: [171, 172]

$$\frac{\Delta n}{n} = \frac{1}{6n^2} (n^2 - 1) (n^2 + 2) \left[\frac{\Delta N}{N} + \frac{\Delta \alpha}{\alpha} + \frac{\Delta \chi}{\chi} \right]. \quad (29)$$

Here, the Δ terms refer to implantation-induced modifications to the unperturbed physical properties, while N is the atomic density, α is the polarizability of the lattice atoms, and χ is a structure factor. As previously mentioned, ΔN is negative and usually predominates, but the $\Delta \alpha$ and $\Delta \chi$ contributions may be positive or negative. In diamond, one or both of these terms might overcome the density loss. In particular, given the strong covalent bonding in the diamond lattice, it is not surprising that structural modifications can induce large changes in polarizability, especially when one considers the possibility of changing sp^3 bonds to sp^2 . On the other hand, the structure factor χ is a correction for crystals that are either non-cubic or non-amorphous, [172] and thus should be negligible for both pristine and fully-amorphized diamond specimens, but it may play a role at intermediate levels of damage. However, if this contribution is responsible for the observed increase in the refractive index, it is unclear why such an effect would be unique to diamond, and not to other crystals with diamond-cubic arrangement, such as silicon. Therefore, discrepancies within the literature and with the current work are most likely due to variations in the relative modifications to the density and polarizability of the implanted diamond specimens.

There are multiple potential explanations for the current discrepancy among experimental studies of this subject. Table 7 lists the relevant experimental parameters from the available literature. Lagomarsino et al. [153] have suggested that the difference is due to low-fluence vs. high-fluence implantation regimes, but the present work shows that the index can decrease at low fluences as well.

The difference between this work and the reports from the Olivero group [148, 151, 153] could be explained by choice of wavelength, which for this work was 400 nm (3.1 eV) and for theirs was 632.8 nm (1.96 eV). If this is the case, the specific roles of the various optical defect bands introduced by the implantations would have to be considered, as well as the variation in polarizability between these two frequencies.

The implantation ion species is another possible factor, and He is unique to the studies exhibiting decreased refractive index. Although this discussion has primarily focused on vacancies, the concentration of the implanted ions themselves may be significant. This is due to the fact that for diamond, higher implantation fluences are required to create the same number of vacancies as can be achieved with lower fluences in other materials. This effect likely stems from the strength of the carbon-carbon bonds in the diamond lattice. For the 1.0 MeV He⁺ ions used in this study, the peak helium concentration is about 20% of the peak vacancy concentration. Helium diffusion in lightly and moderately damaged diamond crystals is negligible at room temperature, [173] therefore the implanted helium concentrations are not expected to change after the initial implantation. Whereas implanted hydrogen, boron, or carbon ions may all bond with the surrounding lattice, interstitial helium is chemically inert, [174] thus it may be reasonable to expect a difference in the polarizability of the lattice for helium implantations as compared to other species.

Another possible explanation involves the inherent ambiguity in the CAP technique between the real part of the refractive index and the speed of sound. Based on previous experimental work, [108] it has been assumed in this study that the longitudinal speed of sound in the implanted diamonds is unaffected by the damage to the lattice. However, if this is not the case, the observed phase shift could be attributed to a decreased speed of sound in the implanted region, which would compete with the increased refractive index. However, if this were the case, it would again be expected that the apparent end of the damaged region in the reflectivity oscillations would

shift toward deeper time delays with increasing fluence, and this is not observed in the experimental data.

Finally, as Table 7 shows, there is a 1–2 order of magnitude difference in ion current density between the current work and the H implantations by the Olivero group [148, 153], suggesting the possibility that the discrepancy may be accounted for by dynamic annealing effects, which can occur at room temperature. [97] (Although data are available, it is difficult to judge the relevance of ion current density and dynamic annealing to the work by Hines et al. [106], as their specimens were annealed to high temperatures after implantation). It is noted that the implantations in the present work were performed below 0 °C specifically to avoid dynamic self-annealing.

VI.3.3 Persistent Amplitude Loss

The final feature of note in the CAP oscillations is the persistent loss of amplitude in the region beyond the implantation damage. Figure 47(c) shows the ratio of the amplitude of the CAP oscillations beyond the damage region to the amplitude near zero time delay at each fluence for which clear amplitudes could be obtained. The ratio decreases linearly with increasing implantation fluence, up to the point where oscillations are no longer observed and the ratio is zero. This persistent amplitude loss is due to depletion of the internally-reflected beam, and can be attributed either to phonon-defect scattering of the CAP wave in the damaged region of the specimen, thereby decreasing R_{CAP} , or to defect-induced scattering and absorption of the probe photons.

To distinguish these two effects, simple optical transmittance experiments (in the absence of a phonon wave) comparing the implanted and unimplanted regions of the specimens were performed. The results are shown in Figure 48. As can be seen, the transmission experiment exhibited the same optical loss in the implanted regions as is exhibited in the CAP experiments, which suggests that CAP wave decoherence does

Table 7: Experimental parameters and results from available works studying the variation in real refractive index of ion irradiated diamond crystals. Here, E_{ion} is the energy of the implanting ions, I is the ion current, d is the ion beam diameter at the specimen, J is the ion current density at the specimen, $T_{impl.}$ is the nominal temperature of the specimen during implantation, and λ are the wavelengths at which the refractive index was measured. An asterisk (*) next to the implantation temperatures denotes specimens that were annealed after implantation.

Reference	Crystal Type	Ion Species	E_{ion} (MeV)	Fluences (cm ⁻²)
[148, 153]	CVD IIa	H ⁺	2, 3	10 ¹⁵ – 10 ¹⁷
This work	CVD IIa	He ⁺	1	3 × 10 ¹⁴ – 3 × 10 ¹⁶
[146]	Natural	He ⁺	0.35	4.9 × 10 ¹⁶
[151]	CVD IIa	B ⁺	0.18	10 ¹³ – 5 × 10 ¹⁴
[106]	Natural	C ⁺	0.02	5 × 10 ¹³ – 2.1 × 10 ¹⁵
[145]	Natural IIa	C ⁺	0.05–1.5	1.5 × 10 ¹⁴ – 10 ¹⁷
[152]	HPHT Ib	Ga ⁺	0.03	10 ¹³ – 5 × 10 ¹⁴

Table 7, continued:

Reference	I (nA)	d (μm)	J (A/m ²)	$T_{impl.}$ (K)
[148, 153]	1	10, 20	3, 12	~300
This work	200	1,000	0.25	< 273
[146]	-	-	-	300*
[151]	-	-	-	-
[106]	20	500	0.1	300*
[145]	-	-	-	77
[152]	-	-	-	-

Table 7, continued:

Reference	Characterization technique	λ (nm)	Result
[148, 153]	Reflection interferometry	632.8	increased n
This work	CAP interferometry	400	decreased n
[146]	Spectroscopic ellipsometry	350 – 1050	decreased n
[151]	Spectroscopic ellipsometry	250 – 1700	increased n
[106]	Reflectivity	450 – 650	increased n
[145]	Reflectivity / transmission	200 – 2500	inconclusive
[152]	Spectroscopic ellipsometry	190 – 2100	both

not contribute significantly to the observed oscillation amplitude loss. Therefore, the observed amplitude loss is attributed to an increase in the optical absorption, specifically the imaginary part of the refractive index, in the damaged regions of the specimens. This finding is easily verified by the naked eye, as the implanted regions grow increasingly opaque with implantation fluence, and are completely black at the highest fluences.

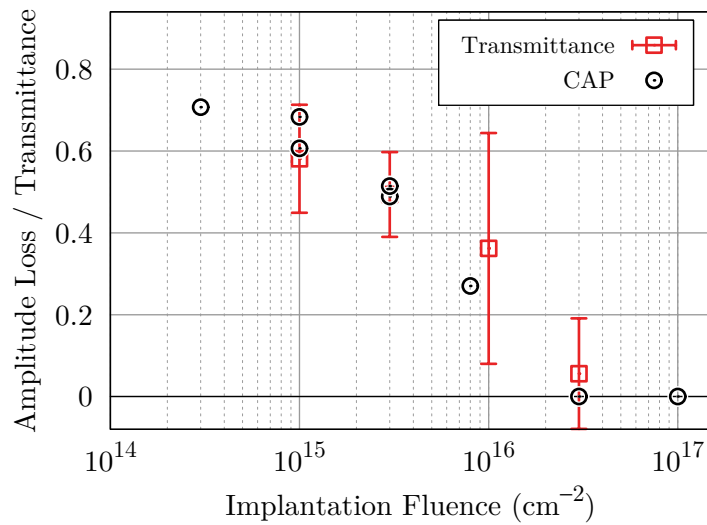


Figure 48: Comparison between persistent amplitude loss in the CAP oscillations and the optical transmittance of the implanted specimens at 400 nm.

CHAPTER VII

PHENOMENOLOGICAL MODEL

This chapter begins by describing the motivation for and limitations associated with a phenomenological model for the implantation-induced variation in the optical characteristics of diamond. Then a simple analytical approach that yields good agreement with a limited set of experimental observations is presented, followed by a description of a more detailed numerical model which allows for the simulation of the full CAP reflectivity response of the implanted specimens.

VII.1 Objective and Limitations

Since ion implantation is likely to become a key component in the manufacturing process for diamond-based quantum information devices (see Chapter IV), it is imperative to understand the ways in which ion implantation modifies the optical characteristics of diamond crystals. In particular, a quantitative model that can accurately predict damage-induced optical modulations would be a desirable tool for device design. The purpose of the work described in this chapter is to provide such a phenomenological model for helium implanted diamonds, based on the experimental results presented in Chapter VI.

From a more fundamental point of view, it is also clearly desirable to understand the underlying physical mechanisms responsible for the observed optical modifications. However, although the quantitative model presented here may provide valuable clues for such an investigation, the question lies beyond the scope of the present work. One recent report [175] suggests that *ab initio* calculations based on density

functional theory may be a viable approach for beginning to answer these more fundamental questions, particularly with respect to the effect of implantation defects on the acousto-optical response.

VII.2 Analytical Approach

VII.2.1 Introduction

Three important features of the experimental data were noted in Chapter VI:

1. A ‘pulse’ feature in regions with vacancy concentrations above $3.9 \times 10^{20} \text{ cm}^{-3}$, in which the oscillations from the implanted specimens reversed phase with the oscillations from the unimplanted specimens. This feature was attributed to a sign reversal in the p_{12} component of the photoelastic tensor.
2. A small, cumulative phase delay between the oscillations for implanted and unimplanted specimens, which increased with increasing ion fluence. This effect was attributed to a decrease in the real part of the refractive index within the damaged layer.
3. A loss of oscillation amplitude in the implanted specimens, which persisted into the specimen at depths beyond the implantation layer, and was attributed to a damage-induced increase in the imaginary part of the refractive index.

The second and third features, which together represent the damage-induced variation in the complex refractive index of the lattice, are manifested most clearly in the region beyond the implantation damage, and can be described using a simple analytical model. The behavior of the first feature requires a more sophisticated approach and will be addressed later in Section VII.3.

VII.2.2 Relationship to Experimental Observables

It is assumed that the local complex index of the implanted crystal can be represented solely as a function of the vacancy concentration, *i.e.*,

$$\tilde{n}(z) = n + i\kappa = \tilde{n}(C_V(z)). \quad (30)$$

In order to evaluate the merit of different analytical models for $\tilde{n}(C_V)$, it is first necessary to establish quantitative relationships between the experimental observables and the two components n and κ .

Phase Shift

The observed phase shift in the oscillations beyond the damage region is due to the damage-induced optical path difference experienced by the probe pulse as it traverses the specimen to the strain wave and back. The one-way difference in the optical path length between the implanted and unimplanted specimens is:

$$OPD_{1-way} = \int_0^z [n(z) - n_0] dz = \int_0^z n(C_V(z)) dz - n_0 z, \quad (31)$$

where n_0 is the real index of the undamaged lattice and the integration is carried out from the surface to some depth z beyond the implantation damage. The resulting phase shift in the CAP oscillations (in radians) is:

$$\theta = 2 \times 2\pi \left(\frac{OPD_{1-way}}{T_z} \right) = \frac{2\pi n_0}{\lambda} \left[\int_0^z n(C_V(z)) dz - n_0 z \right]. \quad (32)$$

Here, positive θ denotes a shift toward greater time delays, *i.e.*, to the right in Figure 44, the initial factor of 2 accounts for the double traversal of the implantation damage by the probe pulse, and $T_z = \lambda/2n_0$ is the period of the undamaged oscillations in the depth domain.

Amplitude Loss

The persistent amplitude loss in the oscillations beyond the damaged region can be related to $\kappa(z)$ by employing a depth-dependent form of the Beer-Lambert law, which describes the loss in the intensity of light as it traverses an absorbing medium:

$$\frac{dE}{dz} = -\frac{\alpha(z)}{2}E. \quad (33)$$

Here $\alpha = 4\pi\kappa/\lambda$ is the linear absorption coefficient, which in the implanted specimens will vary with depth. The electric field form of the law is presented here rather than the usual intensity form because it is the electric fields which recombine interferometrically at the specimen surface. Solving this equation yields the amplitude loss ratio E/E_0 in the CAP oscillations beyond the damaged region as compared to the oscillations in the undamaged specimens:

$$\frac{E}{E_0} = \exp \left[-\frac{4\pi}{\lambda} \int_0^z \kappa(z) dz \right]. \quad (34)$$

The exponential term in Equation 34 has been squared to account for the two passes of the optical probe through the damaged region.

VII.2.3 Phenomenological Model

Lagomarsino et al. [153] found good agreement with experimental results by employing a linear model for the dependence of \tilde{n} on vacancy concentration:

$$\tilde{n}(C_V) = \tilde{n}_0 + \tilde{c}C_V. \quad (35)$$

However, as they point out, this model is valid for a limited range of C_V , as at higher levels of damage approaching the amorphization limit the optical modulation saturates. A simple exponential model which accounts for this saturation was employed

successfully by Battiato et al., [151] and serves as a basis for the current work:

$$n(C_V) = n_0 + (n_\infty - n_0) [1 - \exp(-C_V/a)], \quad (36)$$

$$\kappa(C_V) = \kappa_0 + (\kappa_\infty - \kappa_0) [1 - \exp(-C_V/b)]. \quad (37)$$

Here, n_0 and κ_0 refer to the characteristics of the undamaged lattice, while n_∞ and κ_∞ denote saturation values at high vacancy concentrations. The parameters a and b give the vacancy concentrations at which the two optical modulations have reached $1 - 1/e$ (or 63%) saturation.

VII.2.4 Calculation and Results

Equations 32 and 34 were evaluated simultaneously at each fluence for which experimental data were available using the above exponential model for $\tilde{n}(C_V)$, with n_∞ , κ_∞ , a , and b as fitting parameters. The vacancy concentration profile $C_V(z)$ was provided by the TRIM code, as described in Chapter VI. The invariant parameters n_0 and κ_0 were determined by fitting an exponentially decaying sine function to the oscillations observed in the unimplanted specimens. The real index n_0 was found to be the same for all specimens, with a value of 2.4542, assuming a sound velocity of 17.52 nm/ps. The imaginary index κ_0 varied depending on the specimen, with values from 0.00133 to 0.00362. For the parameter fit, the average value of 0.002488 was used.

The fixed parameters and the parameters giving the best fit to the experimental data are listed in Table 8. Figure 49 shows the variation in the two components of $\tilde{n}(C_V)$ over a range of vacancy concentrations. The comparison to experimental results is given in Figure 50.

In general the agreement of the model with experimental results is very good. A few interesting points are worth noting. The first is that the observed decrease in

Table 8: Constant and best fit parameters for the exponential model given in Equations 36 and 37 using the analytical approach.

Parameter	Value
n_0	2.454 2
n_∞	2.438 7
a	$1.78 \times 10^{20} \text{ cm}^{-3}$
κ_0	0.002 488
κ_∞	0.119
b	$8.00 \times 10^{21} \text{ cm}^{-3}$

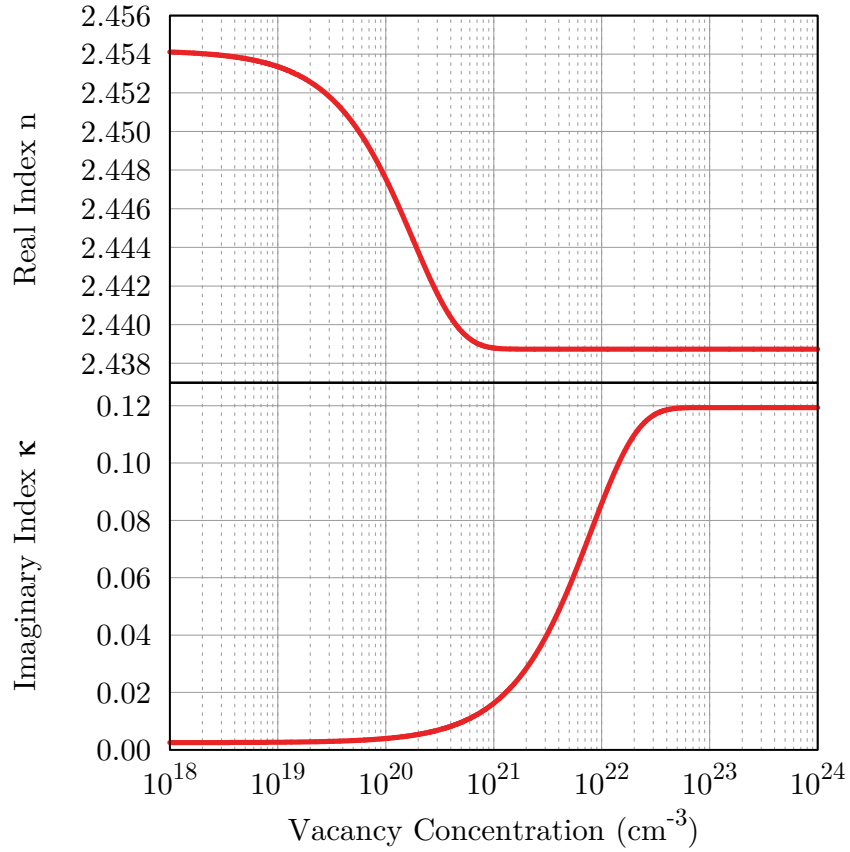


Figure 49: Variation in the real and imaginary components of $\tilde{n}(C_V)$ over a range of vacancy concentrations, using the parameters given in Table 8.

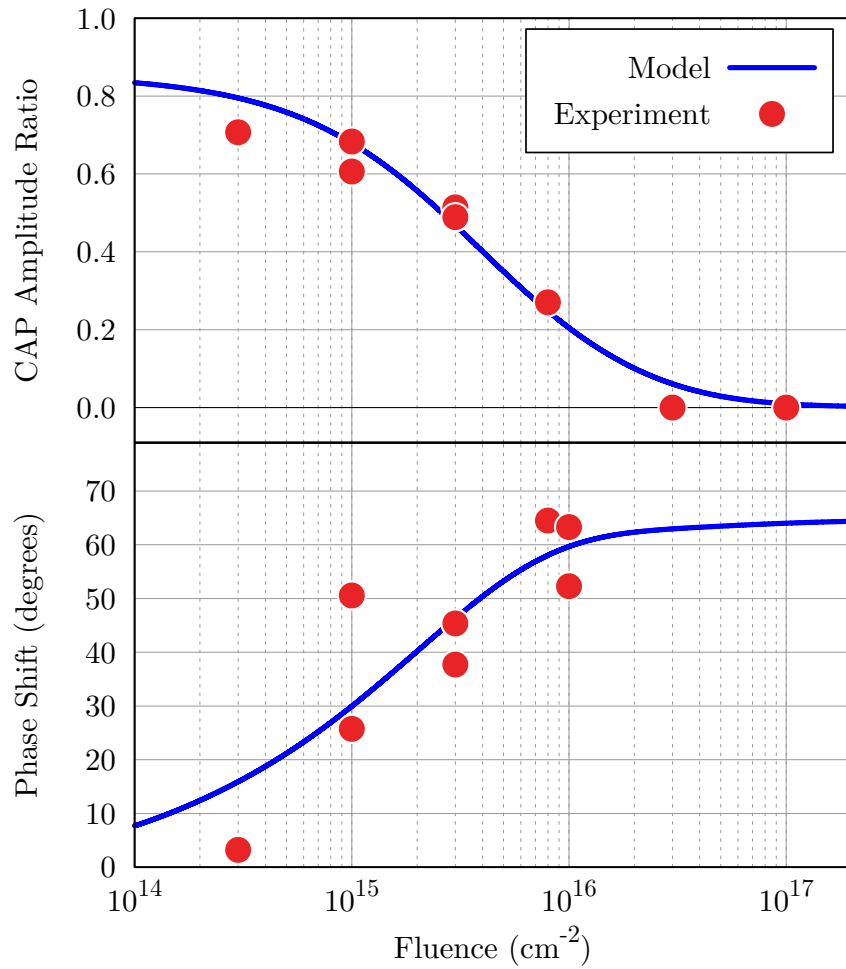


Figure 50: Comparison of the exponential model given in Equations 36 and 37 using an analytical approach with the parameters from Table 8, along with experimental data from Chapter VI.

the refractive index of 0.0155 (0.63%) is relatively small. For comparison, Battiato et al. [151] observed an increase of ~ 0.09 (3.7%) at the saturation limit. In addition, in [151] it was found that the saturation parameter a was $1.5 \times 10^{21} \text{ cm}^{-3}$, whereas in the present work a is found to be $1.78 \times 10^{20} \text{ cm}^{-3}$, an order of magnitude smaller. Possible explanations for these discrepancies have been discussed in Section VI.3.2. Finally, it is interesting to note that the modulation in n occurs in the 10^{19} – 10^{21} cm^{-3} range of vacancy concentrations, while the range for the modulation in κ is 10^{21} – $2 \times 10^{22} \text{ cm}^{-3}$. This suggests that the underlying mechanisms responsible for the damage-induced modulation of the two components may be different.

VII.3 Numerical Simulation

The convenience of the analytical approach presented above stems from the fact that the effect of the implantation damage on the complex refractive index could be easily quantified by considering two separable properties of the reflectivity oscillations beyond the damage region. However, since the phase reversal effect (pulse feature) is manifested solely in the damaged region and modulates the oscillation amplitude and phase in a way that is not easily separable from the variations in n and κ , a more detailed approach that directly considers the interactions between the damaged lattice, the probe photons, and the propagating strain wave is required. In this case, a numerical approach with the goal of fully reproducing the observed time-domain reflectivity oscillations in the implanted diamond specimens is applied.

VII.3.1 Theory

The photoelastic effect describes the variation in the refractive properties of a material due to strain. For an isotropic material under uniaxial strain, as is the case in CAP studies on diamond crystals, it can be shown [160] that the strain-induced variation

in the complex index is

$$\frac{d\tilde{n}}{d\eta} = -\frac{\tilde{n}^3}{2}p_{12}, \quad (38)$$

where η is the uniaxial strain and p_{12} (contracted notation) is one of two unique components of the real fourth-rank photoelastic tensor. It is noted that the single quantity p_{12} determines both $dn/d\eta$ and $d\kappa/d\eta$.

The first-order calculation of the photo-induced propagating strain pulse has been provided by Thomsen et al.: [156]

$$\eta(z, t) = (1 - R) \frac{Q\beta}{A\zeta C} \frac{1 + \nu}{1 - \nu} \left[e^{-z/\zeta} \left(1 + \frac{1}{2}e^{-v_s t/\zeta} \right) - \frac{1}{2}e^{-|z - v_s t|/\zeta} \text{sgn}(z - v_s t) \right]. \quad (39)$$

Here Q and A are the pump pulse energy and beam area, respectively, v_s is the longitudinal speed of sound in the host crystal, and R , β , C , ν , and ζ respectively represent the reflectivity, linear expansion coefficient, volume specific heat capacity, Poisson ratio, and optical absorption length of the transducing layer.

Using Equations 38 and 39, and provided one has a model for how the optical characteristics are modulated by the implantation damage, it is possible to calculate the strain-induced variation in the complex index of an ion-implanted crystal as a function of crystal depth and time t after the incidence of the pump pulse:

$$\tilde{n}(z, t) = \tilde{n}(C_V(z)) - \frac{1}{2} \left[\tilde{n}(C_V(z)) \right]^3 p_{12}(C_V(z)) \eta(z, t). \quad (40)$$

VII.3.2 Calculation

The time-domain reflectivity of the implanted specimens is calculated using a numerical approach that employs the multiplication of homogeneous characteristic matrices for a series of discrete layers, [160,176] each with a unique value of \tilde{n} as determined by Equation 40. This approach is computationally inexpensive and fully accounts for any complex interference effects that may be caused by multiple internal reflections. The

code was tested for accuracy against previous calculations for complex multilayered dielectric films prior to applying it to the case of CAP reflectivity oscillations.

The exponential model given in Equations 36 and 37 has been employed again in this analysis, with the addition of three new parameters to describe the behavior of $p_{12}(C_V)$:

$$p_{12}(C_V) = p_{12,0} + (p_{12,\infty} - p_{12,0}) [1 - \exp(-C_V/c)]. \quad (41)$$

In this case, the fixed model parameters are n_0 and κ_0 , while n_∞ , κ_∞ , $p_{12,0}$, $p_{12,\infty}$, a , b , and c are varied so as to fit the experimental data. The fitting algorithm was the Nelder-Mead simplex method [177] provided by the GNU Scientific Library. [178]

The experimental and simulation-specific parameters that were used for the numerical calculation are listed in Table 9. Due to variations in the transducing layer deposition as well as fluctuations in laser beam alignment, there was some variation in the relative amplitudes of the measured CAP oscillations from specimen to specimen. This was accounted for by using the parameters given in Table 9 for all fluences, but varying the reflectivity for each specimen based on fits to the unimplanted oscillations. In addition, as mentioned previously, there were variations in the optical absorption of the undamaged lattice for the different specimens. Whereas in the previous analytical approach an average absorption was used at all fluences, here the respective fitted value for κ_0 has been used for each fluence. Finally, the Thomsen model for the strain wave generation does not account for the time required for the photoexcited electrons in the transducing layer to couple with the phonon modes in the lattice that eventually result in the propagating strain pulse. As a result, there is a difference in time delay of 4.5–5.5 ps between the experiment and the simulation. The variability of this difference may be attributed to variations in the deposition of the transducing layer, and has been corrected at each fluence by applying the appropriate time domain shift to the simulation results to align the phases of the initial oscillations.

The specimen-specific adjustments described above are all listed together in Table 10.

Table 9: Experimental and simulation parameters used in the numerical simulation of the CAP reflectivity oscillations. Values for the parameters that vary with fluence are given in Table 10.

Parameter	Symbol	Value	
Depth sampling resolution		0.1	nm
Crystal			
Unperturbed real index	n_0	2.454	2
Unperturbed imaginary index	κ_0	(varies)	
Sound velocity	v_s	17.52	nm/ps
Aluminum Transducing Layer			
Absorption length	ζ	7.6	nm
Specific head capacity	C	0.91	J/g-K
Poisson's ratio	ν	0.334	
Linear expansion coefficient	β	2.3	$\times 10^{-5}$
Reflectivity	R	(varies)	
Laser			
Probe wavelength	λ	0.400	μm
Pump pulse energy	Q	3.95	nJ
Pump spot area	A	7.85	$\times 10^3 \mu\text{m}^2$

VII.3.3 Results and Discussion

The resulting best fit parameters from the fitting procedure are given in Table 11. The resulting variation in the optical characteristics and the comparison to the experimental results are shown in Figures 51 and 52, respectively.

As can be seen in Figure 52, the quantitative model is highly successful in reproducing the observed experimental results, with a few minor exceptions. One is in the oscillations at the $8 \times 10^{15} \text{ cm}^{-2}$ fluence, for which the underestimated amplitude is

Table 10: Specimen-specific properties used in the full numerical simulation.

Fluence (cm^{-2})	Reflectivity R	κ_0	Time delay correction (ps)
3×10^{14}	0.98	0.0013 327 6	5.5
1×10^{15}	0.77	0.0017 699 7	5.5
3×10^{15}	0.80	0.0025 353 2	4.5
8×10^{15}	0.955	0.0020 460 5	5.5
1×10^{16}	0.908	0.0036 221 0	5.5
3×10^{16}	0.905	0.0036 218 8	4.25

Table 11: Best fit parameters for the exponential model given in Equations 36, 37, and 41 using the full numerical simulation.

Parameter	Value
n_0	2.454 2
n_∞	2.438 9
a	$3.418 \times 10^{19} \text{ cm}^{-3}$
κ_0	(see Table 10)
κ_∞	0.114
b	$2.229 \times 10^{21} \text{ cm}^{-3}$
p_{12-0}	0.044
$p_{12-\infty}$	-0.101
c	$1.177 \times 10^{21} \text{ cm}^{-3}$

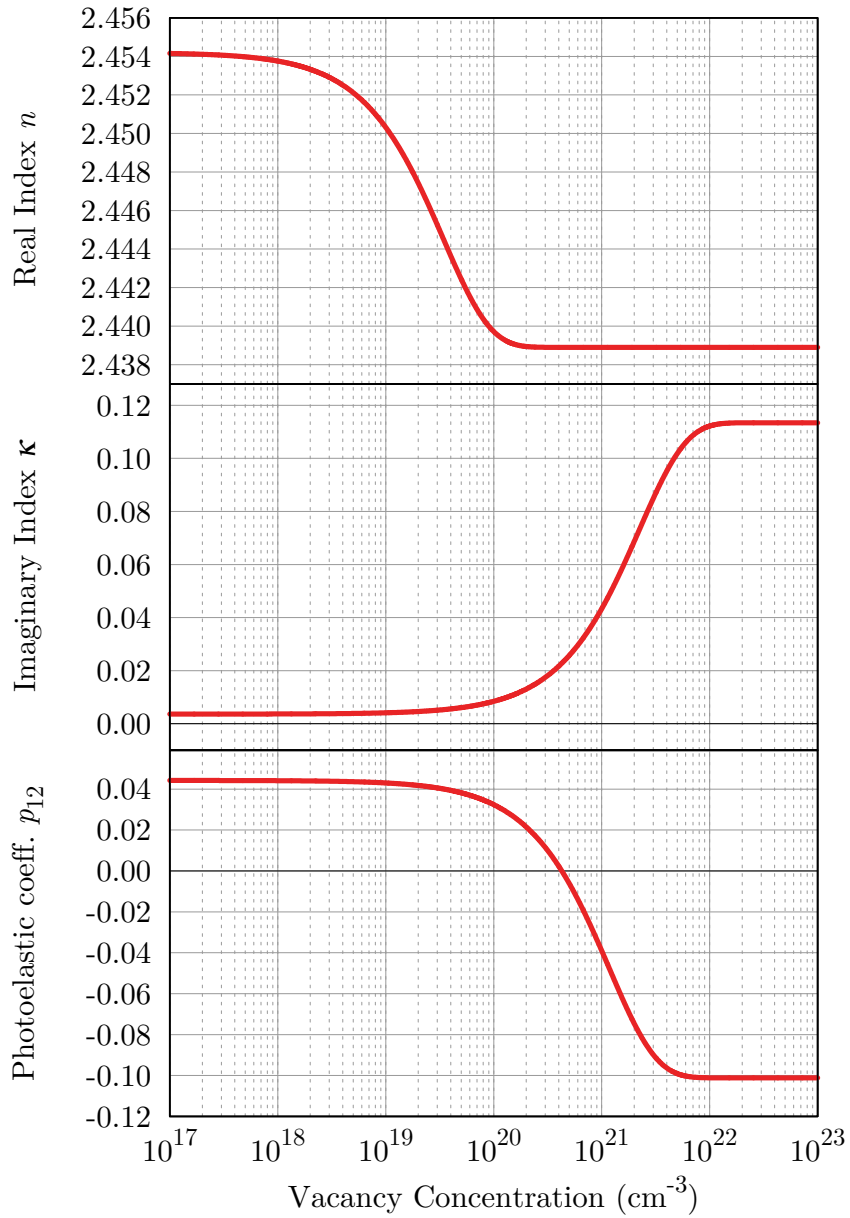


Figure 51: Variation in the real and imaginary components of $\tilde{n}(C_V)$ and $p_{12}(C_V)$ over a range of vacancy concentrations, using the parameters given in Table 11.

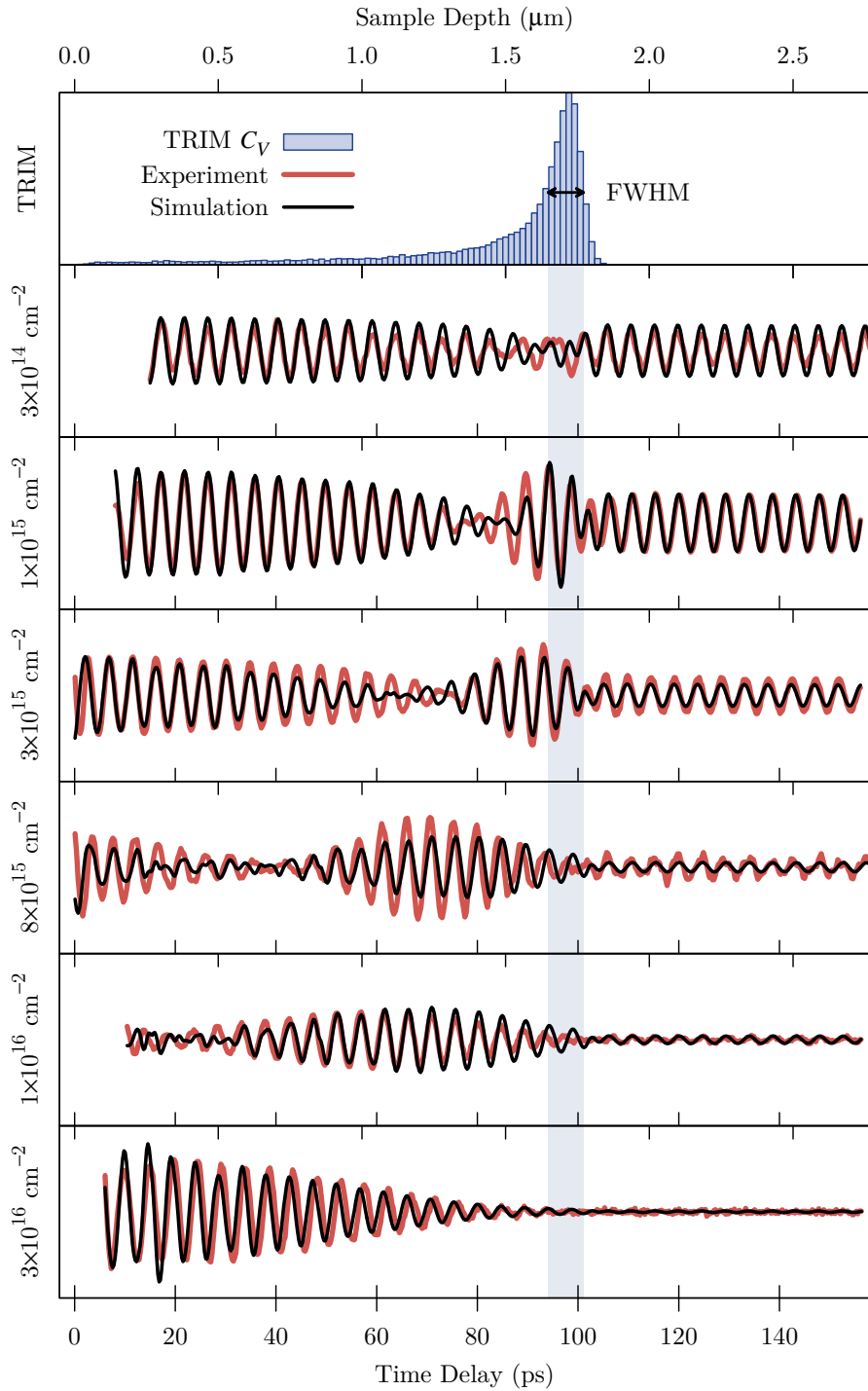


Figure 52: Comparison of the best fit of the exponential model given in Equations 36, 37, and 41 to the experimental data from Chapter VI.

probably due to an excessively high value for the transducing layer reflectivity parameter R . Another discrepancy can be seen near the node positions for the lower fluences, where the onset of the out-of-phase behavior occurs. This is the point where the p_{12} photoelastic coefficient crosses from positive to negative, thus the oscillation pattern is highly sensitive to the vacancy concentration at these positions. The most likely causes for the observed discrepancies are uncertainty in the exact implantation fluence as well as irregularities in the TRIM calculation, both of which could lead to incorrect estimates of the vacancy concentration near these points.

Considering the results in Figure 51, it can be seen that the modulation in the real component of the refractive index n with vacancy concentration occurs from 10^{18} cm^{-3} to 10^{20} cm^{-3} , while for κ and p_{12} the modulation occurs at higher levels of damage, namely from 10^{20} cm^{-3} to 10^{22} cm^{-3} . Although the reasons for this difference are not immediately clear, it once again suggests that the damage-induced modulation in n may occur via a fundamentally different mechanism than the other two properties.

It is also noted that the critical vacancy concentration at which the p_{12} coefficient reverses sign agrees exactly with the value extracted from the experimental data in Chapter VI. That said, the absolute magnitudes of the derived values for p_{12-0} and $p_{12-\infty}$ are subject to a heightened degree of uncertainty due to variations in the deposition of the transducing layer and fluctuations in the reflectivity signal due to laser alignment drift, both of which can affect the overall amplitude of the CAP oscillations. Other potential sources of uncertainty include the possibility of ballistic conduction of pump-excited electrons into the diamond lattice before they can couple to phonon modes in the aluminum transducing layer, which would broaden the optical interface generated by the CAP wave, and partial ablation of the transducing layer due to prolonged exposure to the focused laser beam. However, the ratio $p_{12-\infty}/p_{12-0}$, the saturation rate c , and the aforementioned zero crossing point should all be unaffected

by these considerations. In addition, the derived value for p_{12-0} is found to be in good agreement with *ab initio* calculations. [179]

The exponential model presented in this chapter for the damage-induced modulation to the optical characteristics of diamond is simple, has a rational conceptual basis, and provides good agreement with experimental results for nominal vacancy concentrations up to $\sim 5 \times 10^{22} \text{ cm}^{-3}$. Thus, it may prove to be a useful predictive tool for optical device design. However, it is by no means the only quantitative model that might be applied to this system. In particular, the recent finding by Fairchild et al. [94] that the diamond lattice rapidly collapses into amorphous carbon at a vacancy concentration of $2.8 \times 10^{22} \text{ cm}^{-3}$ suggests a two-phase model featuring an abrupt change in optical characteristics at the critical value for C_V . Even so, the levels of damage studied in this work only reach the critical value at the highest fluences, and then only at the peak of the implantation damage, where the CAP oscillation amplitude has already decayed to essentially zero. Therefore the current work is unable to speak to the validity of such a model. In order to address the lattice collapse model, specimens would need to be implanted at high fluences using low energy ions, which would bring the damage peak closer to the specimen surface and allow for optical characterization before the probe pulse is totally absorbed.

VII.4 Potential Expansion Studies

There are numerous opportunities to further the studies presented in this chapter and Chapter VI. One experiment of potentially high value to the diamond community would be to anneal the implanted diamond specimens at successive temperatures and observe the effect on the CAP reflectivity response. Another would be to expand the wavelength range from 400 nm to the full visible spectrum, with special emphasis given to the absorption wavelengths of optical centers such as the NV^- . In the effort to solve the current experimental discrepancies regarding the behavior of the

real refractive index under implantation conditions, it may also be fruitful to expand the implantation parameters to other energies, temperatures, and ion species. Finally, density functional theory may prove to be valuable for comparing the effects of specific defect species within the diamond lattice on the optical and photoelastic properties of the material.

CONCLUSIONS

The characterization of nonlinear optical absorption in semiconductors is of interest both from a fundamental perspective and from a technological vantage, as nonlinear absorption processes play a key role in all-optical device switching. In Part I of this work, by employing a combination of infrared transmittance experiments and numerical analysis, the two- and three-photon absorption coefficients β and γ for germanium have been evaluated over the range of wavelengths from 2.8 to 5.2 μm . The ratios of the coefficients across the direct/indirect gap transitions and between the two- and three-photon cases, which are less susceptible to experimental uncertainties than the absolute coefficients, have also been determined. Comparison with theoretical studies shows excellent agreement.

In Part II, the ultrafast optical technique known as coherent acoustic phonon interferometry has been applied to He^+ ion-irradiated diamond crystals for the purpose of determining the optical modification induced by the implantation damage. This subject is of critical interest to the field of quantum information systems, as diamond is a strong contender to become the host material for a room-temperature quantum computer, and ion implantation is likely to be a critical component of quantum device fabrication processes. The experimental results provide information about the variation at 400 nm in the complex refractive index of the implanted specimens as well as the variation in the photoelastic tensor. Specifically, a decrease in the real refractive index of the lattice due to the ion implantation has been observed, along with an increase in the imaginary component. In addition, the p_{12} component of the photoelastic tensor is observed to reverse sign above a vacancy concentration of $3.9 \times 10^{20} \text{ cm}^{-3}$. Finally, a simple phenomenological model quantitatively describing

the damage-induced optical modification has been developed which accurately predicts the experimental observations, and may prove to be a useful tool for quantum device design.

REFERENCES

- [1] V Nathan, A. H. Guenther, and S. S. Mitra. Review of multiphoton absorption in crystalline solids. *Journal of the Optical Society of America B*, 2(2):294–316, 1985.
- [2] E. W. Van Stryland, Y. Y. Wu, D. J. Hagan, M. J. Soileau, and K. Mansour. Optical limiting with semiconductors. *Journal of the Optical Society of America B*, 5(9):1980–1988, 1988.
- [3] T. Boggess, A. Smirl, S. Moss, I. Boyd, and E. Van Stryland. Optical limiting in GaAs. *IEEE Journal of Quantum Electronics*, 21(5):488–494, 1985.
- [4] A. Villeneuve, C. C. Yang, G. I. Stegeman, C. N. Ironside, G. Scelsi, and R. M. Osgood. Nonlinear absorption in a GaAs waveguide just above half the band gap. *IEEE Journal of Quantum Electronics*, 30(5):1172–1175, May 1994.
- [5] E. Garmire. Resonant optical nonlinearities in semiconductors. *IEEE Journal of Selected Topics in Quantum Electronics*, 6(6):1094–1110, 2000.
- [6] K. L. Vodopyanov, O. Levi, P. S. Kuo, T. J. Pinguet, J. S. Harris, M. M. Fejer, B. Gerard, L. Becouarn, and E. Lallier. Optical parametric oscillation in quasi-phase-matched GaAs. *Optics Letters*, 29(16):1912–1914, 2004.
- [7] S. C. Abbi and S. A. Ahmad. *Non-linear optics and laser spectroscopy*. Narosa Pub. House, New Delhi, 2001.
- [8] Germanium band structure and carrier concentration. Retrieved from <http://www.ioffe.ru/SVA/NSM/Semicond/Ge/bandstr.html> on March 18, 2010.
- [9] S. M. Sze. *Physics of Semiconductor Devices*, page 13. John Wiley & Sons, 2nd edition, 1981.
- [10] M. Sheik-Bahae and M. P. Hasselbeck. Nonlinear refraction. *Encyclopedia of Optical Engineering*, pages 1501–1510, 2003.
- [11] W. C. Hurlbut, Y-S Lee, K. L. Vodopyanov, P. S. Kuo, and M. M. Fejer. Multiphoton absorption and nonlinear refraction of GaAs in the mid-infrared. *Optics Letters*, 32(6):668–670, 2007.
- [12] M. Sheik-Bahae, A. A. Said, D. J. Hagan, M. J. Soileau, and E. W. Van Stryland. Nonlinear refraction and optical limiting in ‘thick’ media. *Optical Engineering*, 30(8):1228–1235, 1991.
- [13] M. Sheik-Bahae, A. A. Said, T. H. Wei, D. J. Hagan, and E. W. Van Stryland. Sensitive measurement of optical nonlinearities using a single beam. *IEEE Journal of Quantum Electronics*, 26(4):760–769, 1990.

- [14] M. Göppert-Mayer. Elementary processes with two quantum transitions. *Annalen der Physik*, 18(7-8):466–479, 2009. (Translation of original 1931 dissertation.)
- [15] W. Kaiser and C. G. B. Garrett. Two-photon excitation in $\text{CaF}_2:\text{Eu}^{2+}$. *Physical Review Letters*, 7(6):229, 1961.
- [16] M. Lipeles, R. Novick, and N. Tolk. Direct detection of two-photon emission from the metastable state of singly ionized helium. *Physical Review Letters*, 15(17):690–693, Oct 1965.
- [17] R. Braunstein. Nonlinear optical effects. *Physical Review*, 125(2):475, 1962.
- [18] C. M. Cirloganu, P. D. Olszak, L. A. Padilha, S. Webster, D. J. Hagan, and E. W. Van Stryland. Three-photon absorption spectra of zinc blende semiconductors: theory and experiment. *Optics Letters*, 33(22):2626–2628, 2008.
- [19] D. C. Hutchings and E. W. Van Stryland. Nondegenerate two-photon absorption in zinc blende semiconductors. *Journal of the Optical Society of America B*, 9(11):2065–2074, 1992.
- [20] B. S. Wherrett. Scaling rules for multiphoton interband absorption in semiconductors. *Journal of the Optical Society of America B*, 1(1):67–72, 1984.
- [21] E. W. Van Stryland, S. Guha, H. Vanherzeele, M. A. Woodall, M. J. Soileau, and B. S. Wherrett. Verification of the scaling rule for two-photon absorption in semiconductors. *Journal of Modern Optics*, 33:381–386, 1986.
- [22] L. V. Keldysh. Ionization in the field of a strong electromagnetic wave. *Soviet Physics Journal of Experimental and Theoretical Physics*, 20, 1965.
- [23] H. S. Brandi and C. B. de Araujos. Multiphonon absorption coefficients in solids: a universal curve. *Journal of Physics C: Solid State Physics*, 16(30):5929, 1983.
- [24] L. P. Gonzalez, J. M. Murray, S. Krishnamurthy, and S. Guha. Wavelength dependence of two photon and free carrier absorptions in InP. *Optics Express*, 17(11):8741–8748, 2009.
- [25] Srinivasan Krishnamurthy, Zhi Gang Yu, Leonel P. Gonzalez, and Shekhar Guha. Accurate evaluation of nonlinear absorption coefficients in InAs, InSb, and HgCdTe alloys. *Journal of Applied Physics*, 101(11):113104, 2007.
- [26] S. Krishnamurthy, Z. G. Yu, S. Guha, and L. Gonzalez. High intensity light propagation in InAs. *Applied Physics Letters*, 89(16):161108, 2006.
- [27] B. N. Murdin, R. Rangel-Rojo, C. R. Pidgeon, M. F. Kimmitt, A. K. Kar, D. A. Jaroszynski, J. M. Ortega, R. Prazeres, F. Glotin, and D. C. Hutchings. Excite-probe FEL (CLIO) study of two-photon-induced carrier dynamics in narrow gap semiconductors. *Nuclear Instruments and Methods in Physics Research*

Section A: Accelerators, Spectrometers, Detectors and Associated Equipment, 341(1-3):165–168, 1994.

- [28] M. D. Dvorak, W. A. Schroeder, D. R. Andersen, A. L. Smirl, and B. S. Wherrett. Measurement of the anisotropy of two-photon absorption coefficients in zincblende semiconductors. *IEEE Journal of Quantum Electronics*, 30(2):256–268, 1994.
- [29] B. N. Murdin, C. R. Pidgeon, A. K. Kar, D. A. Jaroszynski, J. M. Ortega, R. Prazeres, F. Glotin, and D. C. Hutchings. Infrared free electron laser measurement of two-photon absorption in InAs and InSb over a wide spectral range. *Optical Materials*, 2(2):89–93, 1993.
- [30] A. A. Said, M. Sheik-Bahae, D. J. Hagan, T. H. Wei, J. Wang, J. Young, and E. W. Van Stryland. Determination of bound-electronic and free-carrier nonlinearities in ZnSe, GaAs, CdTe, and ZnTe. *Journal of the Optical Society of America B*, 9(3):405–414, 1992.
- [31] E. W. Van Stryland, H. Vanherzeele, M. A. Woodall, M. J. Soileau, A. L. Smirl, S. Guha, and T. F. Boggess. Two photon absorption, nonlinear refraction, and optical limiting in semiconductors. *Optical Engineering*, 24(4):613–623, 1985.
- [32] J. H. Yee and H. H. M. Chau. Two-photon indirect transition in GaP crystal. *Optics Communications*, 10(1):56–58, 1974.
- [33] J. F. Reintjes and J. C. McGroddy. Indirect two-photon transitions in Si at 1.06 μm . *Physical Review Letters*, 30(19):901, 1973.
- [34] A. Franceschetti, J. W. Luo, J. M. An, and A. Zunger. Origin of one-photon and two-photon optical transitions in PbSe nanocrystals. *Physical Review B*, 79(24):241311, 2009.
- [35] S. Uryu, H. Ajiki, and T. Ando. Excitonic two-photon absorption in semiconducting carbon nanotubes within an effective-mass approximation. *Physical Review B*, 78(11):115414, 2008.
- [36] L. Pan, A. Ishikawa, and N. Tamai. Detection of optical trapping of CdTe quantum dots by two-photon-induced luminescence. *Physical Review B*, 75(16):161305, 2007.
- [37] L. A. Padilha, J. Fu, D. J. Hagan, E. W. Van Stryland, C. L. Cesar, L. C. Barbosa, C. H. B. Cruz, D. Buso, and A. Martucci. Frequency degenerate and nondegenerate two-photon absorption spectra of semiconductor quantum dots. *Physical Review B*, 75(7):075325, 2007.
- [38] H. C. Lee, A. Kost, M. Kawase, A. Hariz, P. D. Dapkus, and E. M. Garmire. Nonlinear absorption properties of AlGaAs/GaAs multiple quantum wells grown by metalorganic chemical vapor deposition. *IEEE Journal of Quantum Electronics*, 24(8):1581–1592, 1988.

- [39] F. Adduci, I. M. Catalano, A. Cingolani, and A. Minafra. Direct and indirect two-photon processes in layered semiconductors. *Physical Review B*, 15(2):926–931, Jan 1977.
- [40] A. F. Gibson, C. B. Hatch, P. N. D. Maggs, D. R. Tilley, and A. C. Walker. Two-photon absorption in indium antimonide and germanium. *Journal of Physics C: Solid State Physics*, 9(17):3259, 1976.
- [41] I. M. Catalano, A. Cingolani, and A. Minafra. Multiphoton transitions at the direct and indirect band gaps of gallium phosphide. *Solid State Communications*, 16(4):417–420, 1975.
- [42] I. M. Catalano, A. Cingolani, and A. Minafra. Transmittance, luminescence, and photocurrent in CdS under two-photon excitation. *Physical Review B*, 9(2):707–710, Jan 1974.
- [43] D. A. Kleinman, R. C. Miller, and W. A. Nordland. Two-photon absorption of Nd laser radiation in GaAs. *Applied Physics Letters*, 23(5):243–244, 1973.
- [44] A. M. Danishevskii, A. A. Patrin, S. M. Ryvkin, and I. D. Yaroshetskii. The effect of stimulated free carrier absorption on two-photon conductivity in semiconductors. *Soviet Physics Journal of Experimental and Theoretical Physics*, 29, 1969.
- [45] S. Guha, A. Zakei, J. L. Blackshire, and S. Krishnamurthy. Irradiance and temperature dependence of the charge carrier lifetimes in bulk $\text{Hg}_{0.6}\text{Cd}_{0.4}\text{Te}$. *Applied Physics Letters*, 83(1):78–80, 2003.
- [46] C. Rauscher and R. Laenen. Analysis of picosecond mid-infrared pulses by two-photon absorption in germanium. *Journal of Applied Physics*, 81(6):2818–2821, 1997.
- [47] F. Bassani and A. Hassan. Analysis of indirect two-photon interband transitions and of direct three-photon transitions in semiconductors. *Il Nuovo Cimento B*, 7(2):313–332, 1972.
- [48] E. Tuncel, J. L. Staehli, C. Coluzza, G. Margaritondo, J. T. McKinley, R. G. Albrige, A. V. Barnes, A. Ueda, X. Yang, and N. H. Tolk. Free-electron laser studies of direct and indirect two-photon absorption in germanium. *Physical Review Letters*, 70(26):4146, 1993.
- [49] G. W. Bryant, P. Kelly, D. Ritchie, P. Braunlich, and A. Schmid. Interaction of intense picosecond pulses of 2.7- μm photons with germanium. *Physical Review B*, 25(4):2587, 1982.
- [50] Y. K. Danileiko, A. A. Manenkov, and A. V. Sidorin. Laser-induced damage in semiconductors. In A. J. Glass and A. H. Guenther, editors, *Laser-Induced Damage in Optical Materials*, page 4. American Society for Testing and Materials, 1978.

- [51] A. Elci, M. O. Scully, A. L. Smirl, and J. C. Matter. Ultrafast transient response of solid-state plasmas. I. Germanium, theory, and experiment. *Physical Review B*, 16(1):191, 1977.
- [52] H. Garcia and K. N. Avnani. Direct and indirect two-photon absorption in Ge within the effective mass approximation. *Applied Physics Letters*, 100(13):131105, 2012.
- [53] B. V. Zubov, L. A. Kulevskii, V. P. Makarov, T. M. Murina, and A. M. Prokhorov. Two-photon absorption in germanium. *Journal of Experimental and Theoretical Physics Letters*, 9(4):130, 1969.
- [54] R. G. Wenzel, G. P. Arnold, and N. R. Greiner. Nonlinear loss in Ge in the 2.54 μm range. *Applied Optics*, 12(10):2245–2247, 1973.
- [55] T. J. Wagner, M. J. Bohn, Jr. R. A. Coutu, L. P. Gonzalez, J. M. Murray, K. L. Schepler, and S. Guha. Measurement and modeling of infrared nonlinear absorption coefficients and laser-induced damage thresholds in Ge and GaSb. *Journal of the Optical Society of America B*, 27(10):2122–2131, Oct 2010.
- [56] D. Seo, J. M. Gregory, L. C. Feldman, N. H. Tolk, and P. I. Cohen. Multiphoton absorption in germanium using pulsed infrared free-electron laser radiation. *Physical Review B*, 83(19), May 2011.
- [57] K. H. Müller, G. Nimtz, and M. Selders. Fast CO₂ laser modulation by hot carriers. *Applied Physics Letters*, 20(8):322–323, 1972.
- [58] C. J. Kennedy, J. C. Matter, A. L. Smirl, H. Weiche, F. A. Hopf, S. V. Pappus, and M. O. Scully. Nonlinear absorption and ultrashort carrier relaxation times in germanium under irradiation by picosecond pulses. *Physical Review Letters*, 32(8):419, 1974.
- [59] C. V. Shank and D. H. Auston. Parametric coupling in an optically excited plasma in Ge. *Physical Review Letters*, 34(8):479, 1975.
- [60] A. L. Smirl, J. C. Matter, A. Elci, and M. O. Scully. Ultrafast relaxation of optically excited nonequilibrium electron-hole distributions in germanium. *Optics Communications*, 16(1):118–120, 1976.
- [61] A. Othonos, H. M. van Driel, Jeff F. Young, and Paul J. Kelly. Hot-carrier dynamics in Ge on single picosecond timescales: Comparing Raman and reflectivity experiments with a self-consistent kinetic model. *Solid-State Electronics*, 32(12):1573–1577, 1989.
- [62] X. Q. Zhou, H. M. van Driel, and G. Mak. Femtosecond kinetics of photoexcited carriers in germanium. *Physical Review B*, 50(8):5226, 1994.

- [63] G. Mak and W. W. Rüle. Femtosecond carrier dynamics in Ge measured by a luminescence up-conversion technique and near-band-edge infrared excitation. *Physical Review B*, 52(16):R11584, 1995.
- [64] E. Gaubas, M. Bauza, A. Uleckas, and J. Vanhellemont. Carrier lifetime studies in Ge using microwave and infrared light techniques. *Materials Science in Semiconductor Processing*, 9(4-5):781–787, 2006.
- [65] G. S. Edwards, D. Evertson, W. Gabella, R. Grant, T. L. King, J. Kozub, M. Mendenhall, J. Shen, R. Shores, S. Storms, and R. H. Traeger. Free-electron lasers: reliability, performance, and beam delivery. *IEEE Journal of Selected Topics in Quantum Electronics*, 2(4):810–817, Dec 1996.
- [66] J. A. Kozub, B. Feng, and W. E. Gabella. Measurements of the spectral and temporal evolution of FEL macropulses. In *Proc. SPIE 4633, Commercial and Biomedical Applications of Ultrafast and Free-Electron Lasers*, pages 153–161, 2002.
- [67] D. Seo, L. C. Feldman, N. H. Tolk, and P. I. Cohen. Interaction of high-power infrared radiation with germanium. In *Proc. SPIE 7132, Laser-Induced Damage in Optical Materials*, pages 713216–713216–9, 2008.
- [68] W. Kaiser, R. J. Collins, and H. Y. Fan. Infrared absorption in *p*-type germanium. *Physical Review*, 91:1380–1381, Sep 1953.
- [69] E. Gaubas and J. Vanhellemont. Dependence of carrier lifetime in germanium on resistivity and carrier injection level. *Applied Physics Letters*, 89(14):142106, 2006.
- [70] M. Levinshtein, S. Rumyantsev, and M. Shur, editors. *Handbook Series on Semiconductor Parameters*, volume 1. World Scientific, 1996.
- [71] H. M. van Driel, L.-A. Lompre, and N. Bloembergen. Picosecond time-resolved reflectivity and transmission at 1.9 and 2.8 μm of laser-generated plasmas in silicon and germanium. *Applied Physics Letters*, 44(3):285–287, 1984.
- [72] D. H. Auston, C. V. Shank, and P. LeFur. Picosecond optical measurements of band-to-band Auger recombination of high-density plasmas in germanium. *Physical Review Letters*, 35:1022–1025, Oct 1975.
- [73] S. Krishnamurthy. In *IR Materials Meeting, Dayton, OH*, 2010.
- [74] A. D. Bristow, N. Rotenberg, and H. M. van Driel. Two-photon absorption and Kerr coefficients of silicon for 850–2200 nm. *Applied Physics Letters*, 90(19):191104, 2007.
- [75] D. H. Reitze, T. R. Zhang, W. M. Wood, and M. C. Downer. Two-photon spectroscopy of silicon using femtosecond pulses at above-gap frequencies. *Journal of the Optical Society of America B*, 7(1):84–89, Jan 1990.

- [76] H. Garcia and R. Kalyanaraman. Phonon-assisted two-photon absorption in the presence of a DC-field: the nonlinear Franz-Keldysh effect in indirect gap semiconductors. *Journal of Physics B: Atomic, Molecular and Optical Physics*, 39(12):2737, 2006.
- [77] J. E. Field. *The Properties of diamond*. Academic Press, London; New York, 1979.
- [78] A. Laraoui, J. S. Hodges, and C. A. Meriles. Nitrogen-vacancy-assisted magnetometry of paramagnetic centers in an individual diamond nanocrystal. *Nano Letters*, 12(7):3477–3482, 2012.
- [79] J. R. Rabeau, P. Reichart, G. Tamanyan, D. N. Jamieson, S. Praver, F. Jelezko, T. Gaebel, I. Popa, M. Domhan, and J. Wrachtrup. Implantation of labelled single nitrogen vacancy centers in diamond using ^{15}N . *Applied Physics Letters*, 88(2):023113, 2006.
- [80] G. D. Fuchs, G. Burkard, P. V. Klimov, and D. D. Awschalom. A quantum memory intrinsic to single nitrogen-vacancy centres in diamond. *Nature Physics*, 7(10):789–793, Oct 2011.
- [81] S. Pezzagna, D. Rogalla, D. Wildanger, J. Meijer, and A. Zaitsev. Creation and nature of optical centres in diamond for single-photon emission—overview and critical remarks. *New Journal of Physics*, 13(3):035024, 2011.
- [82] C. Kurtsiefer, S. Mayer, P. Zarda, and H. Weinfurter. Stable solid-state source of single photons. *Physical Review Letters*, 85:290–293, Jul 2000.
- [83] T. Gaebel, M. Domhan, I. Popa, C. Wittmann, P. Neumann, F. Jelezko, J. R. Rabeau, N. Stavrias, A. D. Greentree, S. Praver, J. Meijer, J. Twamley, P. R. Hemmer, and J. Wrachtrup. Room-temperature coherent coupling of single spins in diamond. *Nature Physics*, 2(6):408–413, Jun 2006.
- [84] R. Hanson, O. Gywat, and D. D. Awschalom. Room-temperature manipulation and decoherence of a single spin in diamond. *Physical Review B*, 74:161203, Oct 2006.
- [85] M. V. G. Dutt, L. Childress, L. Jiang, E. Togan, J. Maze, F. Jelezko, A. S. Zibrov, P. R. Hemmer, and M. D. Lukin. Quantum register based on individual electronic and nuclear spin qubits in diamond. *Science*, 316(5829):1312–1316, 2007.
- [86] R. Hanson, F. M. Mendoza, R. J. Epstein, and D. D. Awschalom. Polarization and readout of coupled single spins in diamond. *Physical Review Letters*, 97:087601, Aug 2006.
- [87] A. Gruber, A. Dräbenstedt, C. Tietz, L. Fleury, J. Wrachtrup, and C. von Borzyskowski. Scanning confocal optical microscopy and magnetic resonance on single defect centers. *Science*, 276(5321):2012–2014, 1997.

- [88] G. Davies and M. F. Hamer. Optical studies of the 1.945 eV vibronic band in diamond. *Proceedings of the Royal Society of London. A. Mathematical and Physical Sciences*, 348(1653):285–298, 1976.
- [89] J. Meijer, B. Burchard, M. Domhan, C. Wittmann, T. Gaebel, I. Popa, F. Jelezko, and J. Wrachtrup. Generation of single color centers by focused nitrogen implantation. *Applied Physics Letters*, 87(26):261909, 2005.
- [90] K.-M. C. Fu, C. Santori, P. E. Barclay, A. Faraon, D. J. Twitchen, M. L. Markham, and R. G. Beausoleil. Properties of implanted and CVD incorporated nitrogen-vacancy centers: preferential charge state and preferential orientation. In Z. U. Hasan, P. R. Hemmer, H. Lee, and C. M. Santori, editors, *Proc. SPIE 7948, Advances in Photonics of Quantum Computing, Memory, and Communication IV*, volume 7948, page 79480S, San Francisco, CA, 2011. SPIE.
- [91] B. A. Fairchild, P. Olivero, S. Rubanov, A. D. Greentree, F. Waldermann, R. A. Taylor, I. Walmsley, J. M. Smith, S. Huntington, B. C. Gibson, D. N. Jamieson, and S. Praver. Fabrication of ultrathin single-crystal diamond membranes. *Advanced Materials*, 20(24):4793–4798, 2008.
- [92] F. Bosia, S. Calusi, L. Giuntini, S. Lagomarsino, A. L. Giudice, M. Massi, P. Olivero, F. Piccolo, S. Sciortino, A. Sordini, M. Vannoni, and E. Vittone. Finite element analysis of ion-implanted diamond surface swelling. *Nuclear Instruments and Methods in Physics Research Section B: Beam Interactions with Materials and Atoms*, 268(19):2991–2995, 2010.
- [93] J. F. Prins, T. E. Derry, and J. P. F. Sellschop. Volume expansion of diamond during ion implantation at low temperatures. *Nuclear Instruments and Methods in Physics Research Section B: Beam Interactions with Materials and Atoms*, 18(1-6):261–263, 1986.
- [94] B. A. Fairchild, S. Rubanov, D. W. M. Lau, M. Robinson, I. Suarez-Martinez, N. Marks, A. D. Greentree, D. McCulloch, and S. Praver. Mechanism for the amorphisation of diamond. *Advanced Materials*, 24(15):2024–2029, 2012.
- [95] A.M. Zaitsev. *Optical Properties of Diamond: A Data Handbook*. Springer, 2001.
- [96] S. Praver. Ion implantation of diamond and diamond films. *Diamond and Related Materials*, 4(5-6):862–872, 1995.
- [97] D. P. Hickey, K. S. Jones, and R. G. Elliman. Amorphization and graphitization of single-crystal diamond—a transmission electron microscopy study. *Diamond and Related Materials*, 18(11):1353–1359, 2009.
- [98] R. Kalish, A. Reznik, K. W. Nugent, and S. Praver. The nature of damage in ion-implanted and annealed diamond. *Nuclear Instruments and Methods in Physics Research Section B: Beam Interactions with Materials and Atoms*, 148(1-4):626–633, 1999.

- [99] C. Uzan-Saguy, C. Cytermann, R. Brener, V. Richter, M. Shaanan, and R. Kalish. Damage threshold for ion-beam induced graphitization of diamond. *Applied Physics Letters*, 67(9):1194–1196, 1995.
- [100] W. Crookes. *Diamonds*. Harper & Brothers, London; New York, 1909.
- [101] S. C. Lind and D. C. Bardwell. The coloring and thermophosphorescence produced in transparent minerals and gems by radium radiation. *American Mineralogist*, 8:171–180, 1923.
- [102] D. S. Billington and J. H. Crawford. *Radiation Damage in Solids*. Princeton University Press, Princeton, New Jersey, 1961.
- [103] F.C. Champion. *Electronic properties of diamonds*. Butterworths, 1963.
- [104] R. H. Wentorf and K. A. Darrow. Semiconducting diamonds by ion bombardment. *Physical Review*, 137:A1614–A1616, Mar 1965.
- [105] V. S. Vavilov, M. I. Guseva, E. A. Konorova, V. V. Krasnopevtsev, V. F. Sergienko, and V. V. Tutov. Semiconducting diamonds produced by ion bombardment. *Soviet Physics—Solid State*, 8:1964, 1966. [Sov. Phys. Solid State 8, 1560 (1966)].
- [106] R. L. Hines. Radiation damage of diamond by 20-keV carbon ions. *Physical Review*, 138(6A):A1747–A1751, Jun 1965.
- [107] V. S. Vavilov, V. V. Krasnopevtsev, Y. V. Miljutin, A. E. Gorodetsky, and A. P. Zakharov. On structural transitions in ion-implanted diamond. *Radiation Effects and Defects in Solids*, 22(2):141–143, 1974.
- [108] J. J. Hauser and J. R. Patel. Hopping conductivity in C-implanted amorphous diamond, or how to ruin a perfectly good diamond. *Solid State Communications*, 18(7):789–790, 1976.
- [109] J. J. Hauser, J. R. Patel, and J. W. Rodgers. Hard conducting implanted diamond layers. *Applied Physics Letters*, 30(3):129–130, 1977.
- [110] R. Kalish, T. Bernsteins, B. Shapiro, and A. Talmi. A percolation theory approach to the implantation induced diamond to amorphous-carbon transition. *Radiation Effects and Defects in Solids*, 52(3):153–168, 1980.
- [111] J. F. Prins. Electrical resistance of diamond implanted at liquid nitrogen temperature with carbon ions. *Radiation Effects*, 76(3):79–82, 1983.
- [112] J. F. Prins. Onset of hopping conduction in carbon-ion-implanted diamond. *Physical Review B*, 31(4):2472–2478, Feb 1985.
- [113] J. F. Prins. Bipolar transistor action in ion implanted diamond. *Applied Physics Letters*, 41(10):950–952, 1982.

- [114] J. F. Prins. Activation of boron-dopant atoms in ion-implanted diamonds. *Physical Review B*, 38(8):5576–5584, 1988.
- [115] J. F. Prins. Annealing effects when activating dopant atoms in ion-implanted diamond layers. *Nuclear Instruments and Methods in Physics Research Section B: Beam Interactions with Materials and Atoms*, 59-60(Part 2):1387–1390, 1991.
- [116] J. F. Prins. Materials modification: doping of diamond by ion implantation. In A. A. Gippius, R. Helbig, and J. P. F. Sellschop, editors, *Proceedings of Symposium C on Properties and Applications of SiC, Natural and Synthetic Diamond and Related Materials of the 1990 E-MRS Fall Conference*, volume 11, pages 219–226. European Materials Research Society, North-Holland, 1992.
- [117] J. R. Zeidler, C. A. Hewett, R. Nguyen, C. R. Zeisse, and R. G. Wilson. A diamond driver-active load pair fabricated by ion implantation. *Diamond and Related Materials*, 2(10):1341–1343, 1993.
- [118] J. R. Zeidler, C. A. Hewett, and R. G. Wilson. Carrier activation and mobility of boron-dopant atoms in ion-implanted diamond as a function of implantation conditions. *Physical Review B*, 47(4):2065–2071, Jan 1993.
- [119] L. A. Davidson, S. Chou, J. F. Gibbons, and W. S. Johnson. Analysis of ion implanted diamond. *Radiation Effects and Defects in Solids*, 7(1):35–44, 1971.
- [120] T. E. Derry, R. W. Fearick, and J. P. F. Sellschop. A channeling investigation of light-ion damage in diamond. *Nuclear Instruments and Methods*, 170(1-3):407–412, 1980.
- [121] G. Braunstein, A. Talmi, R. Kalish, T. Bernstein, and R. Beserman. Radiation damage and annealing in Sb implanted diamond. *Radiation Effects and Defects in Solids*, 48(1):139–143, 1980.
- [122] A. Hoffman, S. Prawer, and M. Folman. Secondary electron emission spectroscopy: A sensitive and novel method for the characterization of the near-surface region of diamond and diamond films. *Applied Physics Letters*, 58(4):361–363, 1991.
- [123] R. A. Spits, J. F. Prins, and T. E. Derry. A determination of the critical damage density required for “amorphisation” of ion-implanted diamond. *Nuclear Instruments and Methods in Physics Research Section B: Beam Interactions with Materials and Atoms*, 85(1-4):347–351, 1994.
- [124] J. W. Vandersande. Low-temperature thermal conductivity of 0.75 MeV electron-irradiated type iia diamonds: evidence for interstitial migration below room temperature. In *Meeting on application of lattice defects in semiconductors, Freiburg, Germany, 1974*, volume 23 of *Institute of Physics Conference Series*, page 308, Bristol, England, 1975. Institute of Physics.

- [125] B. Massarani and J. C. Bourgoin. Defects at low temperature in electron-irradiated diamond. *Physical Review B*, 14(8):3682–3689, Oct 1976.
- [126] J. Bernholc, A. Antonelli, T. M. Del Sole, Y. Bar-Yam, and S. T. Pantelides. Mechanism of self-diffusion in diamond. *Physical Review Letters*, 61(23):2689–2692, 1988.
- [127] T. E. Derry, J. F. Prins, C. C. P. Madiba, J. Ennis, R. A. Spits, and J. P. F. Sellschop. Nuclear reaction profiling of implanted interstitial redistribution in diamond. *Nuclear Instruments and Methods in Physics Research Section B: Beam Interactions with Materials and Atoms*, 35(3-4):431–434, 1988.
- [128] R. A. Spits, T. E. Derry, J. F. Prins, and J. P. F. Sellschop. Depth profiling of implanted ^{13}C in diamond as a function of implantation temperature. *Nuclear Instruments and Methods in Physics Research Section B: Beam Interactions with Materials and Atoms*, 51(3):247–252, 1990.
- [129] J. F. Prins. Point-defect interactions when annealing diamonds implanted at low temperatures. *Physical Review B*, 44(6):2470–2479, Aug 1991.
- [130] J. Bernholc, S. A. Kajihara, C. Wang, and A. Antonelli. Theory of native defects, doping and diffusion in diamond and silicon carbide. In A. A. Gippius, R. Helbig, and J. P. F. Sellschop, editors, *Proceedings of Symposium C on Properties and Applications of SiC, Natural and Synthetic Diamond and Related Materials of the 1990 E-MRS Fall Conference*, pages 265–272. European Materials Research Society, North-Holland, 1992.
- [131] G. Davies, S. C. Lawson, A. T. Collins, A. Mainwood, and S. J. Sharp. Vacancy-related centers in diamond. *Physical Review B*, 46:13157–13170, Nov 1992.
- [132] L. Allers, A. T. Collins, and J. Hiscock. The annealing of interstitial-related optical centres in type II natural and CVD diamond. *Diamond and Related Materials*, 7(2-5):228–232, 1998.
- [133] R. Kalish, A. Reznik, S. Prawer, D. Saada, and J. Adler. Ion-implantation-induced defects in diamond and their annealing: Experiment and simulation. *physica status solidi (a)*, 174(1):83–99, 1999.
- [134] J. F. Prins and T. E. Derry. Radiation defects and their annealing behaviour in ion-implanted diamonds. *Nuclear Instruments and Methods in Physics Research Section B: Beam Interactions with Materials and Atoms*, 166:364–373, 2000.
- [135] J. F. Prins. Erratum: Point-defect interactions when annealing diamonds implanted at low temperatures [Phys. Rev. B 44, 2470 (1991)]. *Physical Review B*, 62(1):726, Jul 2000.
- [136] F. Bosia, N. Argiolas, M. Bazzan, P. Olivero, F. Piccolo, A. Sordini, M. Vanoni, and E. Vittone. Modification of the structure of diamond with MeV ion implantation. *Diamond and Related Materials*, 20(5-6):774–778, 2011.

- [137] A. A. Gippius, R. A. Khmel'nitskiy, V. A. Dravin, and A. V. Khomich. Diamond-graphite transformation induced by light ions implantation. *Diamond and Related Materials*, 12(3-7):538–541, 2003.
- [138] M. Nesládek, K. Haenen, J. D'Haen, S. Koizumi, and H. Kanda. N-type P-doped polycrystalline diamond. *physica status solidi (a)*, 199(1):77–81, 2003.
- [139] M. S. Dresselhaus and R. Kalish. *Ion Implantation in Diamond, Graphite, and Related Materials*. Springer-Verlag, Berlin, 1992.
- [140] R. Kalish. Ion beam modification of diamond. *Diamond and Related Materials*, 2(5-7):621–633, 1993.
- [141] R. Kalish. *Ion implantation and diffusion in diamond*, chapter 6, pages 189–219. Number 9 in EMIS datareviews series. INSPEC, London, U.K., 1994.
- [142] S. Prawer and R. Kalish. Ion-beam-induced transformation of diamond. *Physical Review B*, 51(22):15711, 1995.
- [143] R. Kalish and S. Prawer. *Ion implantation of diamond and diamond films*, chapter 26, pages 945–982. CRC Press, 1998.
- [144] C. H. Bennett and P. W. Shor. Quantum information theory. *IEEE Transactions on Information Theory*, 44(6):2724–2742, Oct 1998.
- [145] K. L. Bhatia, S. Fabian, S. Kalbitzer, Ch. Klatt, W. Krätschmer, R. Stoll, and J. F. P. Sellschop. Optical effects in carbon-ion irradiated diamond. *Thin Solid Films*, 324(1-2):11–18, 1998.
- [146] A. V. Khomich, V. I. Kovalev, E. V. Zavedeev, R. A. Khmel'nitskiy, and A. A. Gippius. Spectroscopic ellipsometry study of buried graphitized layers in the ion-implanted diamond. *Vacuum*, 78(2-4):583–587, 2005.
- [147] A. A. Bettiol, S. Venugopal Rao, E. J. Teo, J. A. van Kan, and F. Watt. Fabrication of buried channel waveguides in photosensitive glass using proton beam writing. *Applied Physics Letters*, 88(17):171106, 2006.
- [148] P. Olivero, S. Calusi, L. Giuntini, S. Lagomarsino, A. Lo Giudice, M. Massi, S. Sciortino, M. Vannoni, and E. Vittone. Controlled variation of the refractive index in ion-damaged diamond. *Diamond and Related Materials*, 19(5-6):428–431, 2010.
- [149] A. Sytchkova, S. Lagomarsino, M. Vannoni, S. Calusi, and P. Olivero. Optical characterization of proton irradiated diamond. In L. Mazuray, R. Wartmann, A. Wood, J.-L. M. Tissot, and J. M. Raynor, editors, *Proc. SPIE 8167, Optical Design and Engineering IV*, volume 8167, page 81671O. SPIE, 2011.

- [150] B. R. Patton, P. R. Dolan, F. Grazioso, M. B. Wincott, J. M. Smith, M. L. Markham, D. J. Twitchen, Y. Zhang, E. Gu, M. D. Dawson, B. A. Fairchild, A. D. Greentree, and S. Prawer. Optical properties of single crystal diamond microfilms fabricated by ion implantation and lift-off processing. *Diamond and Related Materials*, 21(0):16–23, 2012.
- [151] A. Battiato, F. Bosia, S. Ferrari, P. Olivero, A. Sytchkova, and E. Vittone. Spectroscopic measurement of the refractive index of ion-implanted diamond. *Optics Letters*, 37(4):671–673, Feb 2012.
- [152] M. A. Draganski, E. Finkman, B. C. Gibson, B. A. Fairchild, K. Ganesan, N. Nabatova-Gabain, S. Tomljenovic-Hanic, A. D. Greentree, and S. Prawer. Tailoring the optical constants of diamond by ion implantation. *Optical Materials Express*, 2(5):644–649, May 2012.
- [153] S. Lagomarsino, P. Olivero, S. Calusi, D. Gatto Monticone, L. Giuntini, M. Massi, S. Sciortino, A. Sytchkova, A. Sordini, and M. Vannoni. Complex refractive index variation in proton-damaged diamond. *Optics Express*, 20(17):19382–19394, Aug 2012.
- [154] M. A. Draganski, B. A. Fairchild, A. Alves, E. Finkman, J. Orwa, S. Rubanov, B. Gibson, K. Ganesan, P. Spizziri, A. D. Greentree, P. N. Johnston, D. N. Jamieson, and S. Prawer. The refractive index of ion implanted diamond. In *Australian Institute of Physics (AIP) 18th National Congress*, pages 175–178, Adelaide, S. Aust., 2008. Australian Institute of Physics, Causal Productions.
- [155] C. Thomsen, J. Strait, Z. Vardeny, H. J. Maris, J. Tauc, and J. J. Hauser. Coherent phonon generation and detection by picosecond light pulses. *Physical Review Letters*, 53:989–992, Sep 1984.
- [156] C. Thomsen, H. T. Grahn, H. J. Maris, and J. Tauc. Surface generation and detection of phonons by picosecond light pulses. *Physical Review B*, 34:4129–4138, Sep 1986.
- [157] B. C. Daly, T. B. Norris, J. Chen, and J. B. Khurgin. Picosecond acoustic phonon pulse propagation in silicon. *Physical Review B*, 70:214307, Dec 2004.
- [158] J. K. Miller, J. Qi, Y. Xu, Y.-J. Cho, X. Liu, J. K. Furdyna, I. Perakis, T. V. Shahbazyan, and N. Tolk. Near-bandgap wavelength dependence of long-lived traveling coherent longitudinal acoustic phonons in gasb-gaas heterostructures. *Physical Review B*, 74:113313, Sep 2006.
- [159] J. Qi, J. A. Yan, H. Park, A. Steigerwald, Y. Xu, S. N. Gilbert, X. Liu, J. K. Furdyna, S. T. Pantelides, and N. Tolk. Mechanical and electronic properties of ferromagnetic $\text{Ga}_{1-x}\text{Mn}_x\text{As}$ using ultrafast coherent acoustic phonons. *Physical Review B*, 81:115208, Mar 2010.

- [160] O. Matsuda and O. B. Wright. Reflection and transmission of light in multilayers perturbed by picosecond strain pulse propagation. *Journal of the Optical Society of America B*, 19(12):3028–3041, Dec 2002.
- [161] A. Steigerwald, Y. Xu, J. Qi, J. Gregory, X. Liu, J. K. Furdyna, K. Varga, A. B. Hmelo, G. Lupke, L. C. Feldman, and N. Tolk. Semiconductor point defect concentration profiles measured using coherent acoustic phonon waves. *Applied Physics Letters*, 94(11):111910, 2009.
- [162] J. F. Ziegler, M. D. Ziegler, and J. P. Biersack. SRIM—The stopping and range of ions in matter (2010). *Nuclear Instruments and Methods in Physics Research Section B: Beam Interactions with Materials and Atoms*, 268(11-12):1818–1823, 2010.
- [163] A. Steigerwald, A. B. Hmelo, K. Varga, L. C. Feldman, and N. Tolk. Determination of optical damage cross-sections and volumes surrounding ion bombardment tracks in GaAs using coherent acoustic phonon spectroscopy. *Journal of Applied Physics*, 112(1):013514, 2012.
- [164] D. Yarotski, E. Fu, L. Yan, Q. Jia, Y. Wang, A. J. Taylor, and B. P. Uberuaga. Characterization of irradiation damage distribution near $\text{TiO}_2/\text{SrTiO}_3$ interfaces using coherent acoustic phonon interferometry. *Applied Physics Letters*, 100(25):251603, 2012.
- [165] C. Rossignol, B. Perrin, S. Laborde, L. Vandenbulcke, M. I. De Barros, and P. Djemia. Nondestructive evaluation of micrometric diamond films with an interferometric picosecond ultrasonics technique. *Journal of Applied Physics*, 95(8):4157–4162, 2004.
- [166] A. Klokov, M. Kochiev, A. Sharkov, V. Tsvetkov, and R. Khmelnskiy. Graphitized layer buried in a diamond: photothermal properties and hypersound generation under picosecond optical excitation. *Journal of Physics: Conference Series*, 278(1):012019, 2011.
- [167] D. Saada, J. Adler, and R. Kalish. Transformation of diamond (sp^3) to graphite (sp^2) bonds by ion-impact. *International Journal of Modern Physics C-Physics and Computer*, 9(1):61–70, 1998.
- [168] A. Khomich, R. Khmelnskiy, V. Dravin, A. Gippius, E. Zavedeev, and I. Vlasov. Radiation damage in diamonds subjected to helium implantation. *Physics of the Solid State*, 49:1661–1665, 2007.
- [169] J. F. Prins, T. E. Derry, and J. P. F. Sellschop. Volume expansion of diamond during ion implantation. *Physical Review B*, 34(12):8870, 1986.
- [170] M. Wakaki. *Physical Properties and Data of Optical Materials*, chapter 4, pages 135–138. CRC Press, 2007.

- [171] K. Wenzlik, J. Heibei, and E. Voges. Refractive index profiles of helium implanted LiNbO_3 and LiTaO_3 . *physica status solidi (a)*, 61(2):K207–K211, 1980.
- [172] D. T. Y. Wei, W. W. Lee, and L. R. Bloom. Large refractive index change induced by ion implantation in lithium niobate. *Applied Physics Letters*, 25(6):329–331, 1974.
- [173] J.O. Orwa, D.N. Jamieson, K.W. Nugent, S. Praver, and R. Kalish. Effects of damage on diffusion of implanted helium in diamond measured by nuclear elastic scattering. *Nuclear Instruments and Methods in Physics Research Section B: Beam Interactions with Materials and Atoms*, 124(4):515–518, 1997.
- [174] J. P. Goss, R. J. Eyre, P. R. Briddon, and A. Mainwood. Density functional simulations of noble-gas impurities in diamond. *Physical Review B*, 80:085204, Aug 2009.
- [175] H. Lawler, A. Steigerwald, J. Gregory, H. Krzyzanowska, and N. H. Tolk. Experimental and theoretical determination of the opto-acoustic spectra of Si(100). In preparation, 2013.
- [176] M. Born, E. Wolf, and A. B. Bhatia. *Principles of Optics: Electromagnetic Theory of Propagation, Interference and Diffraction of Light*. Cambridge University Press, 1999.
- [177] J. A. Nelder and R. Mead. A simplex method for function minimization. *The Computer Journal*, 7(4):308–313, 1965.
- [178] B. Gough. *GNU Scientific Library: Reference Manual*. A GNU manual. Network Theory, 2009.
- [179] L. S. Hounscome, R. Jones, M. J. Shaw, and P. R. Briddon. Photoelastic constants in diamond and silicon. *physica status solidi (a)*, 203(12):3088–3093, 2006.